

Soft matter probed by nonlinear scattering: self-assembly, interfaces, hydration, and long-range order

Présentée le 27 janvier 2020

à la Faculté des sciences et techniques de l'ingénieur
Chaire Julia Jacobi de photomédecine - Laboratoire de biophotonique fondamentale
Programme doctoral en photonique

pour l'obtention du grade de Docteur ès Sciences

par

Jan DEDIC

Acceptée sur proposition du jury

Prof. C. Moser, président du jury
Prof. S. Roke, directrice de thèse
Prof. P. Hamm, rapporteur
Dr H. B. de Aguiar, rapporteur
Prof. M. M. C. Bastings, rapporteuse

To my family

Acknowledgments

First and foremost, I want to thank my supervisor, Prof. Sylvie Roke for putting her trust in me, for giving me the opportunity to work on cutting-edge research in her group, and for her advice on how to write and think like a scientist.

I would also like to thank the rest of my jury: Prof. Peter Hamm, Dr. Hilton Barbosa de Aguiar, Prof. Maartje Bastings, and Prof. Christophe Moser for reading my thesis and helping me to improve it.

These past 4.5 years would not have been as fun and enriching without my great colleagues at the Laboratory for Fundamental Biophotonics. Namely: Dr. Carlos Macias-Romero, Dr. Cornelis Lütgebaucks, Dr. Yixing Chen, Dr. Nikolay Smolentsev, Dr. Marie Didier, Dr. Orly Tarun, Dr. Evangelia Zdrali, Filip Kovacik, Siyuan Wang, Prof. Halil Okur, Igor Nahálka, Dr. Claire Teulon, Dr. Arianna Marchioro, Nathan Dupertuis, Sergiy Kulik, Maksim Eremchev, Tereza Schönfeldová, David Roesel, and Seonwoo Lee. I would also like to thank our administrative assistant Rebecca Veselinov. It has been a pleasure to work with all of you.

My gratitude goes to Prof. Hatice Altug for her moral support. To Prof. Aleksandra Radenovic, Prof. Dominique Pioletti and Dr. Jens Antons for providing me samples. To Prof. Andrea Ablasser, the members of LAPD, LO, BIOS labs and the Moser group for lending me equipment or allowing me to use their labs. To Prof. Georg Pabst and Dr. Barbara Eicher for kindly hosting me in their group, sharing their know-how, giving me feedback and ideas. To Prof. Eric Tyrode for his moral and technical support. To Prof. Pernilla Wittung-Stafshede and Dr. Sandra Rocha for our fruitful collaboration.

I also thank my former professors and supervisors, especially: Dr. Filip Novotný, Prof. Antonín Fejfar, Prof. Alexander Kromka and Doc. Ivan Richter, who gave me the first taste of scientific research and who supported me in continuing my studies abroad.

I am very grateful to all of my old friends back in the Czech Republic and to the new ones I've made here. I would especially like to thank Jenda, Hanička & Eduard for being there and being awesome. A special mention also goes to all of my climbing and skiing buddies who are too numerous to be listed here.

Lastly, I would like to thank Jess and my family for making my life brigher, and for helping me get to where I am today.

Lausanne, 14 October, 2019

Jan Dedic

Abstract

All organisms are made to a large extent of soft matter - macromolecules such as proteins and polysaccharides, or assemblies of small molecules such as lipids embedded in an aqueous environment. Understanding the role of order in soft matter presents a challenge for experimentalists because such systems are neither completely disordered nor perfectly crystalline. This is especially the case for the aqueous environment itself whose order fluctuates on femto- and pico-second time scales. In this thesis, we attempt to elucidate the presence, extent, changes, and implications of orientational order in several soft matter systems: from polyelectrolyte solutions to lipid membrane interfaces and supramolecular structures. To perform this task, we employ nonlinear optical techniques: second-harmonic and sum-frequency scattering.

In the first two chapters, we explore the structure of water in aqueous polyelectrolyte solutions. Polyelectrolytes of high molecular mass are shown to induce orientational order in water that spans hundreds of nanometers. Using an adapted model of second-harmonic scattering from charged particles, we can explain the observed ordering in terms of weakly screened long-range electrostatic interactions that perturb the structure of water via charge-dipole interactions. Upon exchanging ordinary (light) water for heavy water, we observe a significant nuclear quantum effect in the induced order, indicating that bulk water-water correlations are enhanced as well by polyelectrolytes.

In the following chapter, we exploit the same nuclear quantum effect in polyelectrolyte solutions to show that the polyelectrolyte-induced orientational order correlates with an anomalous increase in the reduced viscosity. We propose that the viscosity anomaly arises from enhanced order in a solvent which hinders the viscous flow. This observation represents a rare direct link between a microscopic property and a macroscopic observable.

In the last two chapters, we change focus from homogeneous solutions to dispersions of liposomes which serve as models of biological membranes. In Chapter 5 we explore the binding of the protein alpha-synuclein to anionic vesicles from the perspective of interfacial water. We show that the adsorption of the protein to a vesicle decreases the order in the interfacial water by 30% but does not affect the surface nor the zeta potential. We propose that the changes in the structure of interfacial water can serve as a label-free probe of protein binding.

In the last chapter, we investigate the supramolecular chemistry of inclusion complexes of methyl- β -cyclodextrin with various lipids. By combining multiple nonlinear scattering techniques, we show that the complexes self-assemble into micrometer-long directed fibers. Based on measurements of different lipids, we propose that the self-assembly process is

driven by hydrogen bonding between the lipid headgroup and cyclodextrin. Lastly, we show that the long-range order of the self-assembled structure is transmitted into the structure of the hydrating water.

Keywords: water, polyelectrolytes, hydration, long-range order, lipid membranes, aqueous interfaces, protein adsorption, self-assembly, host-guest complexes, soft matter, nonlinear optics, light scattering.

Résumé

Tous les organismes sont constitués dans une large mesure de matière molle - de macromolécules telles que des protéines et des polysaccharides, ou d'assemblages de petites molécules telles que des lipides intégrés dans un environnement aqueux. Comprendre le rôle de l'ordre dans la matière molle constitue un défi pour les chercheurs, car de tels systèmes ne sont ni complètement désordonnés, ni parfaitement cristallins. C'est particulièrement le cas pour l'environnement aqueux lui-même dont l'agencement moléculaire fluctue sur les échelles de temps de l'ordre de la femto et de la picoseconde. Dans cette thèse, nous tentons d'élucider la présence, l'étendue, les changements et les implications des diverses orientations moléculaires dans différents systèmes de matière molle : depuis les solutions de polyélectrolytes aux interfaces de membrane lipidique, en passant par les structures supramoléculaires. Pour réaliser cette tâche, nous utilisons des techniques d'optique non linéaire : la diffusion de seconde harmonique et de sommation de fréquence.

Dans les deux premiers chapitres, nous explorons la structure de l'eau dans des solutions aqueuses de polyélectrolytes. Il a été démontré que les polyélectrolytes de masse moléculaire élevée ordonnent l'orientation des molécules dans l'eau sur une centaine de nanomètres. À l'aide d'un modèle adapté de diffusion de la deuxième harmonique à partir de particules chargées, nous pouvons expliquer la structuration observée en termes d'interactions électrostatiques à longue portée faiblement écrantées qui perturbent la structure de l'eau via des interactions charge-dipôle. Lors de l'échange d'eau ordinaire (légère) avec l'eau lourde, nous observons un effet quantique nucléaire important sur l'ordonnement induit, indiquant que les corrélations entre molécules d'eau sont également accrues par la présence des polyélectrolytes.

Dans le chapitre suivant, nous exploitons le même effet nucléaire quantique dans des solutions de polyélectrolytes pour montrer que l'agencement moléculaire induit par un polyélectrolyte est corrélé à une augmentation anormale de la viscosité réduite. Nous postulons que l'anomalie de viscosité découle d'un ordonnancement amélioré dans le solvant, qui entrave le flux visqueux. Cette observation représente un lien direct rare entre une propriété microscopique et une quantité observable macroscopique.

Dans les deux derniers chapitres, nous passons des solutions homogènes aux dispersions de liposomes qui servent de modèles aux membranes biologiques. Au chapitre 5, nous explorons la liaison de la protéine alpha-synucléine aux vésicules anioniques du point de vue de l'eau interfaciale. Nous montrons que l'adsorption de la protéine dans une vésicule diminue l'ordre de 30% dans l'eau interfaciale mais n'affecte pas la surface ni le potentiel zêta. Nous

proposons que les changements dans la structure de l'eau interfaciale puissent servir de senseur sans marqueur pour les processus de liaison protéiques.

Dans le dernier chapitre, nous étudions la chimie supramoléculaire des complexes d'inclusion de méthyl- β -cyclodextrine avec divers lipides. En combinant plusieurs techniques de diffusion non linéaire, nous montrons que les complexes s'auto-assemblent en fibres directionnelles de plusieurs micromètres de long. En nous fondant sur la réponse de différents lipides, nous proposons que le processus d'auto-assemblage soit activé par liaison hydrogène entre le groupe de tête du lipide et la molécule de cyclodextrine. Enfin, nous montrons que l'ordonnement à longue distance de la structure auto-assemblée est transmis à la structure de l'eau qui l'hydrate.

Mots-clés: eau, polyélectrolytes, hydratation, ordonnancement à longue distance, membranes lipidiques, interfaces aqueuses, adsorption de protéines, auto-assemblage, complexes hôte-invité, matière molle, optique non linéaire, diffusion de la lumière.

Contents

Acknowledgments	i
Abstract	iii
Résumé	v
List of figures	xi
List of tables	xiii
Chapter 1: Introduction	1
1.1. Water	1
1.2. Water isotopes and nuclear quantum effects in water	2
1.3. Aqueous electrolyte and polyelectrolyte solutions	3
1.4. Lipid membranes, proteins, and hydration	4
1.4.1. Model lipid membranes and lipid chemistry	6
1.5. Nonlinear spectroscopy	8
1.5.1. Second-order optical nonlinearities	8
1.5.2. Reflection from planar interfaces	10
1.5.3. Scattering from colloidal dispersions	11
1.5.4. Hyper-Rayleigh scattering and coherent SHS from bulk liquids	11
1.6. The structure of this thesis	12
Chapter 2: Experimental details and methodology	15
2.1. Theory of nonlinear scattering	16
2.1.1. Assumptions	16
2.1.2. Symmetries	17
2.1.3. Vibrational sum-frequency scattering	19
2.1.4. Elastic second-harmonic scattering from bulk liquids	24
2.1.5. Elastic second-harmonic scattering from charged particles	26
2.1.6. SH scattering from cylindrical particles	28
2.1.7. SHS from randomly oriented particles	31
2.2. Experimental apparatus for sum-frequency scattering	32
2.3. Experimental apparatus for second-harmonic scattering	35

2.4. Dynamic light scattering	37
2.5. Electrophoretic mobility measurements.....	38
Chapter 3: Hyaluronan orders water up to hundreds of nanometers and induces significant nuclear quantum effects	40
3.1. Introduction	41
3.2. Experimental section.....	42
3.2.1. Materials.....	42
3.2.2. Angle-resolved second harmonic scattering	42
3.2.3. fs-ESHS from HA compared to simple electrolytes	43
3.2.4. Angle-resolved second-harmonic scattering	45
3.2.1. Modeling of the fs-ESHS results	46
3.2.2. Modelling the SHS response	47
3.2.3. Concentration dependence and polyelectrolyte size	50
3.2.4. Extended hydration shell	52
3.3. Conclusions	53
3.4. Appendix.....	54
3.4.1. Full fs-ESHS patterns of HA in H ₂ O	54
3.4.2. fs-ESHS in sss polarization direction	54
3.4.3. Dependence of fs-ESHS of HA on ionic strength.....	55
3.4.4. Power dependence and elasticity of the fs-ESHS process.....	56
Chapter 4: Polyelectrolytes induce water-water correlations that result in dramatic viscosity changes and nuclear quantum effects	60
4.1. Introduction	61
4.2. Experimental section.....	63
4.2.1. Chemicals and sample preparation.....	63
4.2.2. fs-ESHS measurements	64
4.2.3. Dynamic viscosity measurements.....	64
4.2.4. Femtosecond snapshots of long-range order.....	65
4.2.5. Viscosity	68
4.3. Summary and Conclusions	72

4.4. Appendix.....	72
4.4.1. fs-ESHS and reduced viscosity of poly(styrene sulfonate)	72
4.4.2. Calculation of the reduced specific viscosity of PEG.....	73
4.4.3. Modeling the reduced specific viscosity of PAA	73
Chapter 5: Membrane–Protein–Hydration Interaction of α -Synuclein with Anionic Vesicles Probed via Angle-Resolved Second-Harmonic Scattering	76
5.1. Introduction	77
5.2. Experimental section.....	79
5.2.1. Chemicals.....	79
5.2.2. Protein expression and purification	79
5.2.3. Sample preparation	79
5.2.4. AR-SHS measurements	81
5.2.5. Fitting the AR-SHS patterns	82
5.3. Results and Discussion.....	83
5.4. Conclusions	87
Chapter 6: Self-assembly of cyclodextrin-lipid complexes probed by nonlinear scattering	89
6.1. Introduction	90
6.2. Experimental section.....	91
6.2.1. Chemicals.....	91
6.2.2. Sample preparation and measurements	92
6.2.3. The m β CD-liposome interaction is lipid-specific.....	93
6.2.4. Time and concentration dependence of the SFS response.....	96
6.2.5. Structure of the m β CD-liposome complex	98
6.2.6. Hydration.....	101
6.2.7. The self-assembly mechanism	101
6.3. Discussion	103
6.4. Conclusion	103
6.5. Appendix.....	104
6.5.1. SFS spectra of POPS+m β CD in all polarization combinations.....	104

6.5.2. Fitting of the SFS spectra	105
6.5.3. SH scattering from a randomly oriented cylinder.....	105
6.5.4. Dependence of SHS on the dimensions of the cylinder	106
6.5.5. The choice of the χ^2 element.....	107
Chapter 7: Conclusion and outlook.....	108
7.1. Summary	108
7.2. Outlook	109
List of publications.....	112
References.....	113
Curriculum vitae	131

List of figures

Figure 1.1: Water and hydrogen bonding.....	1
Figure 1.2: Illustration of a cell (plasma) membrane.	5
Figure 1.3: Examples of systems that are studied using nonlinear spectroscopic techniques.....	7
Figure 1.4: Energy diagrams and geometries of second-order spectroscopic techniques.....	9
Figure 2.1: Symmetries of a spherical particle.	18
Figure 2.2: Geometry of the sum-frequency scattering process.....	20
Figure 2.3: Theoretically calculated SF scattering patterns.....	23
Figure 2.4: A chart showing the contributions of the surface susceptibility elements	24
Figure 2.5: H ₂ O molecule shown in a Cartesian coordinate system.....	25
Figure 2.6: The sources of SH scattering from charged particles in water..	27
Figure 2.7: Geometry of SHS from a cylindrical particle.....	29
Figure 2.8: Rotation via the proper Euler angles (z-x-z convention).....	31
Figure 2.9: Schema of the optical apparatus for vibrational sum-frequency scattering.....	32
Figure 2.10: The characteristics of the SpitFire Pro laser output.....	33
Figure 2.11: Spectra of the pulses used for SFS.	34
Figure 2.12: The experimental setup for second-harmonic scattering.....	36
Figure 2.13: Characteristics of the laser used for SHS/fs-ESHS experiments.....	36
Figure 2.14: Schema of a DLS system.	37
Figure 2.15: The distribution of ions around a negatively charged particle in an electrolyte solution.....	39
Figure 3.1: Hyaluronan enhances orientational correlations between water molecules.....	45
Figure 3.2: Scattering patterns of HA solutions are concentration-dependent.....	46
Figure 3.3: Illustration of the model.....	48
Figure 3.4: Relevant length scales as a function of HA concentration and the temperature dependence of the fs-ESHS response of HA in H ₂ O.....	51
Figure 3.5: fs-ESHS patterns of HA solutions in H ₂ O at various HA concentrations.....	54
Figure 3.6: Absence of fs-ESHS response in sss polarization combination.	55
Figure 3.7: Dependence of fs-ESHS response of HA and of the Debye length on excess ionic strength..	56
Figure 3.8: Verification of the power dependence of the fs-ESHS intensity.....	57
Figure 3.9: Verification of the elasticity of fs-ESHS from HA in H ₂ O.....	58
Figure 4.1: Long-range distortion of the orientational order of water..	63
Figure 4.2: Negligible contribution of polyelectrolytes to second-harmonic scattering. incoherent scattering.	66
Figure 4.3: fs-ESHS response of PAA disappears with the addition of salt.	67

Figure 4.4: Polyelectrolytes induce strong orientational correlations leading to viscosity changes.....	68
Figure 4.5: Comparison of the measured reduced viscosity of PAA with a theoretical model.	71
Figure 4.6: Polyelectrolytes induce strong orientational correlations leading to viscosity changes.....	73
Figure 5.1: The lipids and liposomes used in this study	80
Figure 5.2: Reproducibility of the SHS measurements.....	81
Figure 5.3: SHS and electrophoretic mobility measurements of DOPG and α S-DOPG.	84
Figure 5.4: Chiral measurements and proposed structure of the α S-DOPG-water interface.	87
Figure 6.1: Molecular structures of m β CD and the lipids used in this work.	91
Figure 6.2: m β CD-liposome interaction is highly specific to the lipid head group	93
Figure 6.3: Control sum-frequency measurements of separate m β CD and POPS.....	96
Figure 6.4: Concentration and time dependence of the SFS response from POPS and POPC liposomes incubated with m β CD	97
Figure 6.5: Second-harmonic scattering from POPS+m β CD..	100
Figure 6.6: Suggested binding model of m β CD to lipid head groups.	102
Figure 6.7: SFS spectra of POPS+m β CD in all 8 polarization combinations.....	104
Figure 6.8: Calculated SHS patterns of randomly oriented cylinders.	106
Figure 6.9: Calculated SHS patterns of a randomly oriented cylinder.	107

List of tables

Table 1.1: Comparison of several properties of light and heavy water	2
Table 5.1: List of constants used in the fitting procedure of AR-SHS patterns.	83
Table 6.1 : Assignment of the peaks in the SFS spectra of the POPS+m β CD and DMPG+m β CD samples to vibrational modes.....	95
Table 6.2: Fitted amplitude, frequency and linewidth of the POPS and DMPG samples. ...	105

Chapter 1: Introduction

Water is the common thread running throughout this thesis. Its importance to the survival of all known life forms is known to everyone. What is less obvious is how and why this is so. The seemingly simple structure of the water molecule, two hydrogen atoms each covalently bound to a central oxygen atom, results in a liquid with surprisingly complex behavior. In this thesis, we attempt to provide new insights into the complex behavior of aqueous systems, such as how far can correlations between water molecules reach, what is the structure of water at biological interfaces, and how molecules in water self-assemble.

1.1. Water

Water is an exceptionally good solvent for polar and ionic compounds. Despite its small size, it has a high viscosity, surface tension, melting and boiling points. The density of water reaches a maximum at 4 °C making ice float. These and many other unusual properties of water stem from the ability of H₂O molecules to form an ordered three-dimensional network via hydrogen bonds (H-bonds) [1, 2] (Figure 1.1). Each H₂O molecule can form up to 4 H-bonds with the surrounding water, 2 bonds via the two lone electron pairs on the oxygen atom and 1 bond for each hydrogen atom. Because these bonds are directional, H-bonded water is tetrahedrally coordinated [3]. On average, an H₂O molecule at standard conditions has ~3.6 H-bonds [4]. The H-bond network is labile, with an estimated H-bond enthalpy of only 6.3 kJ/mol [5] compared to the enthalpy of the O-H covalent bond of ~500 kJ/mol [6]. The H-bond network is also highly dynamic: fluctuations (librations) of the H-bonds occur on a sub-picosecond time scale and water reorientation occurs within 2-3 picoseconds [7-10].

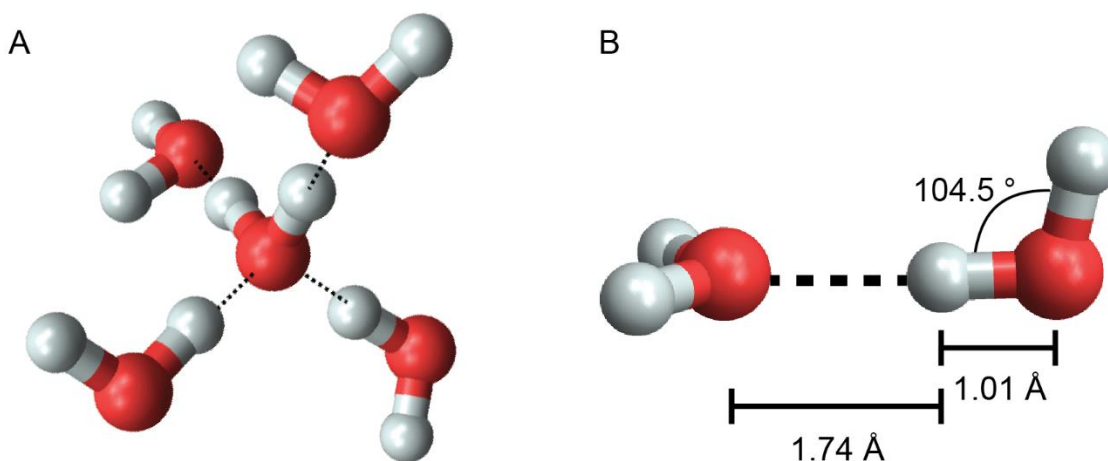


Figure 1.1: Water and hydrogen bonding. (A) An H₂O molecule tetrahedrally coordinated with 4 surrounding water molecules via directional hydrogen bonds (dashed lines). (B) Schema of two hydrogen-bonded H₂O molecules. The dimensions are taken from Ref. [11].

In aqueous solutions, the H-bond network rearranges to accommodate the dissolved species. Depending on the chemical nature, shape, size and electrical charge of the solute, the rearrangement of the H-bond network may be favorable or unfavorable which impacts the solubility [12]. The structure of the H-bond network of water plays a role in many fundamental biological processes, such as membrane formation, protein folding, molecular recognition, adsorption and lubrication [13-16].

1.2. Water isotopes and nuclear quantum effects in water

The oxygen atom and the two hydrogen atoms that constitute the water molecule can exist in more than one stable isotope, the most common being ^{16}O and ^1H . The other stable isotopes are ^{18}O and ^2H (Deuterium, D) [17]. In this thesis, we use $^1\text{H}_2^{16}\text{O}$ (H_2O , light water) and $^2\text{H}_2^{16}\text{O}$ (D_2O , heavy water). The seemingly simple isotope exchange of hydrogen to deuterium leads to considerable changes in certain physicochemical properties. Table 1.1 shows a comparison of several properties of H_2O and D_2O . These differences are due to small changes in the nature of the hydrogen bond whose origins lie in the quantum mechanical behavior of protons. As such, those isotope effects of water that cannot be accounted for by a classical theory are referred to as nuclear quantum effects [2, 18, 19]. The nuclear quantum effects are more pronounced in H_2O than in D_2O due to the nucleus of ^1H being ~50% lighter than ^2H . From Table 1.1 we can see that properties such as the refractive index, the dielectric constant and the dipole moment are almost identical (<1 % difference), while the dielectric relaxation time, vibrational energies, and dynamic viscosity differ by >20 %. More fundamentally, the O-H covalent bond is ~3% shorter in than the O-D bond, whereas the O-H...O hydrogen bond is ~4% longer than the O-D...O bond [11]. The net result of the nuclear quantum effects is that the H-bonds are stronger, the H-bond network is more tetrahedral and more coordinated in D_2O than in H_2O [11, 18].

Table 1.1: Comparison of several properties of light and heavy water. Values are given at standard conditions unless stated otherwise. Partially adapted from Ref. [18].

Property	H_2O	D_2O	Δ (%)
Mass (amu)	18.0153	20.0276	+11.2
Density (g/cm^3) [20]	0.9970474	1.104362	+10.8
Temperature of the triple point (K) [21]	373.15	376.97	+1.0
Temperature of max. density (K) [22]	277.13	284.34	+2.6
Dynamic viscosity (cP) [20, 23]	0.8903	1.0963	+23.1
Dipole moment (D) [24]	1.8546	1.8558	+0.1

Refractive index (550 nm) [25, 26]	1.333977	1.329242	-0.4
Dielectric constant [27]	78.7854	78.2618	-0.7
Autoionization constant [28]	13.993	14.957	+6.9
Dielectric relaxation time (ps, 293.15 K) [29]	9.55	12.3	+28.8
Vibrational frequencies (gas phase) (cm^{-1}) [30, 31]	3657.1	2671.6	-26.9
	1594.7	1178.4	-26.1
	3755.9	2787.7	-25.8
Gas phase dimer dissociation energy (kJ/mol, 10 K) [32, 33]	13.22	14.88	+12.6
O-H bond length (\AA) [11]	1.01	0.98	-3.0
H-bond length (\AA) [11]	1.74	1.81	+4.0
Avg. number of H-bonds [11]	3.62	3.76	+3.9

1.3. Aqueous electrolyte and polyelectrolyte solutions

When we refer to water in our everyday lives, we most often implicitly mean an aqueous electrolyte solution. The role of ions in water has been studied for more than a century. The fact that the interaction of ions with water is not trivial was demonstrated by the famous work of Franz Hofmeister who showed that various ions differ in their ability to solubilize or precipitate proteins [34-36]. This is due to differences in the way ions disturb the structure of water. As for all solutes, the H-bond network of water has to accommodate the space occupied by the dissolved ions. In addition, the electrostatic field emitted by ions interacts with the water dipole, forcing it to align with the electric field [37]. The region around the ion where the structure of water is disturbed is referred to as the hydration shell. Understanding the nature of the water in the hydration shell and the shell's size is key for elucidating the role of ions in phenomena such as protein folding, self-assembly, adsorption, lubrication, and viscous flow. However, advancement in this field has been hampered by a lack of experimental techniques capable of accessing this information. For example, the spatial extent of an ion's influence on the structure of water remains a controversial topic as it depends on the technique used to measure it [38]. The most pronounced changes in water structure are observed in the first, second or third hydration shell (up to 1 nm) [12, 39]. However, recent studies have indicated that the orientational order of water may be disturbed up to 20 nm away from the ion [40, 41]. Unlike the Hofmeister effect, the recently observed extended hydration is not ion-specific but shows a strong isotope effect upon $\text{H}_2\text{O} \rightarrow \text{D}_2\text{O}$ exchange. This indicates that water-water interactions are also important along with charge-water interaction.

In biological and other aqueous systems, the electrical charge is not only found on simple ions but also on large macromolecules (polyelectrolytes). Polyelectrolytes are

macromolecules containing species that ionize in a polar solvent (water). This includes proteins, polysaccharides, DNA, RNA, and various synthetic polymers, such as poly(styrene sulfonate) and poly(acrylic acid). Polyelectrolytes are used in foods and cosmetics (thickeners, emulsifiers) [42], water treatment [43, 44], medical implants [45], and building materials (superplasticizers) [46]. Proteins and charged polysaccharides constitute a significant part of the mucus, the synovial fluid, epithelium, muscle and connective tissues [47, 48]. The swelling behavior of polyelectrolytes and their ability to bind large amounts of water are key to maintaining various biological functions [49]. The behavior of polyelectrolytes is different from and considerably more complex than that of neutral polymers. The properties of polyelectrolytes are influenced by additional electrostatic interactions between the ionized species on the polyelectrolyte chain [50-52]. These interactions are, in turn, modulated by mobile ions dissolved in the solution that screen electrostatic fields. Due to these electrostatic interactions, polyelectrolyte solutions display some unusual properties, such as anomalous viscosity, that cannot be explained by models that work for neutral polymers [52-54]. The existing models of polyelectrolyte behavior are often based on a mean-field approximation of water which is known to be inaccurate for electrolyte solutions [12, 34-36, 39]. As such, the influence of polyelectrolytes on the structure of water should be investigated as well. The questions that we will address in this thesis are:

1. Do polyelectrolytes possess extended hydration shells?
2. How does the hydration of polyelectrolytes differ from simple electrolytes?
3. Does the extended hydration of polyelectrolytes have a measurable impact on the macroscopic properties of the solutions?

Chapters 4 and 5 are dedicated to answering these questions.

1.4. Lipid membranes, proteins, and hydration

Plasma membranes separate various functions necessary for the survival of an organism into specialized compartments [55]. The plasma membrane is made of two opposing leaflets of polar lipids (a lipid bilayer) decorated with proteins and carbohydrates (shown in Figure 1.2) that facilitate the transport of molecules across the membrane and interact with the surrounding environment [55]. The glycerophospholipids that constitute the majority of the lipid bilayer contain two hydrophobic acyl chains and a polar headgroup [55-57]. The existence of membranes is enabled by the unique properties of water since the formation of lipid bilayer proceeds via self-assembly of water-insoluble lipids driven by the hydrophobic interaction [58-60]. Proper functioning of a membrane thus relies on a fine balance of interactions between the lipids, the proteins, and the interfacial region made mostly of water.

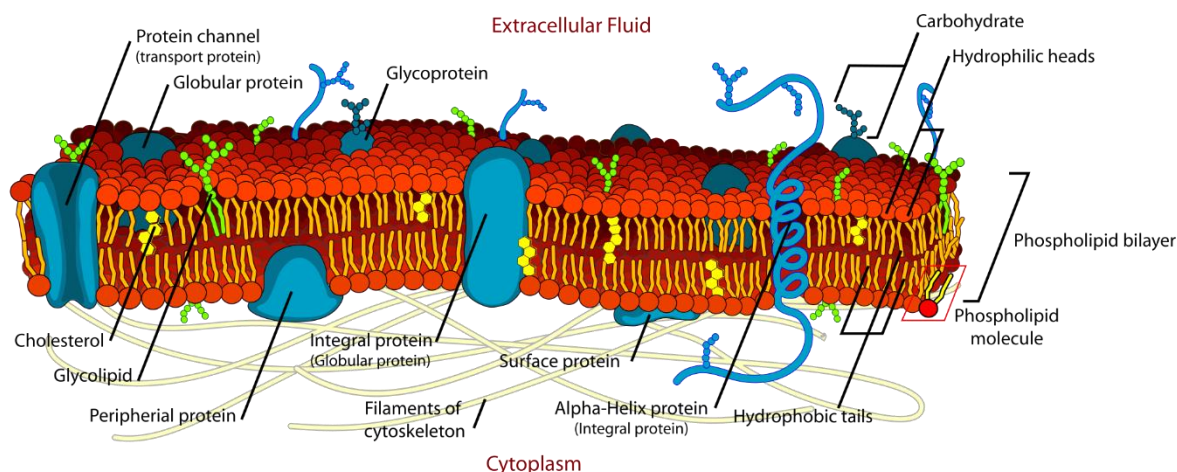


Figure 1.2: Illustration of a cell (plasma) membrane. The membrane is primarily composed of a lipid bilayer and proteins, some of which span across the membrane while others are partially inserted or only bound to the surface of the bilayer. The image is taken from Ref. [61].

The structure of water near the surface of membranes differs from bulk water [62, 63]. This plays a role in membranes' stability and its interactions with the environment [60, 64-66]. The membrane hydration depends on the lipid composition, the surface charge and the composition of the adjacent electrolyte [67-70]. However, characterizing the structure of the interfacial water is experimentally challenging [71]. The membrane-water interface has been studied by techniques such as surface force apparatus [64], atomic force microscopy [62, 63, 72], and molecular dynamics simulations [15, 65]. Recent progress in nonlinear optical imaging and spectroscopy offers a novel approach to probing interfacial phenomena in model biological membranes without resorting to labels or invasive probes [73-75]. This opened a new approach to the study of the electrical double layer [67, 69, 76], the role of hydration in colloid stability [77], surface phase transitions [78], domain formation [79], ion adsorption [80, 81], and transmembrane asymmetry [82].

The lack of molecular-level insight into membrane-protein interactions limits our understanding of cell function or dysfunction. These interactions are typically studied using nuclear magnetic resonance, x-ray crystallography, optical dichroism or fluorescence assays that are not inherently surface-specific and do not provide information about the hydration environment [83]. The role of water in membrane-protein interaction warrants investigation since hydration influences both protein and membrane dynamics [15, 84]. This problem can be addressed experimentally using nonlinear optical techniques which have already been employed to study the secondary structure of proteins at interfaces [85, 86]. Therefore, in Chapter 5 of this thesis we aim to address the following questions:

1. What are the impact of protein adsorption on the hydration environment and surface electrostatics of a liposome?
2. Does second-harmonic scattering provide information about the structure of the adsorbed protein?

1.4.1. Model lipid membranes and lipid chemistry

To perform studies on lipid membrane models, we use small unilamellar vesicles (liposomes) dispersed in aqueous saline solutions. Other existing membrane models include planar monolayers, freestanding bilayers, supported bilayers and giant unilamellar vesicles (Figure 1.3). The planar membranes represent the traditional approach to membrane studies [87]. Lipid monolayers can be prepared at the air/water interface in a Langmuir trough which provides direct control over lateral pressure [88]. The disadvantage of this approach is the large volume of sample required, on the order of 10-100 mL. Another disadvantage is the contact of the sample with air which can lead to contamination or oxidation [88]. Freestanding or supported bilayers immersed in water remedy this issue. However, freestanding bilayers are fragile which complicates long-term measurements. Moreover, probing freestanding bilayers by light reflection (imaging or spectroscopy) is inefficient due to the small refractive index contrast between the bilayer and the solvent. Supported bilayer do not suffer from these issues and are the preferred approach for reflection spectroscopic techniques [89]. One drawback of supported bilayers is a distortion induced in the membrane by the support which affects the lipid transition temperature and significantly increases the transmembrane lipid diffusion rate [90]. The disadvantage shared by all planar membrane models is the lack of curvature which may impact certain membrane functions [91, 92]. Another difference in favor of dispersed vesicles over planar membranes is a large surface to volume ratio leading to diminished sensitivity to small amounts of surface-active impurities [93] and to laser-induced heating [94].

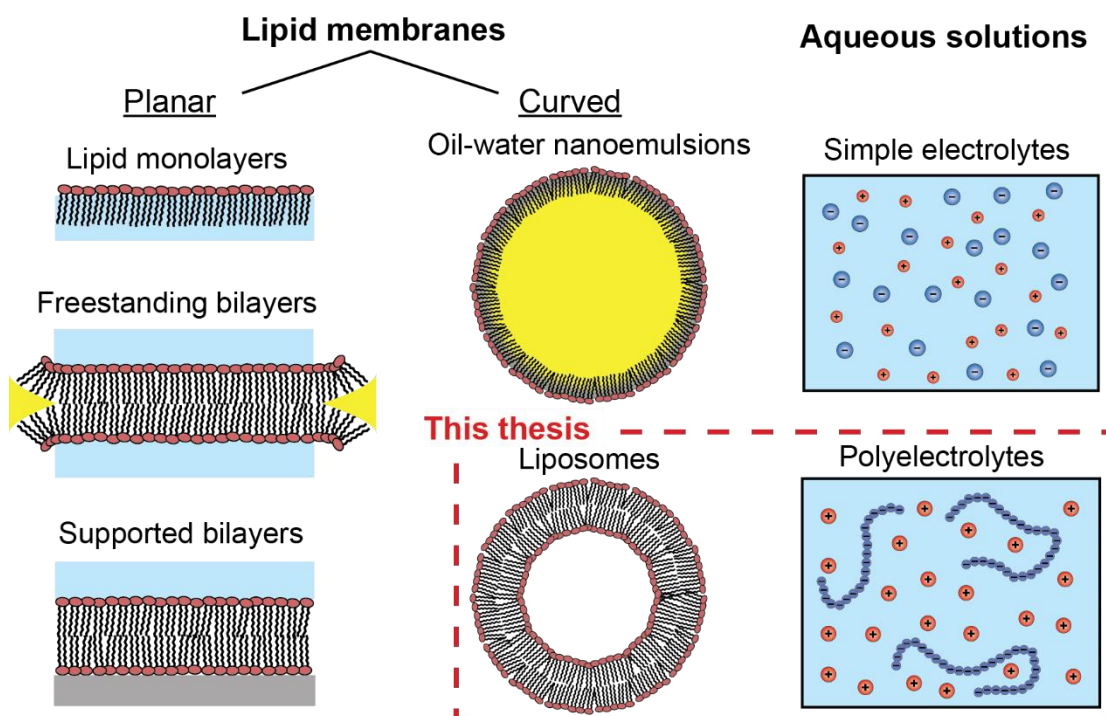


Figure 1.3: Examples of systems that are studied using nonlinear spectroscopic techniques. Left: planar lipid membranes (studied by SHG/SFG in reflection mode). Middle: Spherical lipid membranes (oil nanodroplets and liposomes) studied in a scattering geometry. Right: bulk aqueous solutions (electrolytes, polyelectrolytes) that can be probed by elastic SHS.

The lipid bilayer of a mammalian plasma membrane is asymmetric, with phosphatidylcholine and sphingomyelin found predominantly on the exoplasmic leaflet, whereas phosphatidylserine and phosphatidylethanolamine are concentrated on the cytoplasmic leaflet [95]. To create artificial lipid membranes that can accurately imitate the properties of plasma membranes, therefore, requires not only a precise composition of lipids but also a correct distribution of the lipids across the two membrane leaflets. Supported and freestanding bilayers can easily be made asymmetric during the preparation [79]. Unfortunately, this is not the case for small and large unilamellar vesicles prepared by extrusion where the lipids are automatically scrambled. To overcome this issue, new protocols for liposome asymmetry are being developed that exploit lipid-cyclodextrin complexes to enhance intervesicle lipid trafficking [96, 97]. Cyclodextrins are cyclic oligosaccharides capable of solubilizing hydrophobic molecules in water. They have a wide range of applications spanning from basic membrane research, to flavor encapsulation, drug delivery, and supramolecular chemistry [98-101]. Despite the growing use of cyclodextrins, little is known about their interaction with membranes and lipids. To address this issue, Chapter 6 of this thesis will attempt to provide answers to the following questions:

1. What are the modes of interaction between lipids and cyclodextrin? Does hydration play a role?
2. What is the fate of lipids extracted from membranes by cyclodextrin?

1.5. Nonlinear spectroscopy

1.5.1. Second-order optical nonlinearities

In this thesis, we exploit second-order nonlinear optical effects to measure the structural anisotropy of water and to perform surface-specific measurements. Optical nonlinearities occur at high optical field strengths when the linear relationship between the polarization of a material \mathbf{P} and the incident optical field \mathbf{E} breaks down. In such a case, the macroscopic polarization $\tilde{\mathbf{P}}(t) = \mathbf{P}e^{i\omega t}$ of the material can be expressed as a power series of the incident electric field $\tilde{\mathbf{E}}(t) = \mathbf{E}e^{i\omega t}$ [102]:

$$\tilde{\mathbf{P}}(t) = \varepsilon_0(\chi^{(1)} \cdot \tilde{\mathbf{E}}(t) + \chi^{(2)} : \tilde{\mathbf{E}}(t)^2 + \chi^{(3)} : \tilde{\mathbf{E}}(t)^3 + \dots) \quad (1.1)$$

where $\chi^{(n)}$ is n^{th} order susceptibility tensor. Second-order nonlinearities ($\chi^{(2)} \neq 0$) can be used to generate sum-frequency and second-harmonic signals [102]. In a sum-frequency (SF, Figure 1.4A) process, two optical fields of frequencies ω_1 and ω_2 interact in a material to produce a third optical field with frequency $\omega_0 = \omega_1 + \omega_2$. This process is greatly enhanced for those frequencies (here ω_2) that are in resonance with a real transition in the sample (electronic or vibrational) [102]. Second-harmonic (SH, Figure 1.4B) process is a special case of SF where the two incident fields are of the same frequency, i.e. $\omega_1 = \omega_2$. The energy diagram for a vibrational SF process is shown in Figure 1.4A. Figure 1.4B shows the energy diagram of non-resonant SH generation.

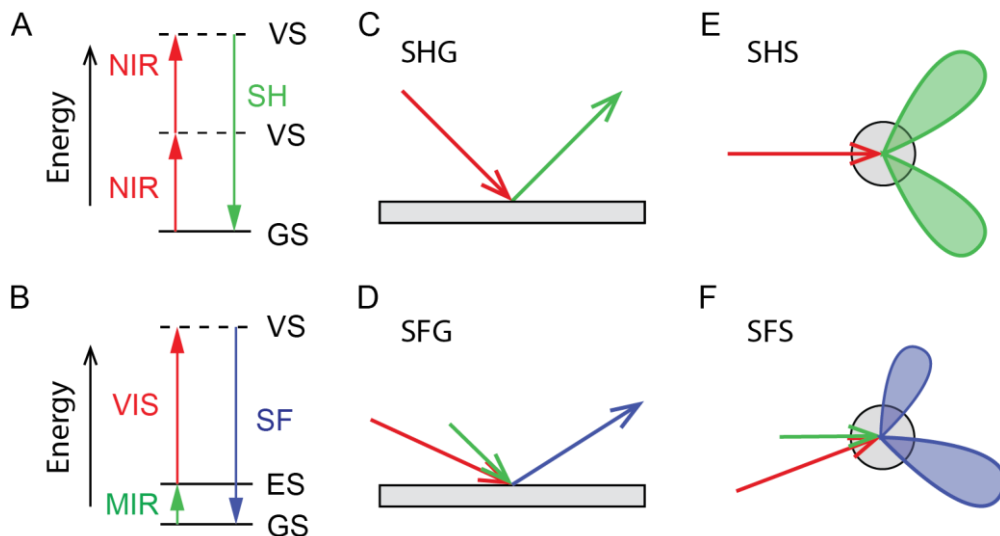


Figure 1.4: Energy diagrams and geometries of second-order spectroscopic techniques. (A) SF is generated by combining a resonant mid-IR optical field (CH stretch modes of alkanes resonate at $\lambda \approx 3400$ nm) and a non-resonant ‘visible’ field ($\lambda \approx 800$ nm corresponds to the output of a Ti:Sa laser). The molecule, therefore, passes from a ground state (GS) to a real excited state (ES) and a virtual state (VS). (B) In an elastic SH process, two photons of the same energy are absorbed by the molecule which passes through two virtual states (VS) and instantaneously re-emits light at the SH wavelength which is half of the incident wavelength. $\lambda \approx 1028$ nm corresponds to the emission of a Yb:KGW laser. (C) Schema of second-harmonic generation (SHG) from a flat interface in reflection geometry. (D) Sum-frequency generation (SFG) in reflection. (E) Second-harmonic scattering (SHS) in collinear excitation. (F) Sum-frequency scattering (SFS).

Second-order optical processes have one important property that linear processes do not: the $\chi^{(2)}$ tensor vanishes in centrosymmetric media. To simply demonstrate this fact for the instantaneous second-harmonic generation, we can write from Eq. (1.1) for the second-order polarization:

$$\tilde{\mathbf{P}}^{(2)}(t) = \chi^{(2)} : \tilde{\mathbf{E}}(t)^2 \quad (1.2)$$

If we change the sign of the electric field, we also change the sign of the polarization, i.e.:

$$-\tilde{\mathbf{P}}^{(2)}(t) = \chi^{(2)} : [-\tilde{\mathbf{E}}(t)]^2 \quad (1.3)$$

Putting Eqs. (1.2) and (1.3) together, we obtain $\tilde{\mathbf{P}}^{(2)}(t) = -\tilde{\mathbf{P}}^{(2)}(t)$ which implies: $\chi^{(2)} = \mathbf{0}$. In other words, SF and SH processes are allowed only in systems with a noncentrosymmetric distribution of material. This property, which is common to all even-order nonlinearities, can be exploited to perform surface-specific spectroscopy and to measure the orientational order (structural anisotropy) of liquids.

The macroscopic second-order susceptibility $\chi^{(2)}$ is a function of the molecular hyperpolarizability $\beta^{(2)}$, the orientational distribution and the number density of the molecules [102]. The molecular hyperpolarizability is

$$\beta^{(2)} = \beta_{NR}^{(2)} + \sum_q \frac{\beta^q}{\omega - \omega_q + i\gamma_q} \quad (1.4)$$

Where the term $\beta_{NR}^{(2)}$ represents a nonresonant background and the term in the sum represents resonances at frequencies ω_q , with damping constants γ_q . The elements of the β^q tensor are proportional to the product:

$$\beta_{ijk}^q \propto \frac{\partial \alpha_{ij}}{\partial Q_q} \frac{\partial \mu_k}{\partial Q_q} \quad (1.5)$$

Where $\frac{\partial \alpha_{ij}}{\partial Q_q}$ and $\frac{\partial \mu_k}{\partial Q_q}$ are the changes in the polarizability and the dipole moment respectively of the molecule vibrating along the normal coordinate Q_q . In other words, for a vibrational mode to be SF-active, it must be simultaneously Raman-active ($\frac{\partial \alpha_{ij}}{\partial Q_q} \neq 0$) and IR-active ($\frac{\partial \mu_k}{\partial Q_q} \neq 0$) [103].

Nonlinear spectroscopy can be realized in various geometries. The reflection geometry (Figure 1.4C, D) where the incident and reflected beams are phase-matched and lie in the same half-plane, was developed to probe planar interfaces. The reflected light is emitted in a narrow range of angles. The scattering geometry (Figure 1.4E, F) is optimal for probing solutions and dispersions. In the scattering geometry, the generated light is emitted in a broad distribution of angles (scattering patterns) which deviate from the phase-matching direction due to the coherent addition of signal over the surface of a small particle [104]. The theoretical treatment of reflection and scattering are similar and on a fundamental (molecular) level, the reflection and scattering processes are identical. Here, we provide a historical overview and state of the art in nonlinear spectroscopic techniques. The theoretical framework of nonlinear scattering is described in the following chapter.

1.5.2. Reflection from planar interfaces

The first SH generation (SHG, Figure 1.4C) in a crystal was demonstrated by Franken et al in 1961 [105]. This was allowed by the invention of the ruby laser one year before by Maiman [106]. The theory of SHG was originally developed by Bloembergen and Pershan in 1962 [107], and subsequently improved in the following years [108-110]. In 1973 SH reflection from a surface was first reported [111]. The use of SHG in the reflection geometry for the study of molecular orientation and adsorption at planar liquid-air interfaces was developed in the 1980s [112-114]. Elastic (non-resonant) SHG from the water-silica interface was first demonstrated by Ong et al. in 1992 [115]. Vibrational SF generation (SFG, Figure 1.4D) was developed in 1987 [116, 117]. The latest technical developments in SFG include 2D (pump-probe) measurements shown in 2006 [118], heterodyne-detection for phase-sensitive measurements in 2007 [119], and the combination of the two in 2012 [120]. The complexity of the systems studied by SHG and SFG has been increasing. Recently, chiral SHS measurements have revealed the presence of chiral water in the minor groove of DNA and in artificial membrane

channels [121, 122] and chiral SFG has been employed to determine the secondary structures of surface-bound proteins [123].

1.5.3. Scattering from colloidal dispersions

Although in 1969 Terhune et al reported the first case of SH scattering (SHS, Figure 1.4E) from crystals and liquids [124], the use of resonant SHS for probing particle interfaces was first demonstrated only in 1996 [125] and vibrational SF scattering (SFS, Figure 1.4F) was introduced 7 years later in 2003 [126]. In 1998 Yan et al reported on elastic (non-resonant) SHS from polystyrene sulfate particles in water and showed a relation between the surface potential and SHS intensity [127]. The first SHS study of liposomes was presented by the same group 3 years later [128]. Another improvement to SHS was angle-resolved (AR) SHS measurements demonstrated in 2010 [129]. Elastic SHS has recently been employed to probe the order of interfacial water at the surfaces of nanoparticles [67, 77, 82, 130-136]. A recent extension of the theory of SHS from charged interfaces significantly improved the agreement between the theory and the experimental data [137]. This allowed an unambiguous determination of the surface potential of liposomes in water [69, 76]. Unlike elastic SHS which probes all molecules in the sample simultaneously, vibrational SFS can measure specific molecular vibrations [126]. It has been employed for the study of the interfacial structure of oil-water emulsions [67, 77, 135, 136, 138-140] and liposomes [82]. The developments and applications of SHG/SHS and SFG/SFS have been summarized in many reviews [73-75, 86, 114, 141-144].

1.5.4. Hyper-Rayleigh scattering and coherent SHS from bulk liquids

SHS occurs not only at interfaces but also in homogeneous solutions of molecules with a noncentrosymmetric electronic structure, such as water. SHS from bulk liquids was first reported in 1965 [124]. The theory of SHS from liquids was developed by Cyvin [145], and subsequently improved by Bersohn [146] and Kauranen and Persoons [147]. Uncorrelated noncentrosymmetric molecules generate incoherent SHS, also referred to as hyper-Rayleigh scattering (HRS) [143]. The HRS intensity is linearly proportional to the number density of the molecules [148]. The emission of light at the second-harmonic frequency can be enhanced if the molecules in the liquid are spatially correlated. This leads to constructive interference of signals from distant molecules. [146]. In the case of coherent SHS, the intensity scales quadratically with the number density of the correlated molecules [143]. SHS has been used to study long-range correlations in aqueous electrolyte solutions [40, 41, 149]. The orientational order in water arises from ion-water and H-bonding interactions. Isotope

exchange experiments ($\text{H}_2\text{O} \rightarrow \text{D}_2\text{O}$) have shown that the H-bond network of water acts against the order induced by the presence of ions [41]. SHS can therefore be used to probe water-water correlations, the influence of various substances on the orientational order of water, and the role of nuclear quantum effects in water [18, 150-152].

1.6. The structure of this thesis

This thesis is divided into 7 chapters. The core of the thesis is Chapters 3 - 6 each of which was adapted from a manuscript (published or in preparation for publication). The first part (Chapters 3 - 4) presents studies of aqueous polyelectrolyte solutions using SHS and viscosity measurements. The second part (Chapters 5 - 6) concerns the studies of molecular interactions with liposomes as models of lipid membranes using SHS, SFS and other supporting techniques. The systems under investigation here compared to other systems studied by nonlinear spectroscopy are illustrated in Figure 1.3.

The chapters are structured as follows:

- Chapter 2 provides the theory for the used experimental techniques: second-harmonic scattering (SHS), sum-frequency scattering (SFS), dynamic light scattering (DLS), and electrophoretic mobility measurements. The physical implementation of the nonlinear scattering techniques is described as well.
- Chapter 3 presents the SHS measurements of polyelectrolyte (hyaluronan) solutions. The origin of the SH response is discussed and compared to that of electrolytes and charged particles. A modified model of SHS from charged particles is proposed to explain the observed SH response. Temperature dependence of the SHS is also measured and discussed.
- In Chapter 4 we present viscosity and SHS measurement of polyelectrolyte solution. We show a correlation between SHS response and the reduced specific viscosity of the solutions. The observed increase in the reduced viscosity and SHS is explained as originating from enhanced orientational order in the bulk water due to the presence of highly charged polyelectrolytes.
- Chapter 5 presents a study of the binding of the protein α -Synuclein to cationic liposomes using SHS, DLS and electrophoretic mobility measurements. The protein binding is shown to have no effect on the surface and zeta potentials. Its presence at the liposome surface leads to a decrease in the orientational order of interfacial water which is seen as a decrease in SHS intensity.
- In Chapter 6 we study the interaction between various liposomes and methyl- β -cyclodextrin using SFS, SHS, DLS and electrophoretic mobility measurements. SFS

measurements show that cyclodextrin is selective to lipid headgroups. SHS reveals that cyclodextrin-lipid complexes self-assemble into fibers. A water isotope exchange indicates that hydration plays a role in the self-assembly process.

- Chapter 7 provides a summary of the thesis and an outlook on the possibilities for future research based on the work presented here.

Chapter 2: Experimental details and methodology

This chapter provides an overview of the principal methods used in this thesis. The core of the chapter is dedicated to the theory of second-order nonlinear scattering, including a discussion of special cases, and calculated examples. The physical implementations of second-harmonic and sum-frequency employed are described in detail. The final sections of the chapter are dedicated to a brief overview of the supporting techniques - dynamic light scattering and electrophoretic mobility measurements.

2.1. Theory of nonlinear scattering

The following section develops the theoretical basis of the two nonlinear optical methods used in this thesis: sum-frequency scattering (SFS) and second-harmonic scattering (SHS). The first part concerns the derivation of general formulas for sum-frequency scattering from the surface of centrosymmetric spherical particles in a centrosymmetric medium. This is followed by a derivation of formulas for elastic second-harmonic scattering. We also derive scattering formulas for charged particles in a polarizable medium which involves an additional third-order effect allowing optical measurement of the surface potential. Lastly, we provide a theory of SH scattering from cylindrical particles with bulk noncentrosymmetry and a method of calculating the scattered intensity of randomly oriented particles.

2.1.1. Assumptions

One possible starting point for calculating the scattered electromagnetic fields is to invoke the reciprocity theorem [153, 154]. If we have an oscillating polarization distribution \mathbf{P} , the electric field generated by this polarization at a distant point \mathbf{r}_0 , $\mathbf{E}(\mathbf{r}_0)$, will resemble a spherical wave. The theorem states that, by reversing the flow of time, this is equivalent to the electric field \mathbf{E}' of a spherical wave back-propagating from the point \mathbf{r}_0 and inducing a linear polarization \mathbf{u} . The product $\mathbf{P} \cdot \mathbf{E}'$ integrated over all space describes the contribution of the polarization \mathbf{P} to an electric field detected at the far-field point \mathbf{r}_0 . Formally, this relationship is given by:

$$\mathbf{E}(\mathbf{r}_0) \cdot \mathbf{u} = e^{ik_0 r_0} \frac{k_0^2}{r_0} \int i\omega \mathbf{P}(\mathbf{r}') \cdot \mathbf{E}'(\mathbf{r}') d^3\mathbf{r}' \quad (2.1)$$

Where k_0 is the wavenumber of the real electromagnetic wave $\mathbf{E}(\mathbf{r}_0)$ in the far-field, while \mathbf{E}' is the theoretical spherical wave returning from the point \mathbf{r}_0 . The integral is evaluated over the volume of the particle. For second-order interactions, the polarization is given by [102]:

$$\mathbf{P}(\mathbf{r}') = \chi^{(2)}(\mathbf{r}') : \mathbf{E}_1(\mathbf{r}') \mathbf{E}_2(\mathbf{r}') \quad (2.2)$$

where $\mathbf{E}_i(\mathbf{r}')$ are the local electric fields in the particle which are related to the incident electromagnetic fields. The Mie theory provides an exact solution to this problem by properly expressing the local electric fields in vector spherical harmonics [155] and has been adapted to nonlinear scattering as well [156-158]. To simplify the calculations, we use the Rayleigh-Gans-Debye (RGD) approximation which assumes that the incident light is neither reflected at the particle surface nor attenuated inside the particle. This is expressed by the conditions [159]:

$$\begin{aligned} \left|1 - \frac{n_p}{n_s}\right| &\ll 1 \\ \frac{2\pi}{\lambda} d \left|1 - \frac{n_p}{n_s}\right| &\ll 1 \end{aligned} \quad (2.3)$$

where n_p and n_s are the refractive indices of the particle and the solvent, λ is the wavelength of out outgoing light, and d is the particle's diameter. We can verify that this condition is easily satisfied for large unilamellar vesicles ($n_p = 1.4$, $d = 120$ nm) in water ($n_s = 1.332$) probed using the second-harmonic of a Yb:KGW laser (514 nm) for which $\left|1 - \frac{n_p}{n_s}\right| = 0.05$ and $\frac{2\pi}{\lambda} d \left|1 - \frac{n_p}{n_s}\right| = 0.08$.

2.1.2. Symmetries

To further simplify the calculation of the scattered fields, we can make use of symmetries of the system under study. For centrosymmetric particles embedded in a centrosymmetric medium, such as water, the $\chi^{(2)}$ tensor will be non-zero only at the particle-solvent interface [102] as illustrated in Figure 2.1A. We can, therefore, define the surface second-order susceptibility tensor as $\chi_s^{(2)}(\mathbf{r}') = \chi^{(2)}(\mathbf{r}')\delta(|\mathbf{r}'| - R)$, where δ is the dirac delta function and R is the particle radius. The i^{th} component of the second-order polarization oscillating at the frequency $\omega_0 = \omega_1 + \omega_2$ is then equal to [102]:

$$\tilde{P}_i^{(2)}(\omega_0) = \varepsilon_0 \chi_{s,ijk}^{(2)}(\omega_0, \omega_1, \omega_2) \tilde{E}_j(\omega_1) \tilde{E}_k(\omega_2) \quad (2.4)$$

To further simplify the problem, we can take into account the symmetries of the surface itself which will eliminate certain elements of the $\chi_s^{(2)}$ tensor [160]. We will consider two cases here: an achiral isotropic surface (Figure 2.1B) and a chiral isotropic surface (Figure 2.1C).

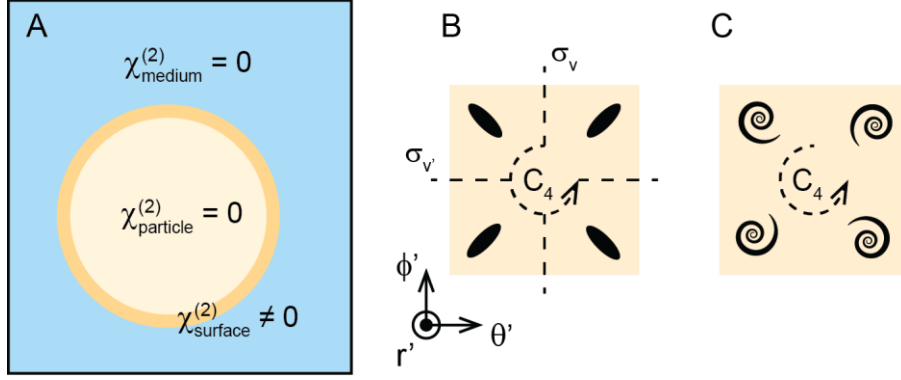


Figure 2.1: Symmetries of a spherical particle. (A) A system composed of a particle made of a centrosymmetric material embedded in a centrosymmetric medium will not generate any second-order response from the bulk of the particle nor from the bulk of the medium due to inversion symmetry. The only place where inversion symmetry is broken is at the particle-medium interface ($\chi_{surface}^{(2)} \neq 0$). (B) View of an achiral isotropic surface. This surface has 3 symmetries: a four-fold rotational symmetry (axis C_4) and two perpendicular reflection planes σ_v and $\sigma_{v'}$ (dashed lines). (C) An illustration of a chiral isotropic surface. This surface has a four-fold rotational symmetry (axis C_4) but lacks reflection symmetry.

Since the surface of a sphere can be locally approximated by a plane, we will use a right-handed Cartesian coordinate system $(\hat{r}', \hat{\theta}', \hat{\phi}')$ for the local surface coordinates where \hat{r}' is a unit vector in the direction normal to the surface and $\hat{\theta}' / \hat{\phi}'$ are mutually orthogonal unit vectors in the plane of the surface. First, let us investigate how $\chi_{s,ijk}^{(2)}$ in equation (2.4) transforms under a four-fold rotation around the r' axis. The transformation matrix for the n^{th} rotation is [161]:

$$D(C_4^n) = \begin{pmatrix} 1 & 0 & 0 \\ 0 & \cos(n\pi/2) & -\sin(n\pi/2) \\ 0 & \sin(n\pi/2) & \cos(n\pi/2) \end{pmatrix} \quad (2.5)$$

The transformed tensor $\chi_{s,lmn}^{(2),tr}$ is then:

$$\chi_{s,lmn}^{(2),tr} = D(C_4^n)_{li} D(C_4^n)_{mj} D(C_4^n)_{lk} \chi_{s,ijk}^{(2)} \quad (2.6)$$

Under a 180° rotation we obtain $\chi_{s,\theta'\theta'\phi'}^{(2),tr} = (-1)(-1)(-1)\chi_{s,\theta'\theta'\phi'}^{(2)} = -\chi_{s,\theta'\theta'\phi'}^{(2)}$ which implies $\chi_{s,\theta'\theta'\phi'}^{(2)} = 0$. The same argument holds for all $\chi_{s,ijk}^{(2)}$ elements where the total number that indices θ' and ϕ' appear is odd (i.e. $\phi'\phi'\phi'$, $\theta'\theta'\theta'$, and all the permutations of $\theta'\theta'\phi'$ and $\theta'\phi'\phi'$). Using a 90° rotation we obtain $\chi_{s,r'\theta'\phi'}^{(2),tr} = (-1)(-1)\chi_{s,r'\phi'\theta'}^{(2)} = \chi_{s,r'\phi'\theta'}^{(2)}$, i.e. $\theta' \leftrightarrow \phi'$ which holds for all 3 permutations of the indices $r'\theta'\theta'$. Lastly, if we apply a 90° rotation to

$\chi_{s,r'\theta'\phi'}^{(2),tr}$ we obtain $-\chi_{s,r'\phi'\theta'}^{(2)}$, i.e. $\phi' \leftrightarrow -\theta'$ for all permutations of $r'\theta'\phi'$. A surface with such symmetry is illustrated in Figure 2.1C.

If the surface is achiral, it contains 2 additional orthogonal planes of mirror symmetry σ_v and $\sigma_{v'}$ (dashed lines in Figure 2.1B). The transformation matrices for σ_v and $\sigma_{v'}$ are:

$$R(\sigma_v) = \begin{pmatrix} 1 & 0 & 0 \\ 0 & -1 & 0 \\ 0 & 0 & 1 \end{pmatrix} \quad R(\sigma_{v'}) = \begin{pmatrix} 1 & 0 & 0 \\ 0 & 1 & 0 \\ 0 & 0 & -1 \end{pmatrix} \quad (2.7)$$

If we apply these symmetry operations to the element $\chi_{s,r'\phi'\theta'}^{(2)}$ we obtain $-\chi_{s,r'\phi'\theta'}^{(2)}$, implying $\chi_{s,r'\phi'\theta'}^{(2)} = 0$. The same holds for any permutation of $r'\phi'\theta'$. The tensor elements $\chi_{s,ijk}^{(2)}$ where ijk is a permutation of $r'\phi'\theta'$ are referred to as chiral [160].

2.1.3. Vibrational sum-frequency scattering

Our goal here is to calculate the electric field components of a wave scattered from the surface of a spherical particle. The geometry of the problem is illustrated in Figure 2.2A (perspective) and B (top view). To calculate the scattered electromagnetic field, the local surface response described by $\chi_s^{(2)}$ must be integrated over the surface of the particle. We can include the combined symmetry of the particle and the electromagnetic field into one term, the effective second-order susceptibility $\Gamma^{(2)}$. This allows us to write the following relationship between the incident and scattered electromagnetic fields detected at a distance r_0 from the source [153, 162]:

$$E_0 = \alpha E_1 E_2 \sum_{a_0 a_1 a_2} \Gamma_{a_0 a_1 a_2}^{(2)} \prod_{i=0}^2 (\hat{q}_{a_i} \cdot \hat{u}_{i,l}) \quad (2.8)$$

with

$$\alpha = \frac{ic k_0^3}{2\pi |\hat{r}| |\hat{I}|} \frac{e^{ik_0 r_0}}{r_0} \quad (2.9)$$

where $|\hat{r}|$ is the unit distance and $|\hat{I}|$ is the unit current. The unit polarization vectors $\hat{u}_{i,l}$ are defined as:

$$\hat{u}_{0,p} = (\sin \theta, 0, \cos \theta) \quad (2.10)$$

$$\hat{\mathbf{u}}_{1,p} = (\cos(\beta - \alpha), 0, \sin(\beta - \alpha))$$

$$\hat{\mathbf{u}}_{2,p} = (\cos \alpha, 0, -\sin \alpha)$$

$$\hat{\mathbf{u}}_{0,s} = \hat{\mathbf{u}}_{1,s} = \hat{\mathbf{u}}_{2,s} = (0, 1, 0)$$

where the subscript i denotes the beam (0 = SF, 1 = VIS, 2 = IR) and the subscript l stands for polarization direction (p-parallel or s-perpendicular with respect to the scattering plane xz).

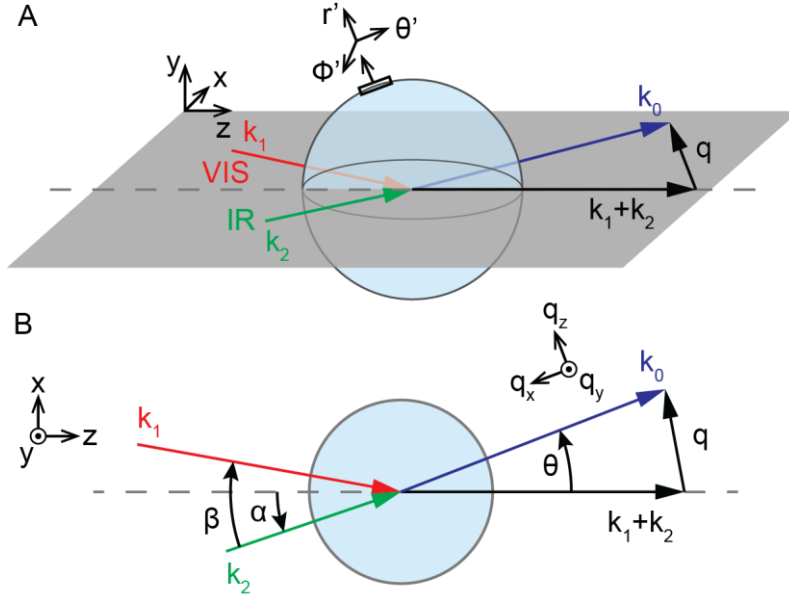


Figure 2.2: Geometry of the sum-frequency scattering process. (A) Perspective view. (B) Top view. There are 3 beams involved with their associated wave vectors, these are in order of decreasing frequency: sum-frequency (SF) – \mathbf{k}_0 , visible (VIS) – \mathbf{k}_1 and infrared (IR) – \mathbf{k}_2 . There are also 3 coordinate systems: 1. A Cartesian laboratory frame $(\hat{\mathbf{x}}, \hat{\mathbf{y}}, \hat{\mathbf{z}})$ with $\hat{\mathbf{z}} \parallel \mathbf{k}_1 + \mathbf{k}_2$ (the phase matching direction). 2. A rotated Cartesian frame $(\hat{\mathbf{q}}_x, \hat{\mathbf{q}}_y, \hat{\mathbf{q}}_z)$ where $\hat{\mathbf{q}}_z \parallel \mathbf{q}$ (the scattering wave vector) 3. A particle surface frame defined in spherical coordinates $(\hat{\mathbf{e}}_{r'}, \hat{\mathbf{e}}_{\theta'}, \hat{\mathbf{e}}_{\phi'})$. The xz plane is the scattering plane in which all 3 wave vectors ($\mathbf{k}_1, \mathbf{k}_2, \mathbf{k}_0$) are placed. The scattering angle θ is the angle between \mathbf{k}_0 and $\mathbf{k}_1 + \mathbf{k}_2$. Beams polarized in the scattering plane are referred to as p-polarized, while beams polarized perpendicular to the plane are referred to as s-polarized. The polarization combination of all 3 beams is described by a 3-letter code in order of decreasing frequency, e.g. pss = SF p-polarized, VIS s-polarized, and IR s-polarized.

The element $a_0 a_1 a_2$ of the effective second-order susceptibility of a spherical particle with a radius R is [162]:

$$\Gamma_{a_0 a_1 a_2}^{(2)} = \sum_{c_0 c_1 c_2} \int d\mathbf{r}'^3 \left\{ \chi_{c_0 c_1 c_2}^{(2)} \delta(|\mathbf{r}'| - R) e^{-i\mathbf{q} \cdot \mathbf{r}'} \prod_{i=0}^2 (\hat{\mathbf{e}}_{c_i} \cdot \hat{\mathbf{q}}_{a_i}) \right\} \quad (2.11)$$

For a spherical particle, the coordinates are (r', θ', φ') with the range: $r' \in [0, R]$, $\theta' \in [0, \pi]$ and $\varphi' \in [0, 2\pi]$ and $d\mathbf{r}'^3 = r'^2 dr' \sin \theta' d\theta' d\varphi'$. The relationship between the unit vectors of the rotated Cartesian frame $(\hat{\mathbf{q}}_x, \hat{\mathbf{q}}_y, \hat{\mathbf{q}}_z)$ and those of the particle's Spherical coordinate frame $(\hat{\mathbf{e}}_{r'}, \hat{\mathbf{e}}_{\theta'}, \hat{\mathbf{e}}_{\varphi'})$ is:

$$\begin{pmatrix} \hat{\mathbf{e}}_{r'} \\ \hat{\mathbf{e}}_{\theta'} \\ \hat{\mathbf{e}}_{\varphi'} \end{pmatrix} = \begin{pmatrix} \sin \theta' \cos \varphi' & \sin \theta' \sin \varphi' & \cos \theta' \\ \cos \theta' \cos \varphi' & \cos \theta' \sin \varphi' & -\sin \theta' \\ -\sin \varphi' & \cos \varphi' & 0 \end{pmatrix} \begin{pmatrix} \hat{\mathbf{q}}_x \\ \hat{\mathbf{q}}_y \\ \hat{\mathbf{q}}_z \end{pmatrix} \quad (2.12)$$

The scattering wave vector is defined as $\mathbf{q} \equiv \mathbf{k}_0 - (\mathbf{k}_1 + \mathbf{k}_2)$ and its magnitude is $q(\theta) = 2k_0 \sin(\theta/2)$. The wave vectors are defined as:

$$\begin{aligned} \mathbf{k}_0 &= k_0(\sin \theta, 0, \cos \theta) \\ \mathbf{k}_1 &= k_1(-\sin(\beta - \alpha), 0, \cos(\beta - \alpha)) \\ \mathbf{k}_2 &= k_2(\sin \alpha, 0, \cos \alpha) \\ \mathbf{k}_1 + \mathbf{k}_2 &= |\mathbf{k}_1 + \mathbf{k}_2|(0, 0, 1) \end{aligned} \quad (2.13)$$

$\chi_s^{(2)}$ is a third-rank tensor with $3^3 = 27$ elements. As was shown in the previous section, there are only 7 independent, non-zero $\chi_s^{(2)}$ elements that can be divided into achiral and chiral. The calculations can be further simplified if we re-define the 7 susceptibility elements in the following manner: $\chi_{s,1}^{(2)} = \chi_{rrrrr} - \chi_{\theta'\theta'r'} - \chi_{\theta'r'\theta'} - \chi_{r'\theta'\theta'}$, $\chi_{s,2}^{(2)} = \chi_{\theta'\theta'r'}$, $\chi_{s,3}^{(2)} = \chi_{\theta'r'\theta'}$, $\chi_{s,4}^{(2)} = \chi_{r'\theta'\theta'}$, $\chi_{s,5}^{(2)} = \chi_{r'\theta'\phi'}$, $\chi_{s,6}^{(2)} = \chi_{\theta'\phi'r'}$, $\chi_{s,7}^{(2)} = \chi_{\phi'r'\theta'}$.

By solving Eq. (2.8) for all 8 polarization combinations of the sum-frequency, visible and IR beams, we obtain the following expressions for the intensity of the emitted electromagnetic field in the 8 polarization combinations [137, 162]:

$$\begin{aligned} E_{ppp} &= \alpha \left[\cos\left(\frac{\theta}{2}\right) \cos\left(\frac{\theta}{2} - \alpha\right) \cos\left(\frac{\theta}{2} - \alpha + \beta\right) \right] \Gamma_1^{(2)} \\ &\quad + \cos(\theta - \alpha + \beta)E_{ssp} + \cos(\theta - \alpha)E_{sps} + \cos(\beta)E_{pss} \\ E_{ssp} &= \alpha \cos\left(\frac{\theta}{2} - \alpha\right) \Gamma_2^{(2)} \\ E_{sps} &= \alpha \cos\left(\frac{\theta}{2} - \alpha + \beta\right) \Gamma_3^{(2)} \\ E_{pss} &= \alpha \cos\left(\frac{\theta}{2}\right) \Gamma_4^{(2)} \end{aligned} \quad (2.14)$$

$$\begin{aligned}
E_{pps} &= \frac{\alpha}{2} \left\{ -F_{ch,1} \left[\chi_5 \cos\left(\frac{\theta}{2}\right) \sin\left(\alpha - \beta + \frac{\theta}{2}\right) + \chi_7 \cos\left(\alpha - \beta + \frac{\theta}{2}\right) \sin\left(\frac{\theta}{2}\right) \right] \right. \\
&\quad \left. + F_{ch,2} (\chi_5 + \chi_6 + \chi_7) \sin(\alpha - \beta + \theta) \right\} \\
E_{psp} &= \frac{\alpha}{2} \left\{ F_{ch,1} \left[\chi_6 \cos\left(\alpha - \frac{\theta}{2}\right) \sin\left(\frac{\theta}{2}\right) - \chi_5 \cos\left(\frac{\theta}{2}\right) \sin\left(\alpha - \frac{\theta}{2}\right) \right] \right. \\
&\quad \left. + F_{ch,2} (\chi_5 + \chi_6 + \chi_7) \sin(\alpha - \theta) \right\} \\
E_{spp} &= \frac{\alpha}{4} \left\{ [F_{ch,1} (\chi_6 + \chi_7) - 2F_{ch,2} (\chi_5 + \chi_6 + \chi_7)] \sin(2\alpha - \beta) \right. \\
&\quad \left. + F_{ch,1} (\chi_7 - \chi_6) \sin(\beta - \theta) \right\} \\
E_{sss} &= 0
\end{aligned}$$

Where the elements of $\Gamma_n^{(2)}$ are defined by the matrix:

$$\begin{pmatrix} \Gamma_1^{(2)} \\ \Gamma_2^{(2)} \\ \Gamma_3^{(2)} \\ \Gamma_4^{(2)} \end{pmatrix} = \begin{pmatrix} 2F_1 - 5F_2 & 0 & 0 & 0 \\ F_2 & 2F_1 & 0 & 0 \\ F_2 & 0 & 2F_1 & 0 \\ F_2 & 0 & 0 & 2F_1 \end{pmatrix} \begin{pmatrix} \chi_{s,1}^{(2)} \\ \chi_{s,2}^{(2)} \\ \chi_{s,3}^{(2)} \\ \chi_{s,4}^{(2)} \end{pmatrix} \quad (2.15)$$

with the form factors $F_1 = 2\pi i R^2 \left(\frac{\sin(qR)}{(qR)^2} - \frac{\cos(qR)}{qR} \right)$, $F_2 = 4\pi i R^2 \left(3 \frac{\sin(qR)}{(qR)^4} - 3 \frac{\cos(qR)}{(qR)^3} - \frac{\sin(qR)}{(qR)^2} \right)$, $F_{ch,1} = 8\pi R^2 \left(3 \frac{\cos(qR)}{(qR)^2} - 3 \frac{\sin(qR)}{(qR)^3} + \frac{\sin(qR)}{qR} \right)$, and $F_{ch,2} = 8\pi R^2 \left(\frac{\cos(qR)}{(qr)^2} - \frac{\sin(qR)}{(qR)^3} \right)$. The optical intensity measured at the sum frequency ω_0 in the polarization combination xyy is $I_{xyy}(\omega_0) = |E_{xyy}^{(2)}|^2$. For an achiral surface (i.e. $\chi_{s,5}^{(2)} = \chi_{s,6}^{(2)} = \chi_{s,7}^{(2)} = 0$), there will be no signal in the polarization combinations spp, psp and pps in Eq. (2.14), that is:

$$E_{pps} = E_{psp} = E_{spp} = 0 \quad (2.16)$$

Calculated scattering patterns based on Eqs. (2.14) for a particle $R = 100$ nm, in water ($n = 1.333$) with wavelengths $\lambda_1 = 800$ nm, $\lambda_2 = 3400$ nm, and surface susceptibility elements $\chi_1 = 0$, $\chi_2 = 1$, $\chi_3 = 0.5$, $\chi_4 = 0.5$, $\chi_5 = 0.1$, $\chi_6 = 1$, $\chi_7 = 0$ are shown in Figure 2.3.

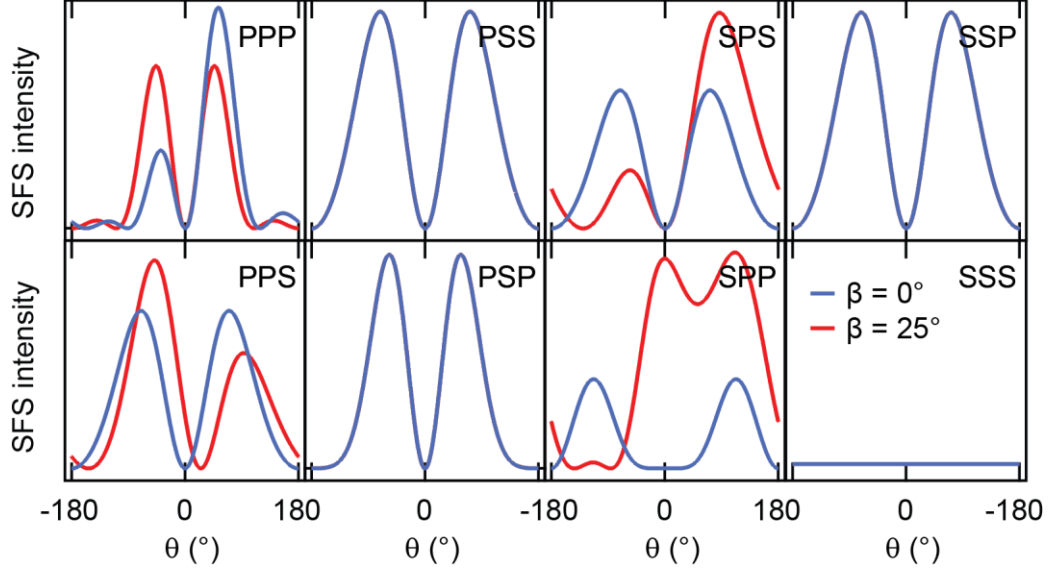


Figure 2.3: Theoretically calculated SF scattering patterns. The patterns in all 8 polarization combinations of the SF, VIS, and IR beams are calculated from Eqs. (2.14). The parameters used for the calculation are: $R = 100$ nm, $n = 1.332$, $\lambda_1 = 800$ nm, $\lambda_2 = 3400$ nm, $\chi_1 = 0$, $\chi_2 = 1$, $\chi_3 = 0.5$, $\chi_4 = 0.5$, $\chi_5 = 0.1$, $\chi_6 = 1$, $\chi_7 = 0$, $\alpha = 0^\circ$. The blue curves show collinear excitation ($\beta = 0^\circ$) while red curves show non-collinear excitation ($\beta = 25^\circ$).

We can see from Eqs. (2.14) and (2.16) that polarization combinations ppp, ssp, sps, pss probe exclusively achiral elements of $\chi_s^{(2)}$ while polarization combinations spp, psp, and pps probe only chiral ones. Moreover, achiral emission is modulated by form-factors F_1 and F_2 , while chiral emission is modulated $F_{ch,1}$ and $F_{ch,2}$ which will lead to different angular distributions of the scattered SF field for chiral and achiral signals. For example, chiral emission produces a response in the forward direction ($\theta = 0^\circ$) under non-collinear excitation while this is never the case for achiral signals or under collinear excitation, as can be seen in Figure 2.3. The sss polarization combination does not contain any coherent signal for spherical particles, regardless of chirality. The relationships between the polarization combinations, the form factors and the elements of $\chi_s^{(2)}$ are summarized in a chart in Figure 2.4.

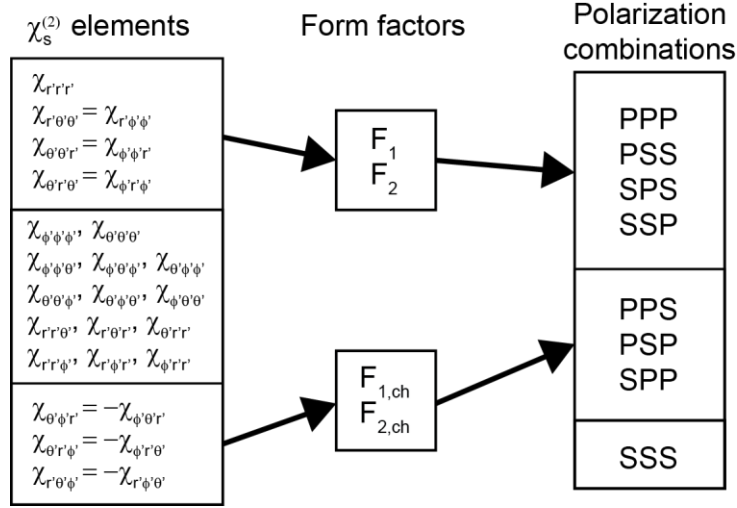


Figure 2.4: A chart showing the contributions of the surface susceptibility elements ($\chi_s^{(2)}$) and the four form factors to the 8 possible polarization combinations.

The above equations were derived with the assumption that the scattering object is a sphere with an isotropic surface. For a non-spherical scattering object, the achiral $\chi_{s,1}^{(2)}$ element can contribute all 8 polarization combinations [162].

2.1.4. Elastic second-harmonic scattering from bulk liquids

In an elastic second-harmonic experiment the wavelength of light used is far from any resonance of any molecule in the sample. All non-centrosymmetric molecules in the probed volume of the sample, therefore, generate SH intensity of approximately the same magnitude [102]. The second-order polarization of each molecule oscillating at 2ω is [102]:

$$\tilde{\mathbf{p}}^{(2)}(2\omega) = \boldsymbol{\beta}^{(2)} : \tilde{\mathbf{E}}(\omega) \tilde{\mathbf{E}}(\omega) \quad (2.17)$$

where $\boldsymbol{\beta}^{(2)}$ is the molecular second-order hyperpolarizability tensor. The macroscopic second-order susceptibility $\chi^{(2)}$ is an orientational average of molecular hyperpolarizability $\boldsymbol{\beta}^{(2)}$ [102]:

$$\chi_{ijk}^{(2)} = \frac{N_m}{\epsilon_0} \langle T_{il}(\xi) T_{jm}(\psi) T_{kn}(\zeta) \rangle_{\xi, \psi, \zeta} \beta_{lmn}^{(2)} \quad (2.18)$$

where N_m is the number density of molecules, T are transformation (rotation) matrices between the molecular frame (a,b,c) and the lab frame (x,y,z), and $\langle \dots \rangle_{\xi, \psi, \zeta}$ denotes an averaging operation over the angles ξ , ψ , and ζ . The symmetry properties of the $\boldsymbol{\beta}^{(2)}$ tensor are identical

to the symmetry of the molecule itself [161]. The H₂O molecule in a Cartesian frame (a,b,c) is illustrated in Figure 2.5.

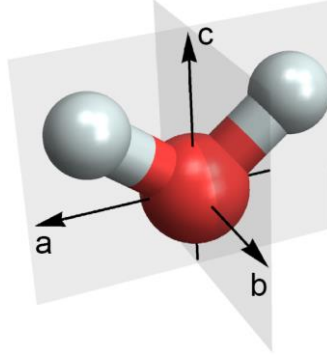


Figure 2.5: H₂O molecule shown in a Cartesian coordinate system (a,b,c) used for the calculation of the symmetry of its $\beta^{(2)}$ tensor. H₂O belongs to the point symmetry group C_{2v}. It possesses a 2-fold rotation axis (c-axis), and two reflection planes (ac and bc, shown in gray).

For H₂O (point symmetry group C_{2v}), the non-zero elements of $\beta^{(2)}$ are: $\beta_{aac}^{(2)}$, $\beta_{aca}^{(2)}$, $\beta_{caa}^{(2)}$, $\beta_{bbc}^{(2)}$, $\beta_{bcb}^{(2)}$, $\beta_{cbb}^{(2)}$, $\beta_{ccc}^{(2)}$ [163]. Assuming that the dispersion of the fundamental and second-harmonic wave are the same under non-resonant conditions, we can assume full permutation symmetry of the tensor and write the following relations for the $\beta^{(2)}$ elements [102]:

$$\beta_{aac}^{(2)} = \beta_{aca}^{(2)} = \beta_{caa}^{(2)}$$

$$\beta_{bbc}^{(2)} = \beta_{bcb}^{(2)} = \beta_{cbb}^{(2)}$$

In an elastic SHS experiment, the detected intensity is the squared sum of all the electric fields \tilde{E}_ν emitted by the molecules ν in the probed volume. The sum can be divided into a self-correlation (quadratic) part and a cross-correlation (interference) part:

$$\begin{aligned} I(2\omega) &= \frac{cn\epsilon_0}{2} \left| \sum_{\nu} \tilde{E}_{\nu}(2\omega) \right|^2 \\ &= \frac{cn\epsilon_0}{2} \left[\underbrace{\sum_{\nu} |E_{\nu}(2\omega)|^2}_{\text{self-correlations}} + \underbrace{\sum_{\nu \neq \nu'} E_{\nu}(2\omega) E_{\nu'}^*(2\omega) e^{iq \cdot (r-r')}}_{\text{cross-correlations}} \right] \end{aligned} \quad (2.19)$$

The self-correlations are always present for non-centrosymmetric molecules and give rise to incoherent hyper-Rayleigh scattering (HRS) [146]. The cross-correlation term accounts for orientational correlations between different molecules. If the relative orientations of the molecules in the probed volume are not random, their relative phases will also not be random and the $e^{iq \cdot (r-r')}$ term will not average out to 0. The presence of orientational correlations will

therefore lead to additional emission of SH light. Moreover, due to the quadratic dependence of the detected SH intensity on the emitted E-field (i.e. the number density of molecules), the elastic SH response of a solution will be dominated by the most abundant species in the sample which are the solvent molecules (water). Therefore, small amounts of solutes that alter the orientational order of many water molecules can lead to a large change in the SH response [40, 41, 149].

2.1.5. Elastic second-harmonic scattering from charged particles

A charged particle dispersed in a polar liquid, such as water, will perturb the orientational order of water molecules at the particle-water interface as well as to a lesser extent further from the particle via a charge-dipole interaction [115, 127, 143, 164]. To analyze the elastic second-harmonic response of such systems, we can adapt Eqs. (2.14) derived previously for SFS. For a non-resonant second-harmonic scattering process with collinear excitation, the equations are greatly simplified. Firstly, due to the degeneracy of the exciting fields ($E_1(\omega_1) = E_2(\omega_2) \equiv E(\omega)$), the indices j, k of $\chi_{s,ijk}^{(2)}$ are permutable. The $\chi_s^{(2)}$ tensor is thus reduced from 7 to 4 elements: $\chi_{s,1}^{(2)}, \chi_{s,2}^{(2)} = \chi_{s,3}^{(2)}, \chi_{s,4}^{(2)}, \chi_{s,6}^{(2)} = -\chi_{s,7}^{(2)}$. Secondly, in collinear excitation: $\alpha = \beta = 0$. Lastly, instead of 8 orthogonal polarization combinations, there are now only 4: ppp, pss, spp, sss. Taking this into consideration, we obtain from Eqs. (2.14) the following expressions for the intensities of the emitted E-fields:

$$\begin{aligned} E_{ppp}^{(2)} &= \alpha \left[\cos\left(\frac{\theta}{2}\right)^3 \Gamma_1^{(2)} + 2 \cos(\theta) \cos\left(\frac{\theta}{2}\right) \Gamma_2^{(2)} \right] + E_{pss}^{(2)} \\ E_{pss}^{(2)} &= \alpha \cos\left(\frac{\theta}{2}\right) \Gamma_4^{(2)} \\ E_{spp}^{(2)} &= -\frac{\alpha}{2} F_{ch,1} \chi_6 \sin(\theta) \\ E_{sss}^{(2)} &= 0 \end{aligned} \tag{2.20}$$

The polarization of the solvent by the surface charge gives rise to an additional 3rd-order contribution to the emitted SH light, as illustrated in Figure 2.6A. The additional contribution can be included in the equation of SH generation via an effective third-order susceptibility tensor $\chi^{(3)'}$ in the following manner:

$$\mathbf{P}^{(2)}(2\omega) = \varepsilon_0 \left(\chi^{(2)} : \mathbf{E}(\omega) \mathbf{E}(\omega) + \chi^{(3)'} : \mathbf{E}(\omega) \mathbf{E}(\omega) \mathbf{E}_{DC}(0) \right) \tag{2.21}$$

where E_{DC} is the electrostatic field generated by the particle. Its direction is normal to the interface and its magnitude is related to the surface potential Φ_0 via the relation $E_{DC}(r') = -\frac{d\Phi_0(r')}{dr'}$. The $\chi^{(3)'}_{ijk}$ tensor includes water reorientation (a $\beta^{(2)}$ effect on the molecular level) and a true third-order effect ($\beta^{(3)}$) but since both effects are linearly dependent on all 3 input electric fields they are grouped under a common effective susceptibility $\chi^{(3)'}_{ijk}$ [164].

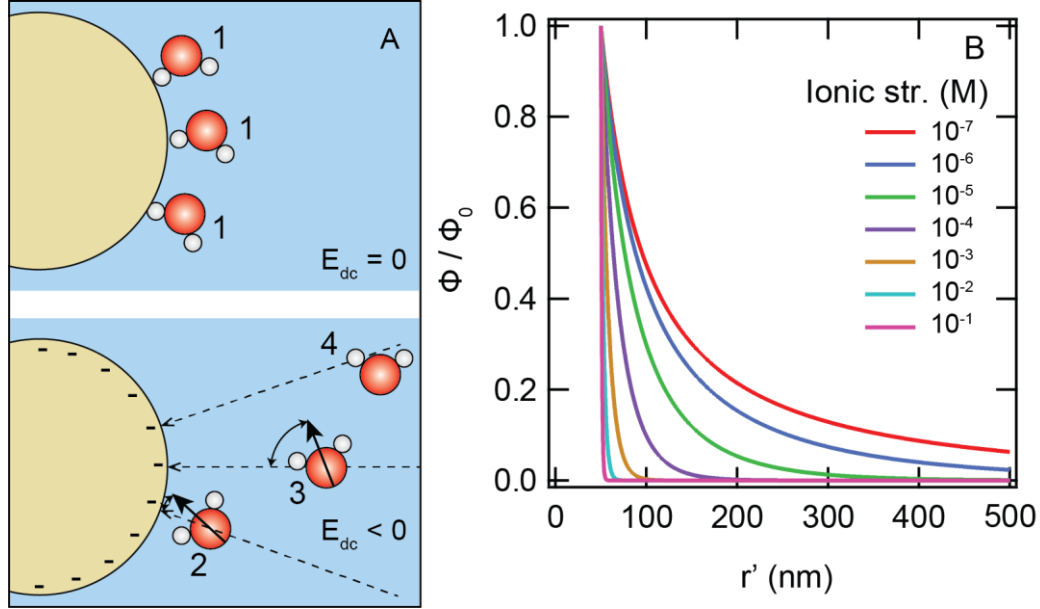


Figure 2.6: The sources of SH scattering from charged particles in water. (A) Possible sources of SH: 1: water oriented by an interface (e.g. H-bonding), 2: water reoriented at the interface by an electrostatic field, 3: water reoriented by an electrostatic field in the bulk, 4: a water molecule whose orientation is not affected by the electrostatic field but still can generate SH through a pure third-order effect ($\beta^{(3)}$). (B) The decay of the electrostatic potential as a function of distance from the surface of an $R = 50$ nm particle at different ionic strengths. The higher the ionic strength the faster the decay.

The additional SH emission due to $\chi^{(3)'}_{ijk}$ can be calculated by a similar approach as was used for $\chi^{(2)}$. Since the E_{DC} always points in the normal direction, regardless of the electromagnetic fields, the fourth-rank $\chi^{(3)'}_{ijkl}$ tensor can be simplified to a third-rank tensor with the same symmetry properties as the $\chi^{(2)}$ tensor, i.e. we can exclude the last index: $\chi^{(3)'}_{ijkl} = \chi^{(3)'}_{ijk}$. The calculation of $\Gamma^{(3)}$ differs from that of $\Gamma^{(2)}$ in that the integration in Eq. (2.11) must now be performed in the radial direction as well. Here, the SH light is generated from successive shells of water molecules ordered by E_{DC} which leads to an interference effect [137]. To account for this, we must include the spatial variation of $E_{DC}(r')$ in the integral which gives us the equation:

$$\Gamma_{a_0 a_1 a_2}^{(3)'} = \sum_{c_0 c_1 c_2} \int d\mathbf{r}'^3 \left\{ \chi_{c_0 c_1 c_2, r'}^{(3)'} E_{DC}(r') e^{-i\mathbf{q} \cdot \mathbf{r}'} \prod_{i=0}^2 (\mathbf{e}_{c_i} \cdot \mathbf{q}_{a_i}) \right\} \quad (2.22)$$

The integration of Eq. (2.22) over θ' and ϕ' is identical to the procedure for $\chi^{(2)}$ (Eq. (2.11)). Due to additional symmetries, we have $\chi_1^{(3)'} = \chi_5^{(3)'} = \chi_6^{(3)'} = \chi_7^{(3)'} = 0$, $\Gamma_1^{(3)} = 0$. The $\chi \rightarrow \Gamma$ transformation is now a simpler relationship: $\Gamma_n^{(3)} = 2F_1 \chi_n^{(3)'}$ for $n = 2, 3, 4$. To integrate Eq. (2.22) over r' we can express the electrostatic field in the form $E_{DC}(r') = -\frac{d\Phi(r')}{dr'}$ where the potential $\Phi(r')$ is:

$$\Phi(r') = \Phi_0 \frac{R}{r'} e^{-\kappa(r'-R)} \quad (2.23)$$

where $\Phi(R) = \Phi_0$ is the surface potential and κ is the inverse Debye length [165]. The decay of the potential from the surface of a charged particle in an electrolyte is shown in Figure 2.6B. Eq. (2.22) now reads [137]:

$$\begin{aligned} \Gamma_n^{(3)'} &= - \int_R^{+\infty} \frac{d\Phi(r')}{dr'} \Gamma_n^{(3)} dr' = 2\chi_n^{(3)'} \left[F_1 \Phi_0 + \int_R^{+\infty} \frac{dF_1}{dr'} \Gamma_n^{(3)} \Phi(r') dr' \right] \\ &= 2\chi_n^{(3)'} \Phi_0 (F_1 + F_3) \end{aligned} \quad (2.24)$$

with the form-factor $F_3 = 2\pi i R^2 \frac{qR \cos(qR) + \kappa R \sin(qR)}{(qR)^2 + (\kappa R)^2}$. The total emitted electric field due to 2nd and 3rd order contributions is obtained by simply transforming Eqs. (2.14) in the following manner: $\Gamma_n^{(2)} \rightarrow \Gamma_n^{(2)} + \Gamma_n^{(3)'}$ for $n = 2, 3, 4$ [137].

2.1.6. SH scattering from cylindrical particles

The theory of SH scattering from cylindrical particles was developed by J.I. Dadap [166]. For simplicity, we will assume that the cylinder is made of noncentrosymmetric material whose crystallographic coordinates are aligned with the coordinates of the particle. The approach to deriving the scattered SH light differs from that for spheres shown above. The polarization of a cylinder can be calculated as:

$$\mathbf{p}' = \frac{1}{V} \int_V \chi^{(2)}(\mathbf{r}') \exp(i\mathbf{q} \cdot \mathbf{r}') d\mathbf{r}' \quad (2.25)$$

where V is the volume of the cylinder. The scattering wavevector and its magnitude are defined the same way as before: $\mathbf{q} = \mathbf{k}_0 - 2\mathbf{k}_1$ and $q = k_0 \sin(\theta/2)$. The geometry of the scattering process is shown in Figure 2.7A. The lab frame is represented by a Cartesian coordinate system $(\hat{x}, \hat{y}, \hat{z})$ while the particle is represented by a rotated coordinate system $(\hat{x}', \hat{y}', \hat{z}')$. The cylinder can be arbitrarily rotated relative to the lab frame via the Euler matrix [167]:

$$\mathbf{M}(\alpha, \beta, 0) = \mathbf{R}_x(\beta)\mathbf{R}_z(\alpha) \quad (2.26)$$

where $\mathbf{R}_i(j)$ is a matrix representing the rotation by an angle j around an axis i . We can use the axial symmetry axis of the cylinder to define a cylindrical coordinate system with unit vectors $(\hat{\rho}', \hat{\phi}', \hat{z}')$ (shown in Figure 2.7B) which are related to the cylinder's Cartesian coordinates $(\hat{x}', \hat{y}', \hat{z}')$ via the transformations:

$$\begin{aligned} \hat{\rho}' &= \cos(\varphi') \hat{x}' + \sin(\varphi') \hat{y}' \\ \hat{\phi}' &= -\sin(\varphi') \hat{x}' + \cos(\varphi') \hat{y}' \\ \hat{z}' &= \hat{z}' \end{aligned} \quad (2.27)$$

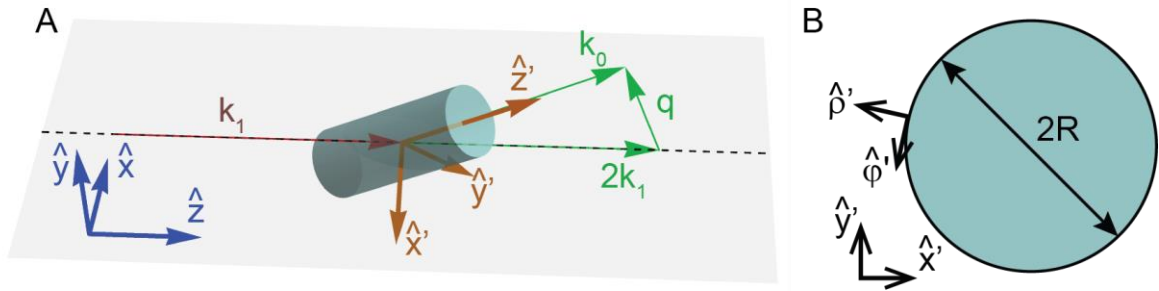


Figure 2.7: Geometry of SHS from a cylindrical particle. (A) A perspective view of the scattering geometry. The laboratory Cartesian coordinates $(\hat{x}, \hat{y}, \hat{z})$ are shown in blue, the particle's Cartesian coordinate $(\hat{x}', \hat{y}', \hat{z}')$ are shown in orange and are related to the laboratory coordinates via an arbitrary rotation using the Euler angles α, β . The scattering plane is defined by the vectors \hat{x} and \hat{z} . The wavevector of the incident light \mathbf{k}_1 is in the \hat{z} direction. (B) Top view of the cylinder. The orthogonal unit vectors $\hat{\rho}'$ lies in the radial direction, the unit vector $\hat{\phi}'$ is normal to the surface and is orthogonal to $\hat{\rho}'$ and \hat{z}' .

The source vector \mathbf{r}' can be expressed in the Cartesian or cylindrical coordinates of the particle as:

$$\mathbf{r}' = x'\hat{x}' + y'\hat{y}' + z'\hat{z}' = \rho'\hat{\rho}' + z'\hat{z}' \quad (2.28)$$

The electric field in the lab and the particle frames is:

$$\hat{\mathbf{e}}_0 = \epsilon_{01}\hat{\mathbf{x}} + \epsilon_{02}\hat{\mathbf{y}} = \epsilon_1\hat{\mathbf{x}}' + \epsilon_2\hat{\mathbf{y}}' + \epsilon_3\hat{\mathbf{z}}' = \epsilon_\rho\hat{\boldsymbol{\rho}}' + \epsilon_\varphi\hat{\boldsymbol{\phi}}' + \epsilon_3\hat{\mathbf{z}}' \quad (2.29)$$

The E-field components in the lab frame $(\epsilon_{01}, \epsilon_{02}, 0)$ and those in the particle frame $(\epsilon_1, \epsilon_2, \epsilon_3)$ are related by an Euler rotation: $\epsilon_i = M_{ij}\epsilon_{0j}$. According to Eq. (2.27) the relationship between the E-field components in the particle's Cartesian and cylindrical coordinates is:

$$\begin{aligned} \epsilon_\rho &= \epsilon_1 \cos(\varphi') + \epsilon_2 \sin(\varphi') \\ \epsilon_\varphi &= \epsilon_2 \cos(\varphi') - \epsilon_1 \sin(\varphi') \end{aligned} \quad (2.30)$$

The wavevector can be expressed in the lab and particle frame as:

$$\mathbf{q} = q_1\hat{\mathbf{x}} + q_2\hat{\mathbf{y}} + q_3\hat{\mathbf{z}} = Q_1\hat{\mathbf{x}}' + Q_2\hat{\mathbf{y}}' + Q_3\hat{\mathbf{z}}' \quad (2.31)$$

where $(q_1, q_2, q_3) = -k_1(\sin(\theta), 0, \cos(\theta) - 1)$ and $Q_i = M'_{ij}q_j$.

For a cylinder made of a noncentrosymmetric medium, the SH signal is dominated by the bulk response $\chi_0^{(2)} = \chi^{(2)} : \hat{\mathbf{e}}_0 \hat{\mathbf{e}}_0$ which is independent of \mathbf{r}' and can be taken out of the integral in Eq. (2.25). The remaining terms in the integral give us the form factor f . To evaluate it, we need to express the term $\mathbf{q} \cdot \mathbf{r}'$ using Eqs. (2.28) and (2.31):

$$\mathbf{q} \cdot \mathbf{r}' = Q_1\rho' \cos(\varphi') + Q_2\rho' \sin(\varphi') + Q_3z' \quad (2.32)$$

The form factor f is then:

$$\begin{aligned} f &= \frac{1}{V} \int_{-L/2}^{L/2} \int_0^{2\pi} \int_0^R \exp[i(Q_1\rho' \cos(\varphi') + Q_2\rho' \sin(\varphi') + Q_3z')] \rho' d\rho' d\varphi' dz' \\ &= \frac{J_1(QR)}{QR} \frac{\sin(LQ_3/2)}{LQ_3/2} \end{aligned} \quad (2.33)$$

Where J_1 is the Bessel function of the first kind and first order, $Q = \sqrt{Q_1^2 + Q_2^2}$, R is the radius of the cylinder, and L is its height. The polarization of the cylinder in its reference frame is:

$$\mathbf{p}' = f\chi_0^{(2)} \quad (2.34)$$

To calculate the detected E-field, we need to express \mathbf{p}' in the lab frame as \mathbf{p} via an inverse rotation: $\mathbf{p} = \mathbf{M}^T \mathbf{p}'$. The amplitude of the E-field at the detector is then proportional to:

$$E(2\omega) \propto \mathbf{p} \cdot \hat{\mathbf{u}} \quad (2.35)$$

where $\hat{\mathbf{u}}$ is a unit polarization vector of the scattered light defined in Eq. (2.10).

2.1.7. SHS from randomly oriented particles

The scattered SH light from randomly oriented particles can be obtained by averaging the emitted intensity over the Euler angles defining the orientation of the particle in space [166, 168]. The Euler angles α, β, γ are shown in Figure 2.8. The Euler rotation matrix $\mathbf{M}(\alpha, \beta, \gamma)$ is a product of 3 elementary rotation matrices. In the z-x-z convention, the Euler matrix is:

$$\mathbf{M}(\alpha, \beta, \gamma) = \begin{pmatrix} c_\alpha s_\gamma - s_\alpha c_\beta s_\gamma & -s_\alpha c_\beta c_\gamma - c_\alpha s_\gamma & s_\alpha s_\beta \\ s_\alpha s_\gamma + c_\alpha c_\beta s_\gamma & c_\alpha c_\beta c_\gamma - s_\alpha s_\gamma & -c_\alpha s_\beta \\ s_\beta s_\gamma & s_\beta c_\gamma & c_\beta \end{pmatrix} \quad (2.36)$$

where $c_i = \cos(i)$ and $s_i = \sin(i)$.

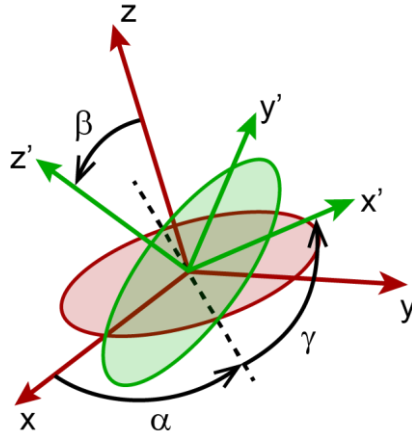


Figure 2.8: Rotation via the proper Euler angles (z-x-z convention). The original xyz coordinates are transformed by 3 rotations to coordinates XYZ. The first rotation is about the z-axis by the angle α . The second rotation is around the intermediate axis (dashed) by the angle β . The third rotation is about the new z'-axis by the angle γ .

To perform orientational averaging of the SHS intensity $I(\alpha, \beta, \gamma)$ that depends on the Euler angles (α, β, γ) we need to evaluate the integral:

$$\langle I \rangle_{\alpha, \beta, \gamma} = \frac{1}{N} \int_0^{2\pi} \int_0^{\pi} \int_0^{2\pi} I(\alpha, \beta, \gamma) \sin(\beta) d\gamma d\beta d\alpha \quad (2.37)$$

where $N = \int_0^{2\pi} \int_0^{\pi} \int_0^{2\pi} \sin(\beta) d\gamma d\beta d\alpha$ is a normalization constant. For cylinders, the angle γ can be omitted thanks to the cylinder's axial symmetry [166].

2.2. Experimental apparatus for sum-frequency scattering

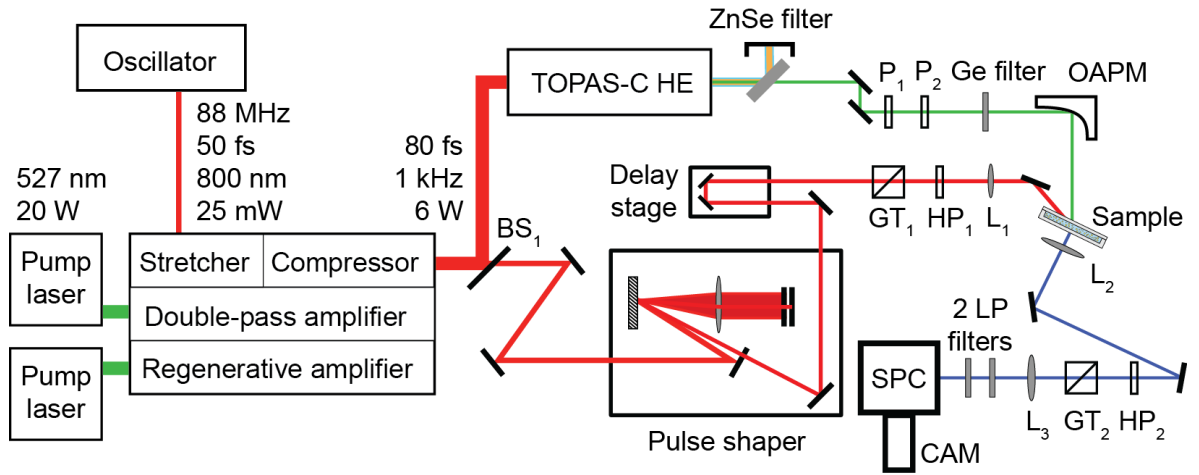


Figure 2.9: Schema of the optical apparatus for vibrational sum-frequency scattering. BS = beam splitter (non-polarizing), GT = Glan-Taylor polarizing beamsplitter, P = wire grid polarizer, OAPM = off-axis parabolic mirror, L = lens, LP filter = low-pass filter, HP = half-wave plate, SPC = spectrometer, CAM = camera.

The experimental apparatus for vibrational sum-frequency scattering is illustrated in Figure 2.9. The setup has been described in detail in the published literature [104, 130]. The primary source of optical pulses is a Ti:Sapphire oscillator (Femtolasers Integral 50) seeding 50 fs long pulses with a central wavelength of approx. 800 nm at a repetition rate of 88 MHz with an average power of 250 mW into an amplifier (SpectraPhysics SpitFire Pro). The amplifier is pumped by the second-harmonic (527 nm) of two Nd:YLF pulsed lasers. The oscillator output is first amplified in a regenerative amplifier up to a power of approx. 2.4 W. The second amplification up to 5-6 W is done in a double-pass amplifier. The amplified pulse is then compressed in time to 80 fs (autocorrelation curve shown in Figure 2.10A). The beam profiles of the SpitFire output are shown in Figure 2.10B. The central wavelength at the output is ~806.7 nm with an FWHM of ~12.5 nm (spectrum shown in Figure 2.10C). The repetition rate of the amplified pulses is 1 kHz.

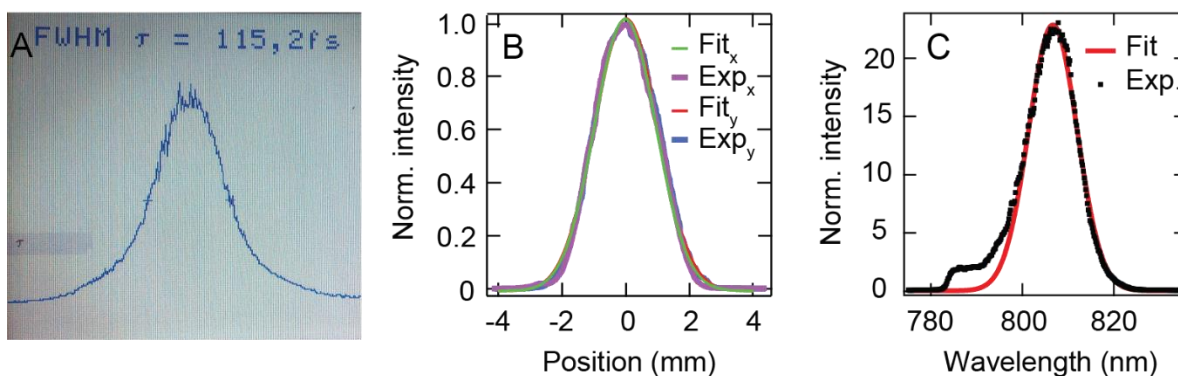


Figure 2.10: The characteristics of the SpitFire Pro laser output. (A) Pulse duration measured by an autocorrelator (the actual pulse duration for a Gaussian temporal profile is the value shown divided by $\sqrt{2}$, i.e. $\sim 81 \text{ fs}$). (B) X- and Y- beam profiles of the SpitFire beam (the actual beam was compressed by a factor of 3 to fit in the beam profiler detector). The measured values (Exp) were fitted by a Gaussian function (Fit). (C) A spectrum of the SpitFire output. The measured values were fitted by a Gaussian function excluding the low-wavelength shoulder.

The output of the amplifier is split into two beams with a non-polarizing beam-splitter. Most of the beam's power is used to pump a commercial 3-stage optical parametric amplifier with a difference frequency generator (Light Conversion TOPAS-C HE). The parametric amplifier produces 50 fs pulses tunable between 900 and 10000 cm^{-1} with a bandwidth (FWHM) of $120\text{-}170 \text{ cm}^{-1}$. An optional ZnSe filter is placed at the output of the TOPAS to block the transmitted signal and idler beams. Otherwise, the signal and idler beams are blocked physically later in the beam path since they are non-collinear with the IR beam. The beam is then passed through a pair of BaF₂ wire grid polarizers (Thorlabs WPH25H-B) to control the power and polarization direction. Afterward, the beam is passed through a Ge filter to remove remaining undesired frequencies which are collinear with the IR beam. Finally, the IR beam is focused into the sample by a gold off-axis parabolic mirror ($f = 50$ or 100 mm). The focus size at the sample position is $\sim 70 \mu\text{m}$.

The visible beam is passed through a home-built pulse shaper which consists of a grating that spatially disperses the spectrum, a lens that collimates the dispersed beam, an adjustable slit that cuts the spectrum and a mirror that reflects the beam back onto the grating. At the output of the pulse shaper, the spectral FWHM is $< 15 \text{ cm}^{-1}$ and the pulse duration is 1-2 ps (spectrum is shown in Figure 2.11A). The output of the pulse shaper is tilted up and fed into a delay line. After the delay line, the pulse passes through a fixed Glan-Taylor polarizing beam-splitter (CVI, PBS-800-050), ensuring a linear horizontally-polarized output. The beam is then passed through a zero-order half-wave plate (Eksma 460-4215) to control the polarization direction. A lens ($f = 300 \text{ mm}$) then focuses the light slightly after the sample (focus size $\sim 150 \mu\text{m}$). The advantage of a shallow focus is the ease of overlapping of the visible beam

with the tightly focused IR beam and the enhanced stability of the beam overlap with against mechanical perturbations and beam drift. The sample cell consists of a CaF_2 window facing the incident beams and a quartz suprasil cuvette (106-QS, PL 0.2 mm, Hellma AG) with an optical path of 200 μm and a volume of approx. 45 μL .

The detection path consists of a collecting plano-convex lens ($f = 15$ mm, Thorlabs LA1540-B) that is oriented perpendicular to the surface of the cuvette. The collimated light is then reflected by 2 Ag-coated flat mirrors. The polarization of the scattered light is controlled via an achromatic zero-order half-wave plate (Thorlabs AHWP05M-600) and Glan-Taylor polarizer (Thorlabs GT15-B), where the polarizer is fixed to allow only p-polarized light through and the half-wave plate placed before the polarizer is used to select the linear polarization of the scattered light that will pass through the polarizer to the detector. This ensures that the polarization-sensitive grating is always illuminated by p-polarized light which diffracts with higher efficiency in a broader range of wavelengths [169]. The scattered 800 nm light is then blocked with two low-pass filters (3rd Millenium, 3RD770SP) and the remaining SF light is focused using a plano-convex lens ($f = 5$ cm) into a spectrometer (Acton SpectraPro 2300i). The light is dispersed in the spectrometer and the spectrum is recorded using an intensified CCD camera (Princeton Instruments PiMax3) with a gate width of 10 ns.

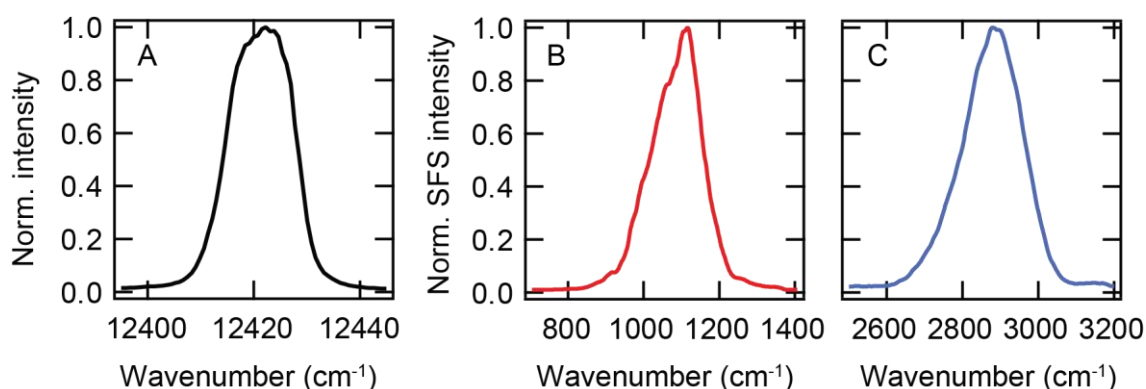


Figure 2.11: Spectra of the pulses used for SFS. (A) A spectrum of the visible beam after the pulse shaper. (B) A spectrum of the IR beam in the region 1000-1200 cm^{-1} obtained by non-resonant SFS from KNbO_3 nanocrystals. (C) A spectrum of the IR beam in the region 2800-3000 cm^{-1} obtained in the same manner.

For normalization purposes, a spectrum of the IR beam (I_{IR}) is recorded using non-resonant SFS from a sample of KNbO_3 nanocrystals deposited on a quartz cuvette. IR spectra of in the two spectral regions used in this thesis (1000-1200 cm^{-1} and 2800-3000 cm^{-1}) are shown in Figure 2.11B,C. Background spectra ($I_{background}$) are recorded by offsetting the incident pulses in time or by blocking one of the incident beams. The formula used for the normalization of the SFS spectra is:

$$Norm.SFS\ intensity = \frac{I_{sample} - I_{background}}{I_{IR}E_{vis}E_{IR}\tau_{acq}} \quad (2.38)$$

where E_{vis} / E_{IR} are the pulse energies of the visible/IR beam in μJ and τ_{acq} is the total acquisition time in seconds (integration time in seconds times the number of expositions). The typical pulse energies used were 8-10 μJ for the visible pulse and 2-8 μJ for the IR, with acquisition times varying between 1 to 5 minutes depending on the strength of the SFS signal but with integration times never exceeding 60 s (60 000 pulses).

To deconvolve the measured SFS spectra into individual vibrational modes, the spectra can be fitted with multiple Lorentzian resonances on top of a non-resonant background. The n^{th} resonance is described by an amplitude A_n , a resonance frequency ω_{0n} , a peak width γ_n , and a phase φ_n . The nonresonant background is described by an amplitude A_{NR} and a phase φ_{NR} . The complete fitting function is as follows [73, 170, 171]:

$$I_{SFS}(\theta, \omega) = \left| A_{NR}f(\theta, \omega)e^{-i\varphi_{NR}} + \sum_n \frac{A_n(\theta)\gamma_n e^{-i\varphi_n}}{\omega - \omega_{0n} + i\gamma_n} \right|^2 \quad (2.39)$$

2.3. Experimental apparatus for second-harmonic scattering

The schema of the apparatus used for SHS experiments is shown in Figure 2.12. The setup was described in detail in the literature [172]. The source of light is a Yb:KGW laser (Light Conversion Pharos) with a pulse duration of 190 fs (shown in Figure 2.13A), a central wavelength of 1028 nm, a bandwidth (FWHM) of 8.6 nm (spectrum in Figure 2.13B), and a repetition rate of 200 kHz. The time-bandwidth product of the laser (2.928) is within 5.3% of the theoretical limit for a Gaussian beam (2.773). The output of the laser is passed through a polarizing Glan-Taylor beam-splitter to ensure the linear polarization of the outgoing light. The polarization of the beam going into the sample is then controlled via a zero-order half-wave plate (Thorlabs WPH05M-1030). A high-pass filter with a cutoff at 750 nm (Thorlabs FEL0750) is placed before the focusing lens to eliminate second-harmonic light generated in the preceding optics. The light is focused into the sample by a plano-convex lens ($f = 75\text{ mm}$) with a focal beam waist of 32 μm and a Rayleigh length of 3.2 mm. The sample consists of a cylindrical glass cuvette (inner diameter 4.2 mm, LS instruments) placed in a temperature-controlled holder.

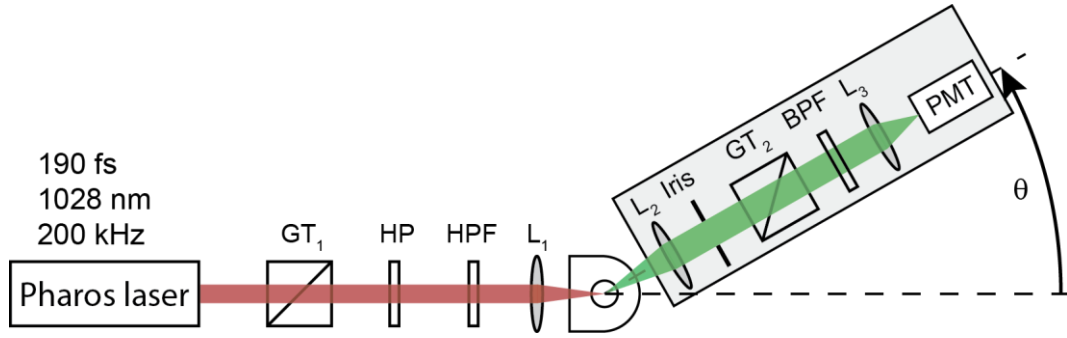


Figure 2.12: The experimental setup for second-harmonic scattering. GT = Glan-Taylor polarizing beam-splitter, HP = half-wave plate, HPF = high-pass filter, L = lens, BPF = band-pass filter, PMT = photomultiplier tube.

The scattered SH light at 514 nm (spectrum shown in Figure 2.13B) is collected via a series of optics mounted on a computer-controlled arm that can rotate in the horizontal plane around the sample. The detection arm consists of a collimating plano-convex lens ($f = 50$ mm), an iris for controlling the acceptance angle, a Glan-Taylor polarizing beam-splitter for controlling polarization of the detected light (Thorlabs GT10-A), a band-pass filter for 515 ± 5 nm (or ± 25 nm) (Chroma ET515/10x or ET515/50), a focusing lens ($f = 30$ mm) and a diode detector with photomultiplier tube (Hamamatsu H7421-40). The maximum average power used for experiments (measured after L_1 without a sample) was 60 mW ($0.3 \mu\text{J}$ per pulse). It was previously confirmed that at this power no higher-order interactions contribute to the signal at 514 nm [41, 172].

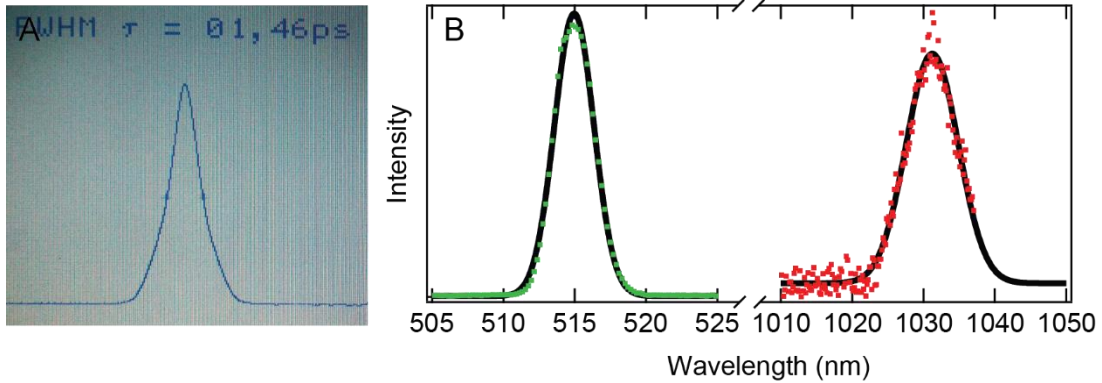


Figure 2.13: Characteristics of the laser used for SHS/fs-ESHS experiments. (A) Pulse duration (autocorrelation time) of the Pharos laser system used for SHS experiments. The actual pulse duration (FWHM) is obtained by dividing the autocorrelation time by $\sqrt{2}$. (B) Spectrum of the second-harmonic (generated in a BBO crystal) and the fundamental beam. The cutoff of the spectrometer (OceanOptics USB4000) is at ~ 1037 nm. The spectra were fitted with Gaussian functions.

The scattering patterns obtained in the polarization combination xyz were normalized according to the formula:

$$S(\theta) = \frac{I_{sample,xyz}(\theta) - I_{solvent,xyz}(\theta)}{I_{solvent,sss}(\theta)} \quad (2.40)$$

where $I(\theta)$ is the count rate (intensity) detected by the PMT at the angle θ obtained by averaging 20-50 expositions of 1s integration time each (2×10^5 pulses per exposition). In single-angle measurements, the normalized intensity in the xyz polarization combination was calculated as $I_{sample,xyz}/I_{solvent,xyz}$.

2.4. Dynamic light scattering

Dynamic light scattering (DLS) measures the distribution of the hydrodynamic sizes of particles based on their rate of diffusion through a liquid. The technique, also known as photon correlation spectroscopy, measures the temporal autocorrelations of light scattered from a particle dispersion [173]. In this work, we used the Malvern Nanosizer ZS (Malvern Ltd., UK). A basic schema of a DLS device is shown in Figure 2.14. The sample is illuminated with a He:Ne laser ($\lambda = 632.8$ nm) and the intensity of the scattered light as a function of time $I(t)$ is measured with a photodiode (PD) at an angle of 175° in a near-backscattering geometry.

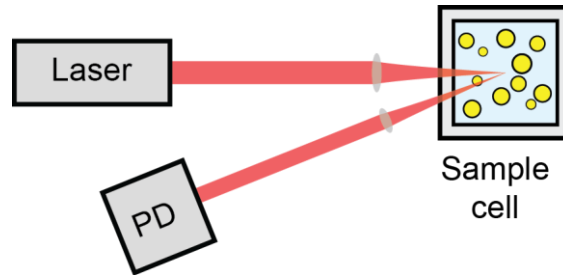


Figure 2.14: Schema of a DLS system.

The intensity autocorrelation function $G(\tau)$ is defined as:

$$G(\tau) = \int_{-\infty}^{+\infty} I(t)I(t + \tau)dt \quad (2.41)$$

where $I(t)$ is intensity detected at a time t and τ is a time delay. For Brownian particles $G(\tau)$ is related to the correlation function $g(\tau)$ via:

$$G(\tau) = A[1 + Bg(\tau)^2] \quad (2.42)$$

where A is the baseline of the function $G(\tau)$, and B is the intercept of the function $g(\tau)$. For a dispersion with a narrow size distribution, $g(\tau)$ decays exponentially as:

$$g(\tau) = e^{-Dq^2\tau} \quad (2.43)$$

where D is the translational diffusion coefficient and $q = (4\pi n/\lambda) \sin(\theta/2)$ is the scattering wavevector with the refractive index of the solution n , the wavelength λ , and the scattering angle θ . For the current system with water as the continuous phase ($n = 1.332$), $q = 2.64 \times 10^7 \text{ m}^{-1}$. For spherical particles, the diffusion coefficient is inversely proportional to the hydrodynamic radius R_H via the Stokes-Einstein relation [174]:

$$R_H = \frac{k_B T}{6\pi\eta D} \quad (2.44)$$

where η is the dynamic viscosity of the solvent. Two approaches can be used to fit the intensity decay with the correlation function in Eq. (2.42): the cumulant fit or the non-negative least squares method. The cumulant fit uses a single exponential function to fit the data and obtain a mean particle radius. The width of the size distribution is expressed as the polydispersity index $PDI = (\sigma/r)^2$, where σ is the standard deviation of the distribution. Lower values of the PDI mean a narrower size distribution. $PDI \approx 0.1$ can be considered a very narrow size distribution.

2.5. Electrophoretic mobility measurements

Surfaces of colloidal particles dispersed in water are often electrically charged. This attracts oppositely charged ions to surface which leads to the formation of an ionic atmosphere around the particles. Two regions of the atmosphere can be distinguished: an inner layer of mostly immobile ions and water and an outer, loosely-bound layer. The border between these two regions is the slip plane. The electrical potential between the slip plane and a distant point is called the zeta potential, ζ , or the electrokinetic potential [174]. The slip plane is at some distance from the actual particle surface as shown in Figure 2.15.

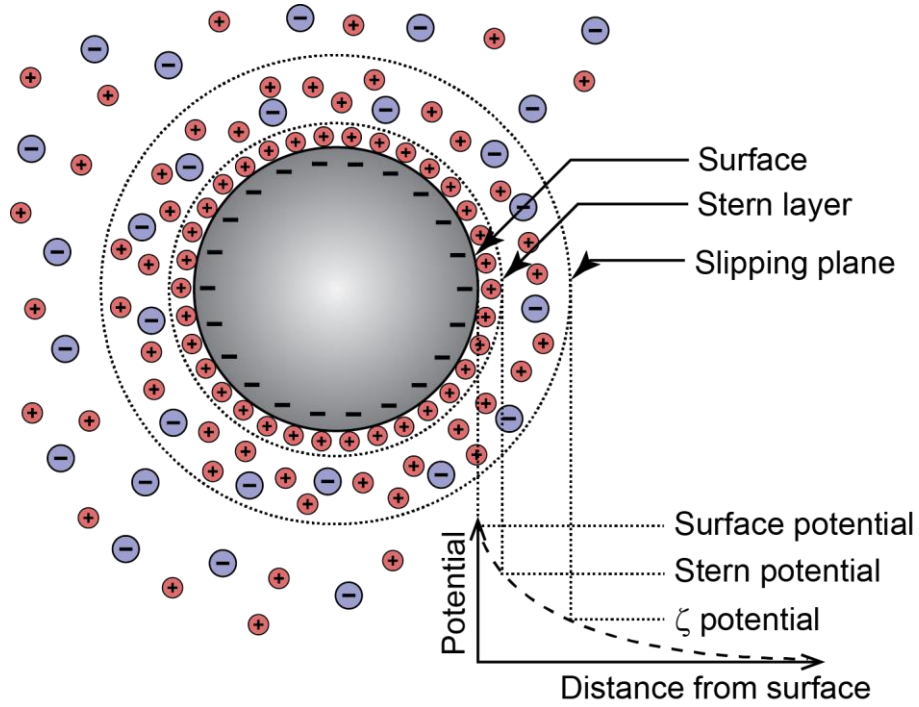


Figure 2.15: The distribution of ions around a negatively charged particle in an electrolyte solution. The case of a positively charged particle is the same except with all signs inverted. The zeta potential is measured at the slip plane which is at some distance from the surface.

The zeta potential can be determined from a measurement of the electrophoretic mobility of the particles. Here, the dispersion is placed between two electrodes. As alternating voltage is applied to the electrodes, the drift velocity of the charged particles toward the oppositely charged electrode is measured via dynamic light scattering. The drift velocity vector of a particle, \mathbf{v} , is directly proportional to the electric field intensity vector, \mathbf{E} , via the electrophoretic mobility μ_e [175]:

$$\mathbf{v} = \mu_e \mathbf{E} \quad (2.45)$$

There are several theories that derive electrophoretic mobility from the zeta potential. The Smoluchowski approximation is commonly used and states [176]:

$$\mu_e = \frac{\varepsilon_0 \varepsilon \zeta}{\eta} \quad (2.46)$$

where η is the dynamic viscosity of the solvent. The Smoluchowski approximation is valid for $\kappa^{-1} \ll R$, where κ^{-1} is the Debye length and R is the particle diameter.

Chapter 3: Hyaluronan orders water up to hundreds of nanometers and induces significant nuclear quantum effects

Hyaluronan (HA) is an anionic bio-polyelectrolyte found in the extracellular environment. It was recently proposed that the hydration of HA explains the low friction between joints during locomotion. Here, we explore the extended hydration shell structure of HA in light and heavy water using femtosecond-elastic second harmonic scattering (fs-ESHS). Recently, simple ions were shown to induce changes in the water-water interactions extending over a distance of tens of hydration shells. We find that HA enhances orientational water-water correlations much more than simple electrolytes, and over even longer distances. A strong isotope effect, stemming from nuclear quantum effects, is observed when light water (H_2O) is replaced by heavy water (D_2O), amounting to a factor of 4.3 in the scattered SH intensity. Angle-resolved fs-ESHS measurements in combination with nonlinear optical modeling show that HA behaves like a flexible chain surrounded by an extended spherical shell of orientationally correlated water. Using this model we describe several ways to determine the concentration-dependent size of a polyelectrolyte in water, using the amount of water oriented by the polyelectrolyte charges as a contrast mechanism. The spatial extent of the extended hydration shell, which includes water within as well as outside the chain is determined via temperature-dependent measurements and can reach up to 475 nm in H_2O and 260 nm in D_2O , corresponding to 1600 (928) hydration shells in H_2O (D_2O).

3.1. Introduction

Water has a key function in biology as it is the primary solvent of life. It actively participates in biochemical transformations such as protein folding, molecular recognition, self-assembly and joint lubrication [84, 177-179]. To elucidate the role that various constituents of the body play in sustaining life, it is important to take into account their interaction with the aqueous environment. One example where water plays a very important role is in the extracellular matrix of epithelial and connective tissues. The matrix is rich in hyaluronan (HA), an anionic polydisaccharide composed of D-N-acetylglucosamine and D-glucuronic acid (displayed in Figure 1A) [48]. HA is an excellent lubricant due to its ability to retain up to 10x its dry weight of water [180-185] and creates a gel-like pericellular coat [186, 187]. The hydration of HA is key for achieving low friction between moving joints [186, 188, 189]. Calorimetric [190, 191], vibrational spectroscopic [192-194] and compressibility [195] studies indicate slower hydrogen (H)-bond dynamics and different thermodynamic properties of the hydrating water compared to bulk water. However, the observed effects of HA are limited to the first of the second hydration shell. With recent developments in nonlinear optical spectroscopy allowing direct probing of the orientational order in the H-bond network of water over nanoscale distances [41], HA hydration warrants further investigation. This is especially relevant in light of the very recent discovery that long-range water-water interactions play a role in the viscosity of polyelectrolyte solutions [196].

The structure of water near ions and charged groups is perturbed relative to neat water due to well-known ion-dipole and H-bonding interactions [15, 197, 198]. However, the spatial extent over which ions perturb the structure of water is still a subject of debate [38]. Ions are traditionally assumed to have a short-range ordering effect, influencing the structure of, at most, the first three layers of hydrating water. This notion is supported by dielectric and THz spectroscopy [199, 200], X-ray [201] and neutron scattering [202], vibrational spectroscopies [9, 37, 203] and computational simulations [204, 205]. However, recent studies based on femtosecond-elastic second harmonic scattering (fs-ESHS) experiments [41, 152, 206], supported by computational studies [207-209] are changing this long-held notion that ion-water interactions are limited to several angstroms. Unlike most experimental techniques, which are often inherently limited to sub-nanometer length scales or equivalently require > 100 mM solute concentrations, fs-ESHS can directly probe spatial correlations over length scales comparable to the wavelength of the light used and in very dilute solutions [143]. Using fs-ESHS a non-specific long-range (~20 nm) influence of simple electrolyte ions on the hydrogen (H)-bond network of water molecules was discovered that starts at ionic strengths as low as 10 μ M [41]. This observation was explained as an electric field induced perturbation in the water-water orientational correlations. Moreover, there is a noticeable nuclear quantum effect that is yet to be explained.

Here, we explore the extended hydration shell structure of hyaluronan in light and heavy water using fs-ESHS. We observe that water-water orientational correlations are enhanced by HA more so than by ordinary salts. The increased order in water is measurable from an HA concentration below 0.1 $\mu\text{g/mL}$, equivalent to 0.25 μM of excess ionic strength. A significant isotope effect is observed when light water (H_2O) is replaced by heavy water (D_2O). The onset concentration increases in D_2O by a factor of 2.4 and the scattered intensity is 4.3 \times lower than in H_2O . Angle-resolved and temperature-dependent measurements were performed to elucidate the extended hydration shell structure further. In combination with nonlinear light scattering theory three different sizes are determined: The size of the folded polymer chain, the size of the shell with a non-negligible electrostatic field, and the extended hydration shell radius. The extended hydration shell spans up to 475 nm in H_2O and 260 nm in D_2O , corresponding to 1600 (928) hydration shells in H_2O (D_2O).

3.2. Experimental section

3.2.1. Materials

Hyaluronan (HA, sodium hyaluronate, structure shown in Figure 3.1A) produced by microbial fermentation of *Streptococcus pyogenes* was purchased from R&D Systems (mol. wt. 1350 kDa) and Contipro a.s. (mol. wt. 1145 kDa) and used as received. The salts NaCl (Sigma-Aldrich, >99.999%) and MgCl_2 (Chempura, >99.995%) were filtered through Millipore Millex-VV 0.1- μm polyvinylidene difluoride (PVDF) membrane filters. We used ultrapure water (> 18.2 $\text{M}\Omega\cdot\text{cm}$) dispensed from a Milli-Q UF-Plus instrument (Millipore Inc). Ultrapure heavy water (D_2O , 99.8 % D) was purchased from Armar Chemicals. Stock solutions of HA were prepared by reconstituting a weighted amount of HA powder in water. Individual samples were prepared by diluting a stock solution of HA in Eppendorf tubes. The tubes were cleaned by prior rinsing with water.

3.2.2. Angle-resolved second harmonic scattering

The experimental conditions used for fixed-angle measurements were similar to Refs. [40, 41, 149]. The detection angle was set to 90 ° with an acceptance angle of 11.4°. Each data point is an average of 3 - 5 measurements. Each measurement is an average of 50 exposures lasting 1 s each, i.e. using $50 \times 2 \times 10^5$ pulses in total. The gate width was 10 ns. The normalized fs-ESHS intensity at a 90° scattering angle was obtained by dividing the intensity of the solution by the intensity of the neat solvent using the same polarization combination.

We employ a three-letter code (xyz) to denote the polarization combination, where the first letter indicates the polarization direction of the outgoing (second-harmonic) light and the

following 2 letters denote the polarization of the incident light. The polarization direction can be either p-parallel or s-perpendicular with respect to the scattering plane.

Angle-resolved fs-ESHS measurements were performed by moving the detector arm in 5° steps between -90° and +90° with an opening angle of 3.4°. The intensity was normalized at each angle θ with respect to pure H₂O or D₂O. The normalized fs-ESHS intensity was calculated as: $S(\theta) = (I_{\text{solution}}(\theta) - I_{\text{water}}(\theta)) / I_{\text{HRS,water}}(\theta)$, where $I_{\text{HRS,water}}$ was obtained by measuring the scattering pattern of the solvent in sss polarization combination. The integrated fs-ESHS intensity was calculated using the formula: $S_{\text{int}} = \sum_{\theta \neq 0} S(\theta)$.

3.2.3. fs-ESHS from HA compared to simple electrolytes

To provide context, we recount a recent finding concerning fs-ESHS measurements performed on aqueous solutions of simple salts. Figure 1B shows the fs-ESHS intensity recorded at a scattering angle θ of 90° for NaCl in H₂O (red triangles) and D₂O (tilted blue squares). The data was adapted from Refs. [40, 41]. The increase in the fs-ESHS intensity was attributed to arise from an increase in the orientational order in the H-bond network of water, due to the interaction of the ionic electrostatic field with the H-bonded network. The intensity starts increasing from a salt concentration of 10 μ M, and saturates at ~10 mM. Electrolytes dissolved in D₂O show the same trend as in H₂O but with a 6 times higher onset concentration and a 36 % smaller saturation value, relative to the pure H₂O or D₂O solvent. This slight restructuring of the H-bond network also manifests itself on the macroscopic length scale as the Jones-Ray effect [210], an anomalous decrease of the surface tension at the fs-ESHS saturation concentrations. The increase in orientational order in the bulk solution gives rise to an entropic penalty, which reduces the surface tension [41, 210, 211].

Figure 1C shows fs-ESHS data obtained in the same manner for HA (mol. wt. 1145 kDa) dissolved in H₂O (red circles) and D₂O (blue squares) plotted as a function of calculated excess ionic strength and HA concentration. The total ionic strength in the solution I is given by $I = I_0 + I_{\text{excess}}$, where I_0 is the ionic strength of an infinitely dilute solution, and $I_{\text{excess}} = c_{\text{HA,mon.}}/2$ is the excess ionic strength with $c_{\text{HA,mon.}}$ the concentration of HA monomers. The fs-ESHS data was recorded in the same way as the data in Figure 1B, at a scattering angle θ of 90° and with all beams p-polarized, i.e. oscillating in the horizontal scattering plane. The fs-ESHS intensity of HA solutions at ionic strengths below 10 mM is much larger than that of simple electrolyte solutions, reaching ~6.3x the response of bulk water for H₂O and ~1.4x the response of bulk D₂O. The intensity increase also occurs at $I_{\text{excess}} = 10^{-8}$ M for HA in H₂O and at 10^{-6} M for HA in D₂O. The intensity plateau reached above 1 mM for H₂O and 10 mM for D₂O is the same for HA and NaCl in their respective solvents.

The increased magnitude of the fs-ESHS response indicates that the interaction of the electrostatic field from the ionic groups on the HA polymers with the H-bond network in water is much stronger than the same type of interaction in the electrolyte solution. This could be caused by the spatial arrangement of the ionic groups on the polymer: HA has a linear charge density of approximately -1 e/nm with the entire chain containing >3000 units. Unlike ions of simple salts, which are statistically distributed in solution, the charges on HA cannot move freely but are restricted, and spatially correlated over a certain distance due to covalent bonding between individual monomers on a single polymer chain. Additionally, intra-chain electrostatic repulsion further limits the flexibility and spatial positioning of the HA chains [212]. The concentration of such a large number of electric charges in a small region of space can generate much stronger localized electrostatic fields than statistically distributed free ions, leading to a much stronger fs-ESHS response of HA compared to NaCl. The characteristic length for electrostatic interactions in an electrolyte solution is given by the Debye length $\kappa^{-1} = \sqrt{\frac{\epsilon_0 \epsilon k_B T}{2 \times 10^3 N_A e^2 I}}$, which can be calculated from the ionic strength (I) in mol/L, with known temperature $T = 298 \text{ K}$, elementary electric charge e , Boltzmann constant k_B , Avogadro number N_A , vacuum permittivity ϵ_0 , and dielectric constant of water $\epsilon \approx 78.5$. The Debye length reaches the same order of magnitude as the wavelength (514 nm) above an ionic strength of $\sim 10^{-5} \text{ M}$ which coincides with the concentration region where we observe the strongest fs-ESHS response. This suggests that screened electrostatic interactions are at play here. However, the fact that replacing light with heavy water in HA solutions significantly alters the fs-ESHS response indicates that the HA does not simply order water molecules via a charge-dipole interaction because such interaction would not be affected by a change in the isotope of the water as both isotopes have nearly identical dielectric constants and dipole moments [27]. The isotope effect in the fs-ESHS response points to long-range interactions between the electric field of HA and the H-bond network of water (i.e. orientational water-water correlations) in the solution [40, 41]. As mentioned in Refs. [41, 196] it will take sophisticated nuclear quantum molecular dynamics [151] extended to include many-body effects, to describe these correlations in detail. Because such models do not yet exist, we revert to nonlinear light scattering theory [137, 164] to model the structure of HA polyelectrolyte hydration in H_2O . We will, therefore, describe angle-resolved and temperature-dependent second harmonic scattering data of HA in H_2O and extract relevant length scales that we will then compare with the contour length (the maximum end-to-end distance) and the electrostatic persistence length (the polymer rigidity due to intra-chain repulsion [212, 213]).

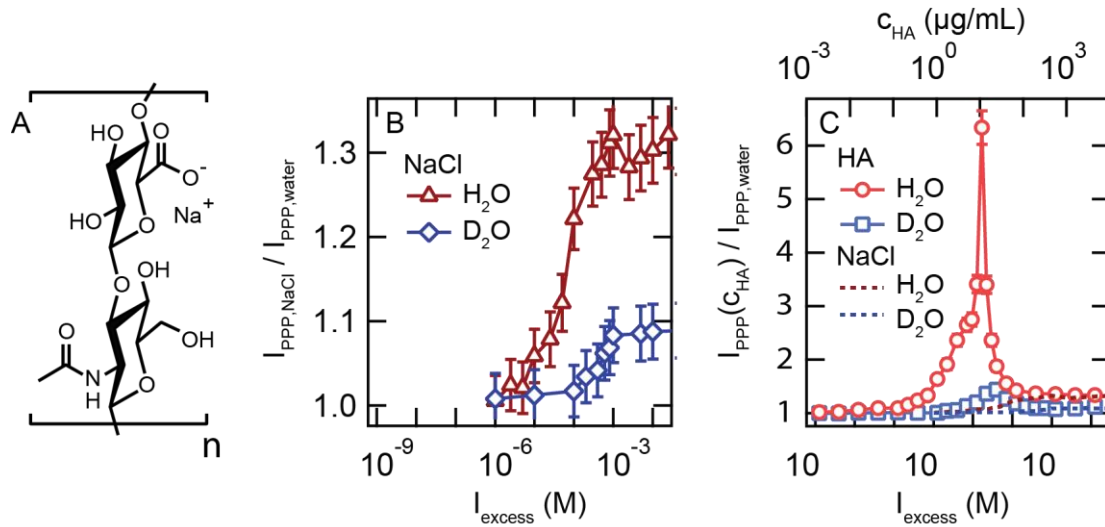


Figure 3.1: Hyaluronan enhances orientational correlations between water molecules. (A) Molecular structure of hyaluronan (HA). (B) Normalized fs-ESHS intensity as a function of ionic strength for NaCl dissolved in light (H₂O) and heavy (D₂O) water obtained with all beams polarized along the horizontal plane (ppp polarization combination). (C) Normalized fs-ESHS intensity as a function of excess ionic strength (and concentration of HA) for HA dissolved in light (H₂O) and heavy (D₂O) water obtained in ppp polarization combination. The dotted lines represent the data for NaCl in panel B. The relative intensity maximum $I_{PPP}(C_{HA})/I_{PPP,water} = 6.3$ at a $c_{HA} = 5$ μg/mL ($I_{excess} = 6.3$ μM) for H₂O and $I_{PPP}(C_{HA})/I_{PPP,water} = 1.45$ at a $c_{HA} = 32$ μg/mL ($I_{excess} = 40$ μM) for D₂O.

3.2.4. Angle-resolved second-harmonic scattering

To characterize the flexible structure of hydrated HA, we measured angle-resolved fs-ESHS in the entire forward half-plane for H₂O. In contrast to single-angle measurements, the angle-resolved measurements provide information about the shape of the emitted scattered light pattern, which is important for further analysis. Three representative angle-resolved scattering patterns of HA solutions at concentrations of 0.3, 3 and 10 μg/mL (excess ionic strength of 0.4, 3.8 and 12.5 μM), and one pattern of a NaCl solution (4.8 mM) are shown in Figure 3.2A. Patterns for all of the measured HA concentrations are shown in the appendix, Figure 3.5. The patterns were recorded with all beams polarized along the horizontal scattering plane (ppp polarization combination). The scattering pattern of NaCl solutions does not vary with salt concentration, as can be seen in Figure 3.5A in the appendix. In contrast, the shape and intensity of the HA patterns change significantly with increasing HA concentration (c_{HA}). The variations in the data of Figure 3.2A can be captured by two key parameters: The integrated fs-ESHS intensity S_{int} , calculated by integrating the scattering patterns in the forward half-plane, is shown in Figure 3.2B. The angle of maximum scattering intensity θ_{max} is shown in Figure 3.2C. S_{int} increases with HA concentration up to ~5 μg/mL (6.25 μM) and then drops

and levels off, very similar to the data measured at $\theta = 90^\circ$ (Figure 3.1C). θ_{max} shifts monotonously from 18° to 65° with increasing c_{HA} . To understand the unusual concentration dependence, we model the two essential properties of the scattering by using nonlinear light scattering theory. The solid lines in Figure 3.2B and Figure 3.2C correspond to the result of this model, which we describe next.

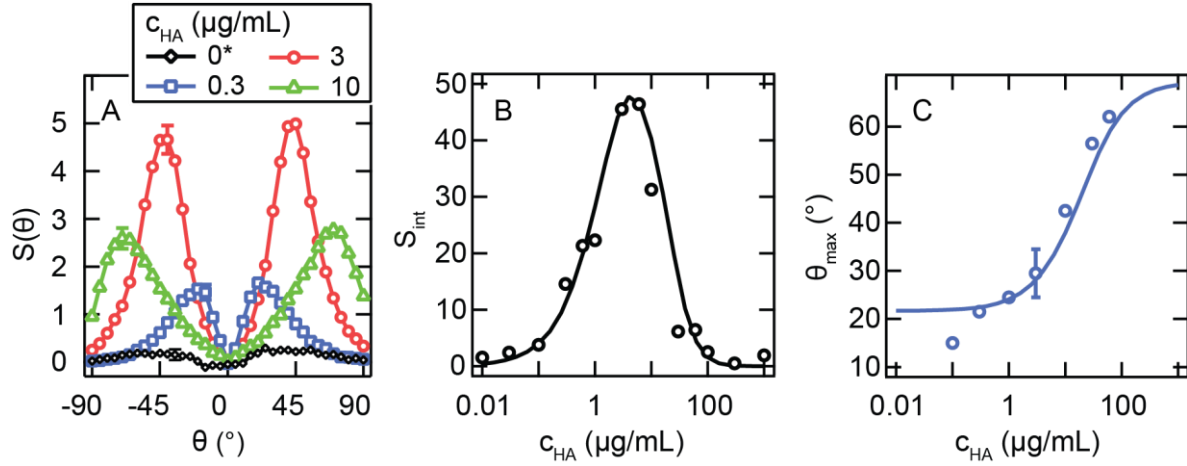


Figure 3.2: Scattering patterns of HA solutions are concentration-dependent. (A) Angle-resolved fs-ESHS measurement of HA solutions (1349 kDa) in H₂O measured at 3 concentrations showing strong concentration dependence of the angular distribution of the scattered SH light. More concentrated HA solutions scatter at higher angles. The value of 0* corresponds to a 4.8 mM NaCl solution. The excess ionic strength for the other concentrations is 0.4 μM (0.3 $\mu\text{g/mL}$), 3.8 μM (3 $\mu\text{g/mL}$), and 12.5 μM (10 $\mu\text{g/mL}$). More patterns are shown in the appendix (Figure 3.5A). (B) The integrated fs-ESHS intensity (S_{int}) in the forward half-plane as a function of HA concentration (c_{HA}). The solid curve shows the predicted behavior based on a proposed model of fs-ESHS and is calculated using Eq. (3.3)**Error! Reference source not found.** (C) The angle of maximum fs-ESHS intensity plotted as a function of HA concentration. The scattering angle at maximum intensity (θ_{max}) shifts to higher angles with increasing concentration which is equivalent to scattering from smaller objects. The solid line is calculated from the proposed model using Eq. (3.4) with $R = 5\kappa^{-1}$. All data was measured in the ppp polarization combination.

3.2.1. Modeling of the fs-ESHS results

To model the fs-ESHS response and to characterize the extent of the hydration shells around HA, we measured angle-resolved fs-ESHS in the entire forward half-plane. In contrast to single-angle measurements, the angle-resolved measurements provide information about the direction of the scattered light which is important for further analysis. Three representative angle-resolved scattering patterns of HA solutions at concentrations of 0.3, 3 and 10 $\mu\text{g/mL}$ (excess ionic strength of 0.4, 3.8 and 12.5 μM), and one pattern of a NaCl solution (4.8 mM)

are shown in Figure 3.2A. The scattering pattern of NaCl varies minimally with salt concentration (shown in Figure 3.5A). In contrast, the shape and intensity of the HA patterns change significantly with increasing HA concentration. To simplify the analysis of the data, we took two key parameters: the integrated fs-ESHS intensity S_{int} (calculated by integrating the scattering patterns in the forward half-plane) and the angle of maximum scattering θ_{max} . Patterns for all of the measured HA concentrations are shown in the appendix in Figure 3.5B. The patterns were recorded with all beams polarized in the horizontal scattering plane (ppp). The dependence of the integrated fs-ESHS intensity on HA concentration is shown in Figure 3.2B. We can see that the trend here is similar to the curve measured at the fixed scattering angle of 90 ° shown in Figure 3.1C. The intensity increases with HA concentration up to ~5 µg/mL and then drops rapidly and levels off. The maximum scattering angle as a function of HA concentration is plotted in Figure 3.2C. It can be seen that θ_{max} shifts monotonously from ~18 ° to 65 ° with increasing HA concentration. Both observations are indicative of a scattering object whose size decreases with concentration, leading to a larger θ_{max} . To better understand the unusual concentration dependence, we've attempted to capture the two essential properties of the scattering by applying the theory of second-harmonic scattering from charged particles. The solid lines in Figure 3.2B and Figure 3.2C correspond to the result predicted by this model (the details of the model are described below).

3.2.2. Modelling the SHS response

Nonlinear light scattering theory has been developed for a variety of systems, including SHS from spherical surfaces or infinitely thin shells around isotropic particles in an isotropic solution [156, 162, 166, 214]. The most useful approximation for the current situation is the Rayleigh-Gans-Debye (RGD) approximation, in which the refractive index contrast between a particle with radius R and the medium is small [160]. This response is characterized by a second-order surface susceptibility $\chi_s^{(2)}$, which captures interfacial chemical interactions. Later models have included the effect of a non-zero surface potential Φ_0 and ionic strength (via κ^{-1}) [115]. The electrostatic potential decays to ~2% of its surface value at R over a distance of $4\kappa^{-1}$ [137]. This introduces an effective third-order susceptibility $\chi^{(3)'}_{eff}$ response, which for the present non-resonant excitation has only a single value, $\chi^{(3)'} = 10.3 \times 10^{-22} \text{ m}^2/\text{V}^2$ [76]. Figure 3A shows an illustration of the relevant parameters in this model. Section S2 in the SI contains a more detailed description of RGD SHS from a sphere, which results in the following type of expression for the scattered SH response $S(\theta)$ in terms of the intensity scattered from a particle dispersion in ppp polarization $I(\theta)_{PPP,disp}$, normalized by the intensity scattered by pure water in the sss polarization combination $I(\theta)_{SSS,H2O}$:

$$S(\theta) = \frac{I(\theta)_{PPP,disp}}{I(\theta)_{SSS,H2O}} = N_p \left| F(q, R, \kappa, \chi_s^{(2)}, \chi^{(3)'}, \Phi_0) \right|^2 \quad (3.1)$$

For noninteracting particles, the single-particle response, determined by the form factor $F(q, R, \kappa, \chi_s^{(2)}, \chi^{(3)'}, \Phi_0)$ is multiplied by the particle density N_p . q is the magnitude scattering wave vector defined as the difference between the wave vectors of the scattered SH wave vector and the sum of the two fundamental wave vectors, $q = 4\pi n \sin(\theta/2)/\lambda$, with n the refractive index of the solvent and λ the SH wavelength. SHS scattering from isotropic particles with isotropic surfaces is characterized by four non-zero polarization combinations (sps, pss, ppp, pss), four vanishing polarization combinations (sss, spp, pps, psp), and the absence of scattered light in the forward direction ($\theta = 0^\circ$) for the four non-vanishing ones. This leads to a characteristic 2 lobe pattern similar to those of Figure 3.2A [126, 137, 156, 160]. The position of the lobes (represented by θ_{max}) shifts to higher angles with decreasing particle radius. For example, taking a wavelength of 1000nm, and $\chi_{s,2}^{(2)} = 1$, results in $\theta_{max} > 50^\circ$ for $R = 50$ nm, while $\theta_{max} < 20^\circ$ is reached when $R = 500$ nm.

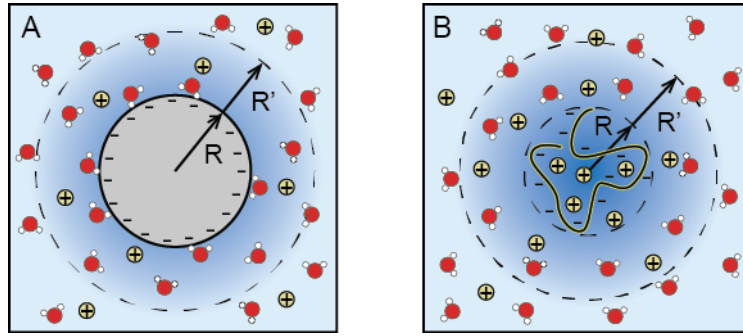


Figure 3.3: Illustration of the model. (A) A model of nonlinear light scattering from a sphere. The source of SHS signal are water molecules whose orientational distribution is distorted by their interaction with the surface of the particle as well as water molecules within the dashed circles that are perturbed by the electrostatic field of the particle. (B) Model for scattering from an HA solution. There is no surface but the electrostatic field of the polymer can distort the orientational distribution of water molecules, leading to SH generation.

Figure 3.2A and Figure 3.5B which shows ppp pattern for HA solutions, display the same striking features of SH scattering from a particle as described above, and so RGD nonlinear light scattering from a sphere can be taken as a starting point to describe the data in Figure 3.2B and Figure 3.2C and extract relevant length scales from it. We modify the model based on the differences between HA polymers in solution and a dilute dispersion of non-interacting spherical particles. Figure 3.2B shows an illustration of the changes and assumptions. First, HA polymers are either folded or stretched and do not have a different medium inside as is the case for particles or droplets. However, we can still consider the

boundary of a polymer as a closed shell with a certain radius R . R can, therefore, be considered as the average effective size of the folded negatively charged polyelectrolyte chain in the solution. Within this radius, there are charges and counter ions that together result in an electrostatic environment with a vanishing radial component of the electrostatic field. Outside this radius, there are counter ions that are more mobile and result in a slowly decaying electrostatic field, with the Debye length κ^{-1} a determining factor. Since SHS of a single object scales with R^6 , we consider that the aqueous volume outside of the soft sphere of the polymer chain with radius R will provide the dominant contribution to the SHS intensity. Since this boundary is charged there will be an electrostatic field that penetrates into the adjacent extended hydration shell, where it will increase the orientational order of the water (illustrated in). This decay length, taken from the center of the object and indicated by R' will have an approximate distance of $R' = R + 4\kappa^{-1}$ [137]. Furthermore, because HA has a charge spacing of ~ 1 nm, larger than the Bjerrum length in water (0.71 nm), counter-ion condensation will not occur when the HA concentration (c_{HA}) is varied [215]. This means that the surface potential Φ_0 can be considered as concentration-independent. For dilute solutions, the Debye length spans hundreds of hydration shells. With the $I \sim R^6$ scaling in mind, we expect that the long-range electrostatic field interaction will dominate over the short-range chemical interactions between water and the HA chain. This means we can neglect the $\chi_s^{(2)}$ contribution compared to the $\chi^{(3)'$ contribution in the model. Finally, to account for long-range charge-charge correlations between different HA chains due to the weakly-screened electrostatic field, we include a structure factor S_{DH} in the description of the scattering. Such a structure factor has been derived for electrolyte solutions [41], and is given by $S_{DH}(q, \kappa) = q^2 / (q^2 + \kappa^2)$. Taking these differences into account we arrive at the following expression for $S(\theta)$:

$$\begin{aligned}
 S(\theta) &= \frac{I(\theta)_{PPP,HA}}{I(\theta)_{SSS,H2O}} \\
 &= N_p \left[2 \Phi_0 (F_1(\theta, R) \right. \\
 &\quad \left. + F_3(\theta, R, \kappa)) \chi^{(3)'} \cos(\theta/2) (2 \cos(\theta) + 1) \right]^2 S_{DH}(q, \kappa)
 \end{aligned} \tag{3.2}$$

where $F_1 = 2\pi i R^2 \left(\frac{\sin(qR)}{(qR)^2} - \frac{\cos(qR)}{qR} \right)$ and $F_3 = 2\pi i R^2 \frac{qR \cos(qR) + \kappa R \sin(qR)}{(qR)^2 + (\kappa R)^2}$ are scattering form factor functions [76]. Eq. (2) contains the following parameters: Φ_0 , R , κ , and $\chi^{(3)'}$. Of these, κ , and $\chi^{(3)'}$ are known and Φ_0 is independent of the HA concentration. The last parameter in the model is the effective size or radius R . For a flexible charged polymer like HA this value is unknown but must fall somewhere between the size of a completely collapsed chain and a fully extended one [216]. Given that the intra-chain electrostatic repulsion is the major contribution

to the extension of the HA chain, we express the size of HA as a linear function of the Debye length, i.e. $R = \alpha \kappa^{-1}$, where we will treat the proportionality constant α as a fitting parameter to obtain the size of the hydration shell of HA. Such a choice is in accordance with other size models, such as the Odijk-Skolnick-Fixman (OSF) theory [212, 213], although the exponent on κ^{-1} varies depending on the polyelectrolyte rigidity, the concentration regime and the ionic strength [217, 218]. We will discuss the general issue of polyelectrolyte size further at the end of this section.

To compare this model with the experimental data in Figure 3.2B and Figure 3.2C we calculate the total fs-ESHS signal by numerically integrating the scattering pattern in the forward half-plane:

$$S_{int} = \int_{-\pi/2}^{\pi/2} S(\theta) d\theta \quad (3.3)$$

The maximum scattering angle θ_{max} of Figure 3.2C can be obtained by computing the maximum of the scattering pattern in the forward half-plane, i.e. by numerically solving for θ :

$$\left. \frac{dS(\theta)}{d\theta} \right|_{\theta_{max}} = 0 \quad (3.4)$$

The computed S_{int} and θ_{max} values are shown in Figure 3.2B and Figure 3.2C as solid lines. Using the single fit parameter α , which takes a best-fit value of $\alpha = 5$, the curve for the total fs-ESHS intensity produced by this model (Figure 3.2B) matches well with the measured values (circles), as well as the maximum scattering angle as a function of HA concentration (Figure 3.2C). Considering that both the integrated intensity as well as the angle of maximum intensity are found with the same single fit parameter suggests that our model captures the essentials of the fs-ESHS response.

3.2.3. Concentration dependence and polyelectrolyte size

The modeling provides insight into the unusual concentration dependence of the fs-ESHS response of HA solutions. The initial rise in the intensity with HA concentration is due to the increasing number density of the number of HA chains and their extended hydration shells. At the same time, increasing the HA concentration adds counter-ions to the solution which increases the ionic strength and decreases the Debye screening length. This has three consequences: First, the HA chain collapses as the intra-chain repulsion is weakened (reducing R). Second, the extent of the hydration shells decreases due to increased Debye

screening (reducing κ^{-1} and R'). Third, long-range charge-charge correlations between different HA chains are suppressed as well. The peak integrated intensity at $\sim 5 \mu\text{g/mL}$ is reached when the positive contribution from an increasing number density of HA starts to be outweighed by the opposing contributions from enhanced Debye screening. The increase in the scattering angle (θ_{max}) with HA concentration shown in Figure 3.2C reflects the shrinking of both R and R' .

Figure 3.4A presents a comparison of the variation of R (i.e. the size of the polymer as determined by water orientation around a particular charge distribution), and R' (i.e. the size of the polymer chain plus the region with a non-negligible electrostatic potential), together with the contour length L_c (i.e., the length at maximum extension), the electric persistence length L_p (i.e. the length over which the tangential electrostatic correlations are lost, and the free radius per HA, R_{free} . L_p and R_{free} are calculated as follows: $L_p = \frac{\lambda_B}{4a^2\kappa^2}$ [212, 213], $R_{free} = \left(\frac{3M_{HA}}{4\pi c_{HA}N_A}\right)^{1/3}$, where $\lambda_B = 0.71 \text{ nm}$ is the Bjerrum length in water, κ^{-1} is the Debye screening length, $a = 1.02 \text{ nm}$ is the distance between charges on HA, $M_{HA} = 1349 \text{ Da}$ is the average molar weight of HA, N_A is Avogadro's constant and c_{HA} is HA concentration in $\mu\text{g/mL}$. It can be seen that the contour length is larger than all other size parameters, which makes sense because L_c represents the end-to-end distance of a fully stretched chain. L_p is larger than R and R' for most of the low ionic strength range ($< 20 \mu\text{g/mL}$). The reason for this is an over-estimation of the electrostatic interactions compared to the distance derived from the fs-ESHS scattering because the OSF theory is valid only for rigid polyelectrolytes, i.e. when $a \ll \sqrt{\lambda_B L_0}$ [219]. With $a = 1.02 \text{ nm}$ the distance between charges on HA, $\lambda_B = 0.71 \text{ nm}$, and $L_0 \approx 8 \text{ nm}$ the intrinsic persistence length of HA [220], we obtain $\sqrt{\lambda_B L_0} \approx 2.4 \text{ nm}$, which does not fully satisfy the condition.

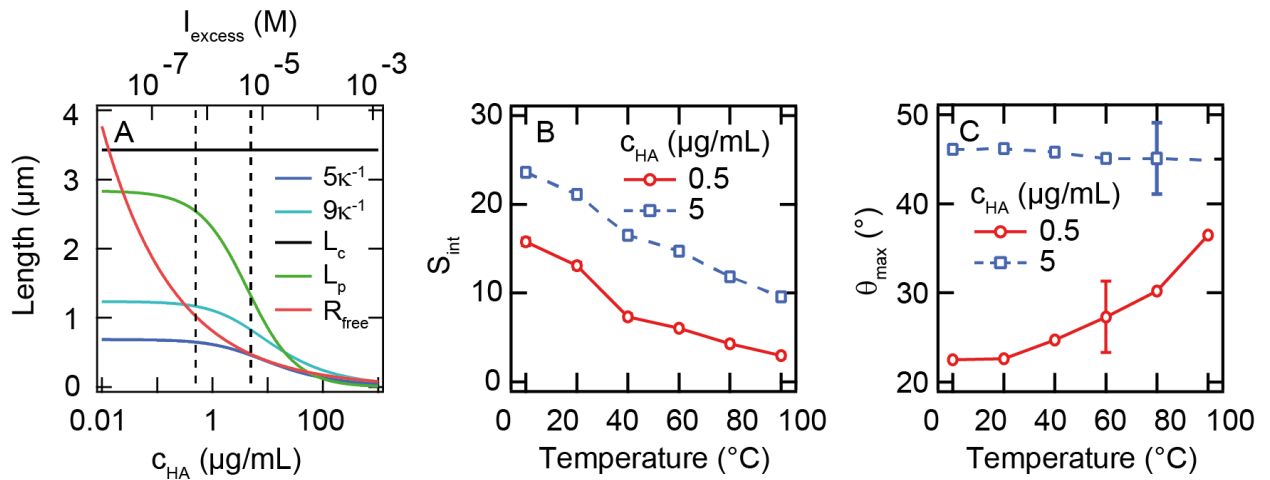


Figure 3.4: Relevant length scales as a function of HA concentration and the temperature dependence of the fs-ESHS response of HA in H_2O . (A) The relevant lengths as a function of HA

concentration: the Debye length κ^{-1} , the contour length L_C , the electric contribution to the persistence length L_p , and the free radius per HA chain R_{free} . (B) Temperature dependence of total fs-ESHS intensity and (C) maximum scattering angle at HA concentrations of 0.5 $\mu\text{g/mL}$ (red circles) and 5 $\mu\text{g/mL}$ (blue squares).

The size determined via fs-ESHS (R) tells us something about the charge induced water orientation. This is completely different from standard experimental methods to determine polyelectrolyte size, which rely on refractive index contrasts as experienced by light (dynamic light scattering), x-rays (small-angle X-ray diffraction), or neutrons (small-angle neutron scattering) [218]. Besides the difference in contrast mechanism, there is also a difference in sensitivity range: fs-ESHS works well at very low concentrations and ionic strengths, as it is very sensitive to the electrostatic field effects, whereas the linear light scattering methods perform well at high ionic strength and concentration.

3.2.4. Extended hydration shell

Finally, we consider another method to determine the extended hydration shell around the polyelectrolyte. Figure 3.4A also shows the radius based on the available free volume (red line, R_{free}). When $R_{free} > R'$ there is no interaction between the HA chains or soft shells ($c_{HA} < 0.3 \mu\text{g/mL}$). At higher concentrations there is, justifying the use of the structure factor in the model. In order to determine if R , R' or R_{free} has anything to do with the hydration shell around the semi-flexible HA chain, we have performed fs-ESHS experiments at different temperatures. Changing the temperature will change the importance of random thermal motion compared to ion-water (charge-dipole) interactions, and it will also change the screening length. With increasing temperature, the orientational order will reduce, leading to a decrease in the integrated fs-ESHS intensity S_{int} . This arises both from a change in orientational order as well as a potential change in effective size, due to the altered dipole-charge interactions. If the effective size decreases with temperature as well, we expect to see an increase in the scattering angle of maximum intensity θ_{max} . However, if the effective size is limited by the available free volume per HA chain, we would not expect to see an additional change in θ_{max} . In this case, the size of the hydration shell is approximately the radius of free volume per HA chain shown in Figure 3.4A.

Figure 3.4B shows the temperature dependence of the total fs-ESHS intensity measured between 0 and 100 $^{\circ}\text{C}$ at two HA concentrations: 0.5 and 5 $\mu\text{g/mL}$, indicated by the dashed lines in Figure 3.4A. As expected, the intensity decreases monotonically with temperature due to decreased orientational order. The increase of temperature from 0 to 100 $^{\circ}\text{C}$ also increases the Debye length by 20 nm at $c_{HA} = 0.5 \mu\text{g/mL}$ and by 15 nm at $c_{HA} = 5 \mu\text{g/mL}$. This effect seems to be insignificant compared to the decrease in the orientational order from thermal motion. The maximum scattering angle θ_{max} as a function of temperature

for the two HA concentrations is plotted in Figure 3.4C. At the HA concentration of 0.5 $\mu\text{g/mL}$ we observe a rise in θ_{max} with temperature which reflects the shrinking of the extended hydration shell. However, at an HA concentration of 5 $\mu\text{g/mL}$ θ_{max} is independent of temperature, indicating that the size of the hydration shell is constant. We can, therefore, conclude that the theoretical extent of the hydration shells is at least equal to the free radius of HA at 5 $\mu\text{g/mL}$ which amounts to a shell with a radius of 475 nm. Applying the same reasoning for D_2O , we estimate the size of the hydration shell in D_2O at 30 $\mu\text{g/mL}$ to be 260 nm per HA or 45% of the value for H_2O .

A shell with a radius of 475 nm holds $\sim 1.3 \times 10^{10}$ water molecules and one polymer chain, whose volume will displace ~ 20000 water molecules. Compared to the value found for R , the size of the polymer chain as given by the distribution of charge, there is an additional shell of oriented water with a thickness of ~ 17 nm, or ~ 60 water molecules in diameter. This number of hydrating water molecules that surround the charged HA polymer is similar to the number of ~ 77 water molecules that were found around electrolytes in an earlier fs-ESHS study [41].

3.3. Conclusions

We have probed the extended hydration of hyaluronan, a biological anionic polyelectrolyte, using fs-ESHS. The source of the measured coherent second-harmonic radiation is assigned to water molecules that interact with the electrostatic field of spatially correlated charges on the polyelectrolyte chain. The fs-ESHS response of HA is compared to that of dilute electrolyte solutions, which also display an increase in second-harmonic intensity at very low ionic strengths ($\sim 10^{-5}$ M). Unlike the simple electrolyte solutions, the fs-ESHS intensity vs. HA concentration curve displays a maximum at an intermediate concentration (~ 5 $\mu\text{g/mL}$) that is 6x larger than the intensity scattered by simple electrolytes. This difference is explained by the larger magnitude of the electrostatic field generated by HA compared to randomly distributed ions. At high concentrations, the intensities scattered by HA and electrolyte solutions converge to the same plateau. This is explained by an enhancement of Debye screening with increasing HA concentration which results in a shrinkage of the hydration shells. A theoretical model that treats HA as a flexible charged particle surrounded by a spherical shell of polarized water molecules qualitatively describes the changes in the fs-ESHS intensity and angle as a function of HA concentration (ionic strength). Using this model we propose a method to determine the size of polyelectrolytes in dilute solutions. Temperature-dependent fs-ESHS experiments were used to estimate the size of the extended hydration shell, which amounts to a few hundred nanometers for a concentration of 5 $\mu\text{g/mL}$. Similar to simple salt solutions, a clear difference between light and heavy water is observed. In heavy water, the fs-ESHS intensity maximum is

4.3× lower and occurs at 2.4× higher HA concentration (ionic strength). This difference cannot be explained by the proposed model and likely stems from the same nuclear quantum effect observed in simple electrolyte solutions [41]. This isotope effect indicates that the interactions leading to the observed behavior are not only charge-water interactions but also contain interactions of the electrostatic field with the collective hydrogen bond network.

3.4. Appendix

3.4.1. Full fs-ESHS patterns of HA in H₂O

Figure 3.5A shows the scattering patterns of NaCl solutions in H₂O obtained in ppp polarization combination. The integrated fs-ESHS intensity S_{int} and maximum scattering angle θ_{max} as functions of HA concentration shown in Figure 3.2B and Figure 3.2C in the main text were obtained from scattering patterns of HA solutions in H₂O measured in ppp polarization combination. The scattering patterns that were used for the analysis are shown in Figure 3.5A. An illustration of how S_{int} and θ_{max} were extracted from the pattern are shown in Figure 3.5B.

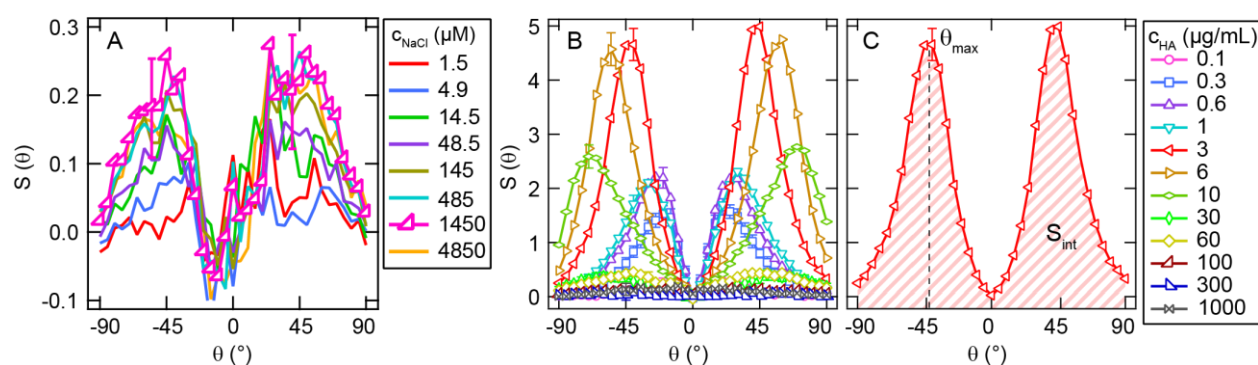


Figure 3.5: fs-ESHS patterns of HA solutions in H₂O at various HA concentrations. (A) fs-ESHS patterns of NaCl in H₂O obtained in PPP polarization combination. (B) All fs-ESHS patterns of HA in H₂O obtained in PPP polarization combination used in Figure 3.2. (C) An example of a pattern with the maximum angle θ_{max} indicated and the integrated intensity S_{int} shown as the area under the curve of the pattern. The patterns were recorded in ppp polarization combination. The two symmetric lobes of the patterns shift towards larger scattering angles with increasing HA concentration (mol. wt. 1349 kDa). The increasing scattering angle corresponds to a decreasing length scale that is being probed.

3.4.2. fs-ESHS in sss polarization direction

The theory of second-harmonic scattering predicts that spherically symmetric objects with a locally isotropic surface generate no response in sss polarization combination [160, 162] (all beams polarized perpendicular relative to the scattering plane). This was confirmed for HA solutions by a fixed-angle measurement at a 90° scattering angle shown in Figure 3.6. The

lack of fs-ESHS response in the sss polarization combination confirms that the hydration shells of HA are spherical.

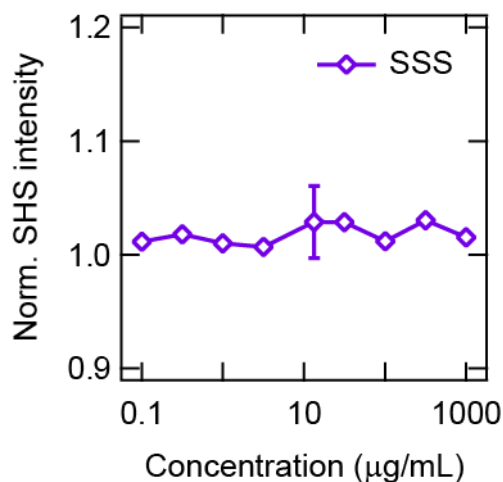


Figure 3.6: Absence of fs-ESHS response in sss polarization combination. Normalized second-harmonic scattering intensity measured at a fixed angle of 90° in sss polarization combination as a function of HA concentration (mol. wt. 1349 kDa). The lack of response in this polarization is predicted by the theory of second-harmonic scattering for particles with an isotropic surface.

3.4.3. Dependence of fs-ESHS of HA on ionic strength

The fact that the fs-ESHS response of HA in ppp polarization combination originates from long-range electrostatic interactions was verified by measuring the effect of added salt on the fs-ESHS intensity at a constant HA concentration. The total fs-ESHS intensity as a function of excess ionic strength is shown in Figure 3.7A. Adding excess NaCl decreases the Debye screening length as shown in Figure 3.7B. We see that the fs-ESHS response drops with added NaCl and nearly vanishes at 1000 μM of excess NaCl.

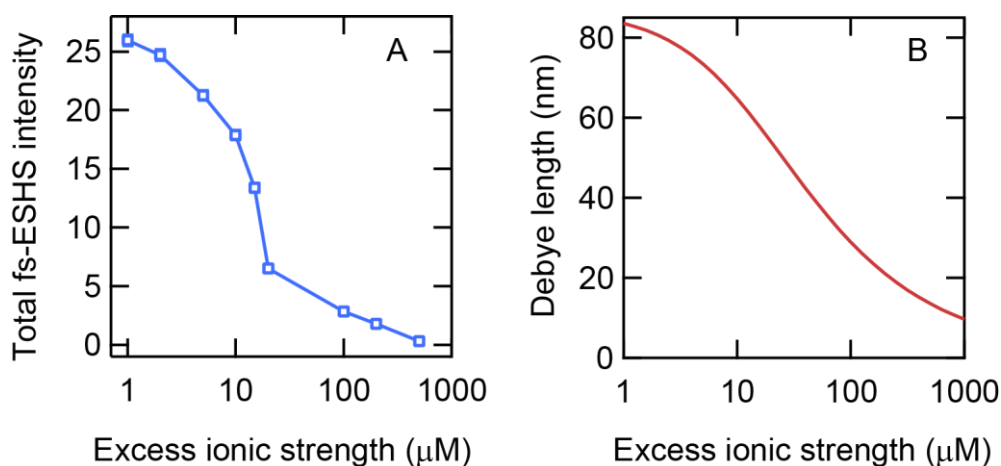


Figure 3.7: Dependence of fs-ESHS response of HA and of the Debye length on excess ionic strength. (A) Total fs-ESHS intensity of a HA solution ($c = 10 \mu\text{g/mL}$, mol. wt. 1145 kDa) recorded in ppp polarization combination as a function of excess ionic strength from added NaCl. (B) The Debye screening length as a function of excess ionic strength assuming a base ionic strength of $17.5 \mu\text{M}$.

3.4.4. Power dependence and elasticity of the fs-ESHS process

The intensity of light generated via second-harmonic process scales quadratically with incident power [102]. To verify that the detected light does indeed originate from a second-order optical process, we measured the intensity as a function of average incident laser power. The result in Figure 3.8 is plotted as the measured photon counts divided by the square of the incident power. The resulting curve is constant, which confirms that the detected light is generated via a second-order optical process.

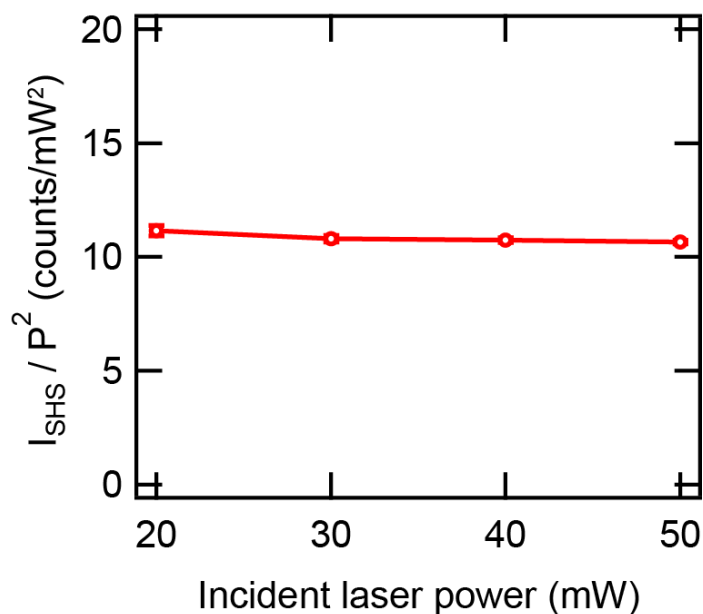


Figure 3.8: Verification of the power dependence of the fs-ESHS intensity. Scattered second-harmonic intensity from a HA solution ($c = 5 \text{ ug/mL}$, mol. wt. 1349 kDa) measured at 90° angle in ppp polarization combination divided by the square of the incident laser power as a function of incident laser power. The flat line indicates that the power dependence is purely quadratic which means that no lower- or higher-order optical effects contribute to the detected signal.

To confirm that changes in the measured intensity originate from second-harmonic scattering and not from another quadratic optical process such as two-photon fluorescence or hyper-Raman scattering, we measured the spectra of the light scattered from the HA solutions (mol. wt. 1145 kDa) at various HA concentrations in H_2O . The obtained spectra are shown in Figure 3.9A. Spectra were recorded in ppp polarization combination at 45° scattering angle in the wavelength range between 400 and 650 nm. A low-pass filter (850 nm cutoff) was placed in the detector path to block the scattered fundamental wavelength. A background acquired with the laser beam blocked was subtracted from each spectrum. It can be seen that the second-harmonic peak at 0 cm^{-1} (514 nm) dominates the spectrum. There are also 3 observable Stokes hyper-Raman peaks at approx. 764 cm^{-1} (535 nm), 1662 cm^{-1} (562 nm), 3062 cm^{-1} (610 nm) corresponding to the librational mode of H-bonded H_2O molecules, the bending mode of H_2O and the stretching mode of H_2O , respectively [221]. No Anti-Stokes hyper-Raman scattering (negative Raman shift) and no fluorescence (broad features) were observed. Similar hyper-Raman spectra of water acquired with different laser sources were previously reported in the literature [222, 223]. We can see that the hyper-Raman peaks are not influenced by HA whereas the intensity of the second-harmonic peak at 0 cm^{-1} varies with HA concentration as can be seen in detail in Figure 3.9B. Moreover, in the actual scattering

experiments, the band-pass filters used (515 ± 25 and 515 ± 5 nm) blocked most of the hyper-Raman light.

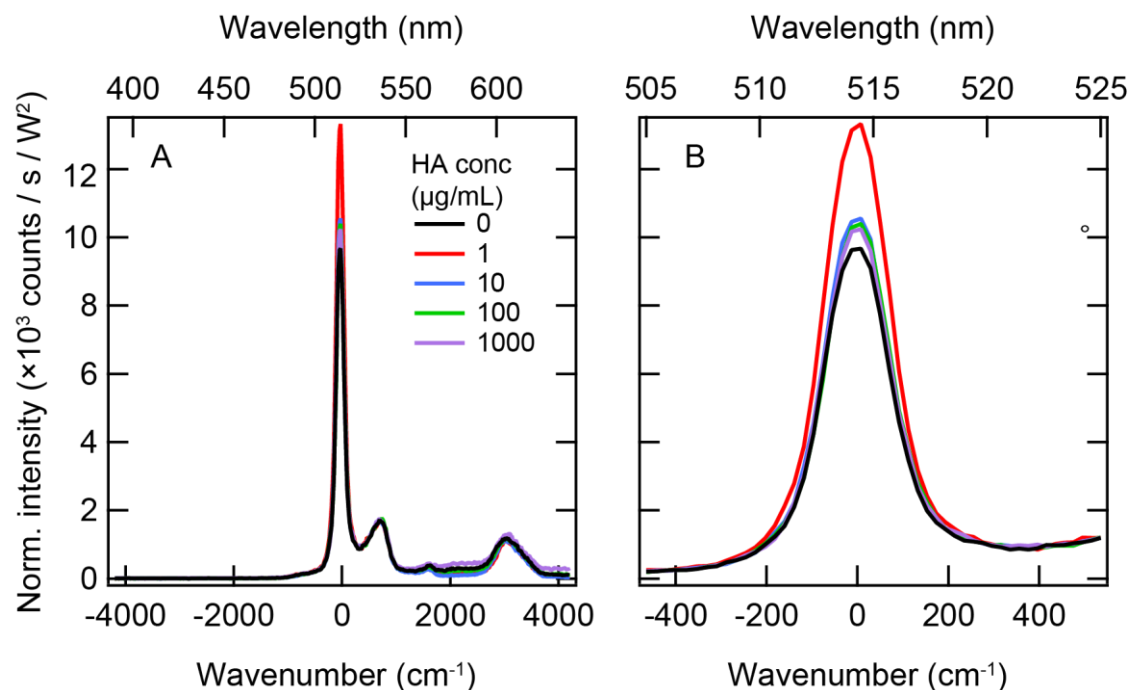


Figure 3.9: Verification of the elasticity of fs-ESHS from HA in H₂O. (A) Spectra of the light generated in the fs-ESHS experiments on HA (mol. wt. 1145 kDa) in H₂O at various HA concentration. The bottom horizontal axis shows the Raman shift with respect to the second-harmonic wavelength (514 nm), the top axis shows the approximate wavelength. The second-harmonic peak is the dominant feature of the spectrum. There are also 3 observable Stokes hyper-Raman peaks at approx. 764 cm⁻¹ (535 nm), 1662 cm⁻¹ (562 nm), 3062 cm⁻¹ (610 nm) corresponding to the librational mode of H-bonded H₂O molecules, the bending mode of H₂O and the stretching mode of H₂O, respectively. Only the second-harmonic peak varies with HA concentration. No Anti-Stokes hyper-Raman scattering or fluorescence is observed below 1000 µg/mL. (B) Detail of the second-harmonic peak.

Chapter 4: Polyelectrolytes induce water-water correlations that result in dramatic viscosity changes and nuclear quantum effects

Ions interact with water via short-ranged ion-dipole interactions. Recently, an additional unexpected long-ranged interaction was found: The total electric field of ions influences water-water correlations over tens of hydration shells, leading to the Jones Ray effect, a 0.3% surface tension depression. Here, we report long-range interactions in polyelectrolyte solutions contributing significantly to both molecular as well as macroscopic properties. Femtosecond elastic second harmonic scattering shows that long-range electrostatic interactions are remarkably strong in aqueous polyelectrolyte solutions leading to an increase in water-water correlations. This increase is shown to play a role in the reduced viscosity, which changes more than two orders of magnitude with polyelectrolyte concentration. Using D₂O instead of H₂O shifts both the fs-ESHS and the viscosity curves by a factor of ~10 and reduces the maximum viscosity value by 20-300 %, depending on the polyelectrolyte. These phenomena cannot be explained using a mean-field approximation of the solvent and point to nuclear quantum effects.

This chapter is based on an article by Jan Dedic, Halil I. Okur, and Sylvie Roke entitled: "Polyelectrolytes induce water-water correlations that result in dramatic viscosity changes and nuclear quantum effects" that has been published in the journal Science Advances.

Dedic, J., Okur, H. I. & Roke, S. Polyelectrolytes induce water-water correlations that result in dramatic viscosity changes and nuclear quantum effects. Sci. Adv. 5, eaay1443, doi:10.1126/sciadv.aay1443 (2019).

4.1. Introduction

Most biochemical reactions occur in aqueous environments, underlining the importance of water for life. More than just a passive background, water actively participates in various processes, such as enzyme and ion channel activity [57], protein folding and stability [177], self-assembly [224], molecular recognition [225, 226], charging [227] and lubrication [228]. This is possible because water molecules are strongly responsive to the electrostatic fields of simple ions and charged macromolecules such as polyelectrolytes or to polar groups. In order to understand the complex role that water plays in biochemical processes, it is necessary to study the interaction of ions and ionic groups with water on both the molecular as well as the macroscopic level. It is known that various macroscopic properties of aqueous solutions are influenced by ions, such as the dynamic viscosity and the surface tension [12, 229, 230]. The changes in these properties have their origins in the molecular-level interactions between ions and water. The interactions of ions with water at ionic strengths > 0.1 M have been subject to numerous investigations using X-ray scattering [231], neutron scattering [232], IR spectroscopy [9], Raman scattering [233, 234], terahertz spectroscopy [235] and molecular dynamics (MD) simulations [37, 205, 207, 236] among others. These studies show that the molecular structure of water in the vicinity of ions is strongly influenced by the valence, polarizability and size of the ion [36, 237, 238] and that significant perturbation of the structure and dynamics of liquid water are observed within the first three hydration shells. In addition, the ion-water interaction is influenced only minimally by nuclear quantum effects [41, 239-241].

Recent femtosecond-elastic second harmonic scattering (fs-ESHS) experiments performed by us [41, 152] and others [206] together with subsequent computational studies [207-209] have provided a new dimension to the understanding of water – ion interactions. In an fs-ESHS experiment, the nonlinear polarization of a liquid composed of non-centrosymmetric molecules is measured. This polarization arises from two sources [115, 146, 150]: The first contribution arises from the polarization of individual molecules and gives rise to incoherent (hyper-Rayleigh) scattering [146, 148]. It occurs in all polarization combinations of the in- and out-going optical fields. The second contribution arises from the coherent addition of the second-harmonic (SH) signal from different but orientationally-correlated molecules. This coherent contribution can be measured only in certain polarization combinations of the optical fields, for example with all beams polarized parallel to the scattering plane (ppp polarization combination). Performing fs-ESHS experiments on 21 different aqueous electrolyte solutions spanning a concentration range from $1\ \mu\text{M}$ to 0.1 M revealed a universal increase in the fs-ESHS intensity, but only for polarization combinations that contain coherent emission. This increase was further absent for neutral solutes and displayed remarkably different curves for H_2O and D_2O . It was proposed that the total long-ranged electrostatic field

of the ions already present at low salt concentrations perturbs the water-water correlations in the H-bond network of water and is subject to a significant and as of yet unexplained nuclear quantum effect. Revisiting key elements of the experiments and interpretation here, Figure 4.1A shows fs-ESHS data for NaCl in H₂O and D₂O solutions adapted from Refs. [40, 41]. We can see that the fs-ESHS response already increases at a salt concentration of 10 μ M, and saturates at \sim 1 mM. Since these correlations are already observed at ion separations of \sim 20 nm, the phenomenon reports on long-ranged interactions. The D₂O solutions in Figure 4.1A display the same trend but with a lower saturation value and higher onset concentration compared to H₂O. Although the H₂O curve in the ppp polarization combination can be explained using a mean-field Debye-Hückel model that describes the influence of the total electrostatic field in the solution on the molecular orientational order [41, 152, 208, 209], the model fails to explain the large discrepancy between H₂O and D₂O (as well as other models that represent water only by a dielectric constant). The H₂O/D₂O difference indicates that the dissolved ions influence collective H-bonding interactions. Water has two distinct modes for breaking H-bonds (illustrated in Figure 4.1B) whose relative strengths are different in H₂O and D₂O. Since fs-ESHS probes orientational correlations between water molecules, it has more sensitivity towards detecting H-bond breaking by bending rather than stretching, and can clearly distinguish H₂O from D₂O.

The weak ion-induced restructuring of the H-bond network of water was connected to the Jones-Ray effect [210], which entails an anomalous and isotope-dependent \sim 0.3 % reduction of the surface tension at the fs-ESHS saturation concentrations. The ion-induced increase in orientational order in the aqueous bulk solution gives rise to an entropic penalty, which causes a reduction in the surface tension [41, 210, 211]. This long-range interaction of the ionic electrostatic field with water is a new and poorly understood phenomenon that warrants further investigation. One could ask whether long-ranged correlations in water are consequential since, until now, the reported effects they cause represent only a minor (0.3 %) change in macroscopic properties [38].

Here, we report that long-range reordering of the H-bond network of water via weakly-screened electrostatic interactions in polyelectrolyte solutions causes significant changes in the reduced specific viscosity. Anionic polyelectrolytes, poly(acrylic acid) (PAA) and poly(styrene sulfonate) (PSS) (molecular structures displayed in Figure 4.1C) are shown to strongly enhance the orientational order of water, starting at polyelectrolyte concentrations as low as 1 nM. The changes in the orientational order of water are more pronounced in H₂O than in D₂O, consistent with the behavior observed in the solutions of simple salts. The reduced specific viscosity of the polyelectrolyte solutions follows a similar trend as the water ordering, for both H₂O and D₂O, and changes of more than two orders of magnitude are observed. We

conclude that long-range interactions between spatially correlated ionic groups on the polyelectrolytes and the H-bond network have a significant impact on the reduced viscosity. Although traditional mean-field models based on inter- and intra- polyelectrolyte correlations can qualitatively explain the viscosity anomaly in H₂O, the models fail to predict the discrepancy between H₂O and D₂O [242, 243]. This points to water-water correlations having an influence on the anomalous viscosity of polyelectrolyte solutions. In addition, our data suggest that H-bond breaking through rotations occurs more readily than through H-bond stretching and is relatively more important for viscosity.

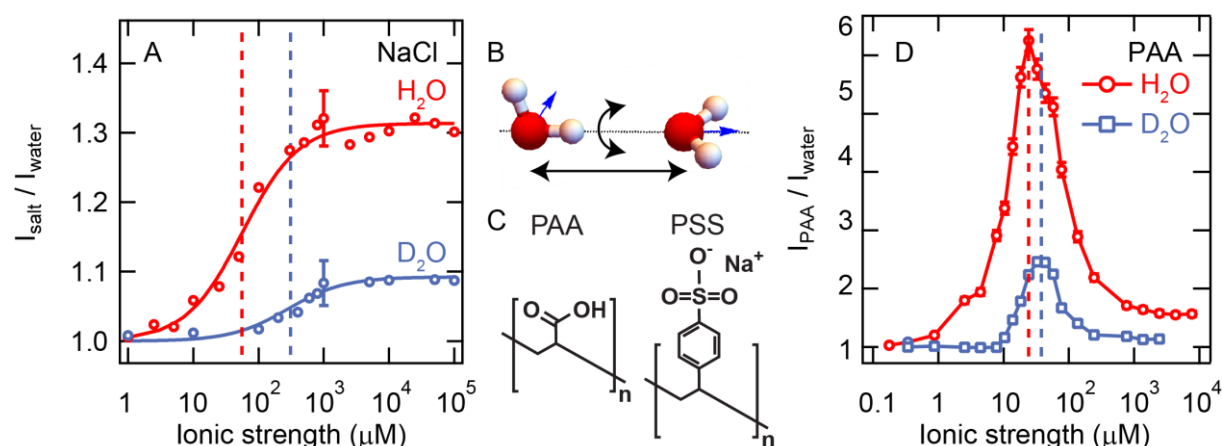


Figure 4.1: Long-range distortion of the orientational order of water. (A) fs-ESHS intensities, relative to that of pure water, of NaCl in H₂O and D₂O obtained at a scattering angle of 90° in the ppp polarization combination. The fs-ESHS data are adapted from Refs. [40, 41]. The dashed lines indicate the concentrations of half-saturation. (B) Illustration of two H-bonded water molecules that are orientationally correlated. The black arrows represent different axes along which H-bonds can be broken. fs-ESHS is mostly sensitive to the breaking of this H-bond via rotation (black curved arrow). In a D₂O molecule, the H-bond bending mode is predicted to be stronger than in H₂O while the H-bond stretching mode is expected to be weaker due to nuclear quantum effects. (C) Molecular structures of PAA and PSS polyelectrolytes. (D) fs-ESHS intensities, relative to pure water, of PAA in H₂O and D₂O obtained at a scattering angle of 90°. The dashed blue and red lines indicate peak intensity concentrations. All fs-ESHS data was recorded with beams polarized parallel to the horizontal scattering plane (ppp). The molecular weight of PAA was 450 kDa.

4.2. Experimental section

4.2.1. Chemicals and sample preparation

Poly(acrylic acid) - mol. wt. 450 kDa (Polysciences, Inc), sodium poly(styrene sulfonate), sodium salt – mol. wt. 1000 kDa (Polysciences, Inc), and poly(ethylene glycol) – mol. wt. 400 kDa (Sigma) in powder were used as received. The structure of PSS and PSS are shown in Figure 4.1C. NaCl (99.999%) was purchased from Acros. Stock polymer solutions were

prepared by dissolving the powder in water (H₂O or D₂O). The samples were prepared by subsequent dilution of the stock solutions to obtain the desired polymer concentration. Stock NaCl solutions were filtered through Millipore Millex-VV 0.1-mm polyvinylidene difluoride membrane filters. Ultrapure H₂O with an electrical resistance of 18.2 MΩcm was obtained from a Milli-Q UF-Plus instrument (Millipore Inc.). For experiments with heavy water, the D₂O used contained 99.8% D atoms and had an electrical resistance of >2 MΩ·cm (Armar).

4.2.2. fs-ESHS measurements

The experimental conditions used for fixed-angle measurements were the same as in Refs. [40, 41, 149]. The detection angle was set to 90° with an acceptance angle of 11.4°. Each data point is an average of 3 - 5 measurements. Each measurement is an average of 50 expositions of 1 s integration time, using $50 \times 2 \times 10^5$ pulses in total. The gate width was 10 ns. The polarization combination is denoted using a 3-letter code where the first letter indicates the polarization of the outgoing SH light and the last two letters indicate the polarization of the incident fundamental light. The polarization can either be in the scattering plane (p-parallel) or perpendicular to the plane (s-perpendicular).

To compare fs-ESHS response with reduced specific viscosity we introduced another metric: integrated fs-ESHS intensity (S_{int}). To obtain this quantity, a scattering pattern is recorded at 5° steps between -90° and +90° with an opening angle of 3.4°. The pattern is normalized at each angle θ with respect to pure water using the formula:

$$S(\theta) = \frac{I_{solution}(\theta) - I_{water}(\theta)}{I_{HRS,water}(\theta)} \quad (4.1)$$

where $I_{solution}(\theta)$ and $I_{water}(\theta)$ stand for the average second-harmonic count rate at a scattering angle θ recorded in the same polarization combination (ppp or sss) while $I_{HRS,water}$ is the intensity of hyper-Rayleigh scattering (HRS) and was always recorded with all beams polarized perpendicular to the scattering plane (sss). The integrated fs-ESHS intensity is then calculated as:

$$S_{int} = \sum_{\theta \neq 0} S(\theta) \quad (4.2)$$

4.2.3. Dynamic viscosity measurements

Dynamic viscosities were measured using an Ubbelohde-type glass capillary viscometer (Paragon Scientific Ltd.) immersed in a temperature-controlled water bath (ET 15S, Lauda

Scientific GmbH). The measurements were performed at 25.00 ± 0.01 °C. The viscometer with the loaded liquid was allowed to reach equilibrium with the bath for at least 4 minutes before measurement. The elution times were measured with a time-stamped digital camera (720p @ 24 fps, Huawei Mi A1) that recorded the passing of the liquid's meniscus between the two marked positions on the viscometer. Each sample was measured at least 3 times. The reduced specific viscosity was calculated as:

$$\eta_{red} = \frac{\eta_{solution} - \eta_{water}}{c_m \eta_{water}} \quad (4.3)$$

where η_i is the measured dynamic viscosity based on the elution time and c_m is the monomer concentration of the polyelectrolyte.

4.2.4. Femtosecond snapshots of long-range order

The orientational correlations between water molecules in solutions of PAA and PSS were measured at different concentrations (excess ionic strengths). The excess ionic strength (I) of the solution, due to the dissolved and partially dissociated polyelectrolytes was calculated as $I = 0.5c_m f$, where c_m is the monomer concentration in mol/L and f is the percentage of dissociated counter-ions. According to Manning's theory of counter-ion condensation [215, 244], the degree of ionization is $f = b/\lambda_B = 0.35$, where $b = 0.25$ nm is the distance between ionizable groups on the polyelectrolyte chain and $\lambda_B = e^2/4\pi\epsilon_0\epsilon k_B T = 0.71$ nm, is the Bjerrum length in water with e the elementary charge, ϵ_0 the vacuum permittivity, $\epsilon \approx 78.5$ the dielectric constant of water, k_B the Boltzmann constant and temperature $T = 298$ K. Figure 4.1D shows the fs-ESHS response of PAA solutions as a function of PAA concentration (ionic strength) recorded at a fixed scattering angle $\theta = 90^\circ$ with all beams polarized in the horizontal scattering plane. It can be seen that the fs-ESHS response from H₂O solutions increases from a value of 1 at near-infinite dilution and reaches a maximum of 6.2 after which the intensity drops again and levels off above an ionic strength of ~ 1 mM. The increase in the scattered intensity with concentration might be intuitively interpreted in terms of an increasing number density of bare polyelectrolytes. This simple explanation is, however, contradicted by the subsequent decrease in fs-ESHS intensity. Moreover, incoherent fs-ESHS measurements (recorded with all beams polarized in the direction vertical to the scattering plane - sss) of the same solutions, shown in Figure 4.2, display no increase in the fs-ESHS response at the concentrations used here. If the bare polyelectrolytes contributed significantly to the SH signal, we would expect to see an increase in the incoherent response. The reason why the contribution of the bare polyelectrolytes is insignificant compared to their hydration shells can be understood by noting

that in a non-resonant fs-ESHS experiment, the emitted SH intensity scales quadratically with the number of orientationally-correlated molecules in the focal volume [102]. Even at the highest polyelectrolyte concentration used here, there are still > 1000 water molecules per monomer, leading to an up to 10^6 times higher contribution from the water than from the polyelectrolytes.

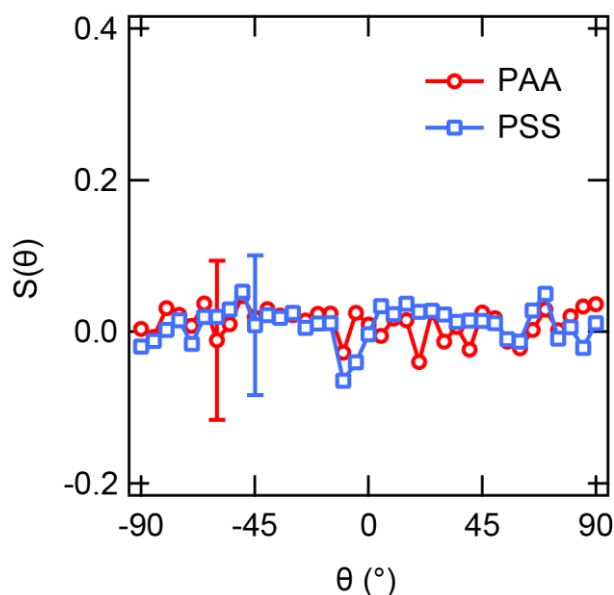


Figure 4.2: Negligible contribution of polyelectrolytes to second-harmonic scattering. Water normalized fs-ESHS scattering pattern of PAA (11 nM, ionic strength 12 μ M) and PSS (5 nM, ionic strength 4 μ M) in H_2O obtained in sss polarization combination which reports only on incoherent scattering. The absence of signal shows that the bare polyelectrolytes do not contribute significantly to the fs-ESHS response.

Figure 4.1D also shows that a significant discrepancy occurs when the same fs-ESHS experiment is conducted using D_2O as the solvent instead of H_2O . The fs-ESHS trend for D_2O is significantly altered compared to H_2O : the maximum intensity is $2.4\times$ lower and appears at a $1.5\times$ higher concentration compared to H_2O . The presence of a saturation intensity at high concentration, a low onset ionic strength and the difference between H_2O and D_2O is reminiscent of the observations for aqueous salt solutions of Figure 4.1A. The main difference here is the appearance of a pronounced peak in the concentration curve compared to electrolyte solutions. This behavior stems from the interactions between the electrostatic field of the ionic groups on polyelectrolytes and the H-bond network of water as discussed in the previous chapter. At very low ionic strength the polyelectrolyte chains are in an extended conformation due to strong intra-chain electrostatic repulsion [212, 213, 245, 246] and different polyelectrolytes are expected to be correlated with each other [242, 247-249]. The ionized groups on the polyelectrolyte chains, therefore, do not move freely like simple electrolyte ions but are limited in their spatial arrangement both by the stiffness of the polyelectrolyte chains

and repulsions between different chains. These intra- and inter-chain correlations impact the orientational order of water molecules that are associated with each ionic group as extended hydration shells. The long-range correlations in polyelectrolyte solutions are possible due to a combination of a high degree of ionization of the polyelectrolytes and a large Debye screening length. At an ionic strength of $I = 10 \mu\text{M}$, the Debye length is $\kappa^{-1} = \sqrt{2\pi\lambda_B/10^3 N_A I} \approx 100 \text{ nm}$ where λ_B is the Bjerrum length as defined before and N_A is the Avogadro number. Since the ionic strength is a function of polyelectrolyte concentration, increasing the polyelectrolyte concentration shortens the Debye length which suppresses long-range spatial correlations [212, 213, 249]. The importance of Debye screening for the fs-ESHS response was confirmed by measuring the effect of varying ionic strength on the measured fs-ESHS intensity shown in Figure 4.3. The fs-ESHS intensity drops rapidly with ionic strength and virtually disappears above 1 mM. The total electrostatic field in the liquid, and consequently the water-water correlations that are induced by it, are expected to be the highest when the chain concentration is maximized up to the point where the spatial correlations in and between the polyelectrolyte chains begin to disappear due to Debye screening. Such behavior would give rise to a maximum in the fs-ESHS response. For PAA in H_2O the fs-ESHS intensity maximum occurs at an ionic strength of $\sim 24 \mu\text{M}$, which corresponds to a Debye length of 62 nm.

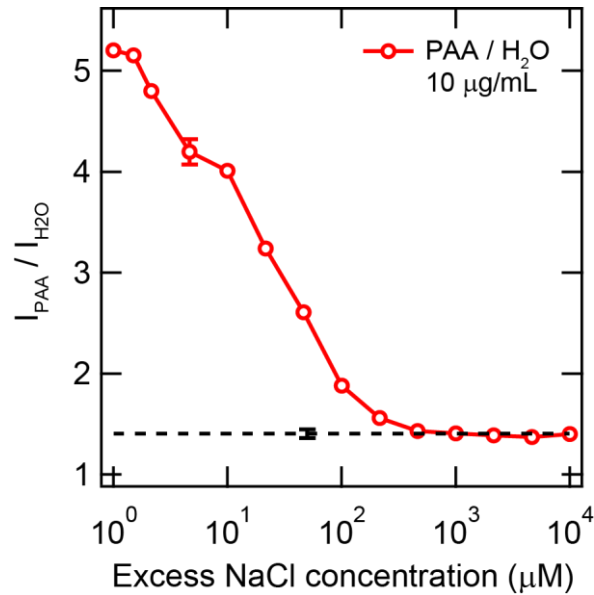


Figure 4.3: fs-ESHS response of PAA disappears with the addition of salt. The normalized fs-ESHS intensity measured at 90° scattering angle of PAA in H_2O ($10 \mu\text{g/mL}$) as a function of excess NaCl concentration (red circles). The normalized intensity relative to neat water levels off at $\sim 1 \text{ mM}$ NaCl concentration at ~ 1.4 , matching the plateau value for electrolyte solutions (horizontal dashed line).

4.2.5. Viscosity

The fs-ESHS data of Figure 4.1D suggest a large degree of polyelectrolyte-induced orientational correlations between the water molecules. Would such an increase in correlations also have an influence on a macroscopic observable? Viscosity is a good candidate since the degree of structural correlations in a solvent has a significant influence on viscosity [18, 241, 250-252]. This is apparent in the 23 % higher viscosity of pure D₂O compared to H₂O at room temperature [20, 23] which cannot be entirely accounted for by a difference in mass (moment of inertia) of the two isotopes of water. The residual difference in viscosity was assigned to stronger H-bonding in D₂O [2, 18]. Recent work from our group has shown that there is an ion-specific correlation between the viscosity and the intensity of fs-ESHS experiments for high electrolyte concentrations [149]. Studies from as early as the 1950s have reported an anomalous increase in the reduced specific viscosity of dilute aqueous polyelectrolyte solutions which does not occur for neutral polymers or at high ionic strength [247, 253]. The viscosity anomaly was qualitatively explained as due to intra- and inter-polyelectrolyte correlations [242, 243, 254]. In light of the recent fs-ESHS experiments, it would be interesting to investigate whether long-range electrostatic interactions between the charges and the H-bond network in polyelectrolyte aqueous solutions play a role in this viscosity anomaly. Traditional polyelectrolyte viscosity models are based on a mean-field approximation of the solvent and therefore do not explicitly take into account changes in solvent structure. Experimentally performing viscosity and fs-ESHS measurements will show whether a long-range interaction between the electrostatic field and the H-bond network of water is playing a role in the viscous flow of polyelectrolyte solutions.

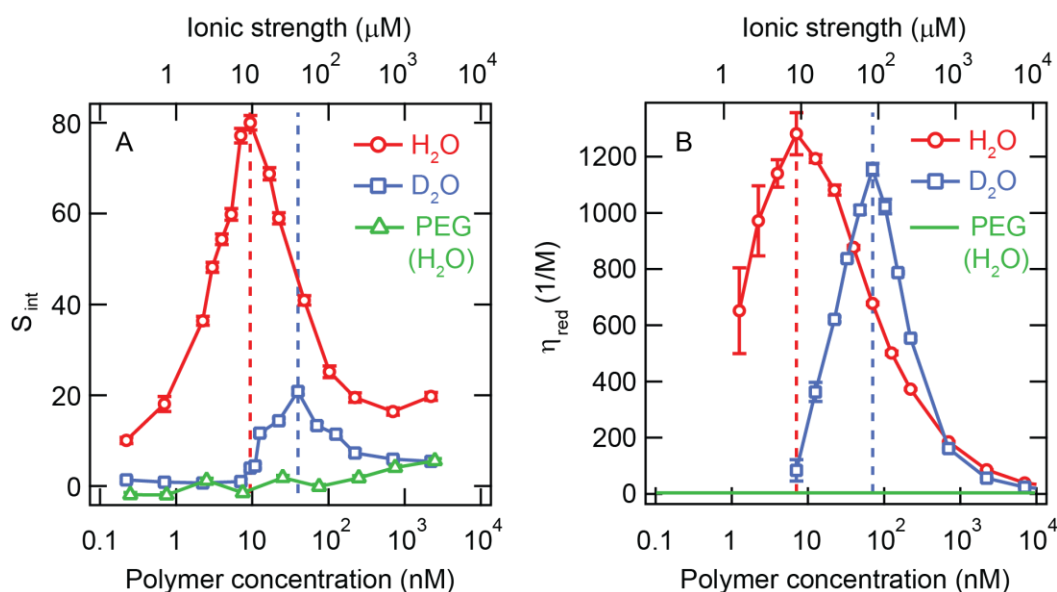


Figure 4.4: Polyelectrolytes induce strong orientational correlations leading to viscosity changes. (A) fs-ESHS intensities, relative to that of pure H₂O / D₂O, of PAA obtained by integrating the

fs-ESHS intensity in the angular range $-90^\circ > \theta > 90^\circ$. The dashed line indicates the peak concentration. The data for PEG in H₂O (green) serves as a comparison with a neutral polymer. The data was recorded with all beams polarized parallel to the horizontal scattering plane (ppp). (B) Reduced specific viscosity of PAA dissolved in H₂O and D₂O. The average molecular weight of PAA was 450 kDa, corresponding to a contour length of 1560 nm. The reduced specific viscosity of PEG was calculated using the Huggins equation [255] with details of the calculations shown in the appendix.

In what follows, we investigate the long-range correlations in aqueous polyelectrolyte solutions in more detail by measuring the integrated second harmonic intensity scattered in the forward half-plane (Figure 4.4A) and compare it with the reduced specific viscosity of the solutions (Figure 4.4B). In Figure 4.4A the measured integrated fs-ESHS intensity (S_{int}) is plotted as a function of polyelectrolyte concentration (bottom axis) and ionic strength (top axis) for PAA solutions in H₂O (red circles), D₂O (blue squares), and for poly(ethylene glycol) (PEG), a neutral polymer dissolved in H₂O (green triangles). The fs-ESHS data for PSS is shown in Figure 4.6A (appendix) and displays a similar trend as the PAA. The concentration dependence of S_{int} is comparable to the fixed-angle measurements of Figure 4.1D, but higher fs-ESHS intensities are recorded, allowing for a more accurate comparison. The fs-ESHS intensity increases up to a value of 80 times the scattered intensity of pure water up to a concentration of ~ 9 nM (ionic strength of ~ 10 μ M). The intensity drops with a further addition of PAA, leveling off at a concentration of 220 nM (ionic strength of 240 μ M). For D₂O solutions the behavior is also similar compared to Figure 4.1D, and shows a curve that is reduced in maximum intensity by a factor of ~ 4 , and shifted to $8\times$ higher concentrations. The results for PSS (Figure 4.6A, appendix) are qualitatively similar but display an even more pronounced difference between H₂O and D₂O: The fs-ESHS peak intensity is reduced from 80 to 8, and the peak polymer concentration is increased by a factor of 14. PEG, on the other hand (Figure 4.4A), shows no such behavior, underlining the importance of electrostatic interactions with water.

The reduced specific viscosity η_{red} as a function of polymer concentration is shown for PAA solutions in H₂O (red) and D₂O (blue) in Figure 4.4B. The data for the PSS polyelectrolyte is plotted in the same manner in Figure 4.6B in the appendix. As a comparison, the specific viscosity of neutral PEG polymer chains in H₂O is also displayed (green trace). The η_{red} of PEG solutions was theoretically calculated with details shown in Section 4.4.2 in the appendix. The specific viscosity of PAA and PSS shows a surprisingly similar behavior as the fs-ESHS data, starting at a low value and rising up to a maximum with increasing concentration. The viscosity maximum occurs at the same ionic strength as the fs-ESHS maximum (~ 10 μ M for H₂O) and comprises a difference of two orders of magnitude of η_{red} . The effect of D₂O on the viscosity is similar: The peak intensity is shifted to higher ionic strength for D₂O (~ 100 μ M),

and the peak value is reduced by ~20 %. For PSS (Figure 4.6B) the effect is even more pronounced: Switching from H₂O to D₂O, the peak concentration is shifted from 3.2 to 100 nM (ionic strength 2.8 μ M to 85 μ M), and the peak value of η_{red} is reduced by a factor of ~3.

The appearance of a peak in η_{red} as a function of polyelectrolyte concentration is in qualitative agreement with previously measured data for both PAA [256] and PSS [242, 257] in H₂O. To the best of our knowledge, the D₂O measurements have not been reported before, and are remarkably different from H₂O, in that the peak occurs at 10 \times higher concentration and with a smaller amplitude. The anomalous viscosity peak is known to rapidly disappear when excess salt is added to the solution due to Debye screening [258], which is consistent with the sensitivity of the fs-ESHS response to added salt shown in Figure 4.3. This points to long-range electrostatics as the source for the observed behavior in both the molecular structural (fs-ESHS) measurement and the macroscopic (reduced viscosity) measurement. The neutral PEG (and other neutral polymers) does not display the viscosity anomaly [259, 260]. Likewise, there is no peak in the fs-ESHS response of PEG. This further confirms the importance of long-range electrostatic interactions in PAA (PSS) solutions which are responsible for the strong enhancement of the fs-ESHS response and the reduced viscosity and are absent for neutral polymers such as PEG.

The behavior observed in Figure 4.4 is interesting for the following reasons: First, the correlation between the fs-ESHS intensity and the reduced specific viscosity for both H₂O and D₂O and for both polyelectrolytes with different molecular weights and different chemical structures suggests that they derive (at least partially) from the same mechanism. Second, the isotope effect observed in the viscosity is unexpected. According to literature, the anomalous behavior of the specific viscosity of polyelectrolyte solutions stems solely from intra- and inter-polyelectrolyte correlations [242, 243, 248]. Models based on this assumption are in agreement with the experimental data in H₂O. However, since the models are based on a mean-field approximation of water, they do not predict a significant difference in η_{red} between H₂O and D₂O, as the dielectric constants of the two solvents differ by less than 0.4% [27]. Using one of the existing mean-field models [261], we calculated the reduced specific viscosity and plotted it together with the measured data for H₂O and D₂O. The data is presented in Figure 4.5. Although the model reproduces the anomaly for PAA in H₂O, it predicts nearly the same behavior for in D₂O. Yet, the measured η_{red} of PAA is significantly different for D₂O, indicating that the enhancement of water-water correlations plays an important role.

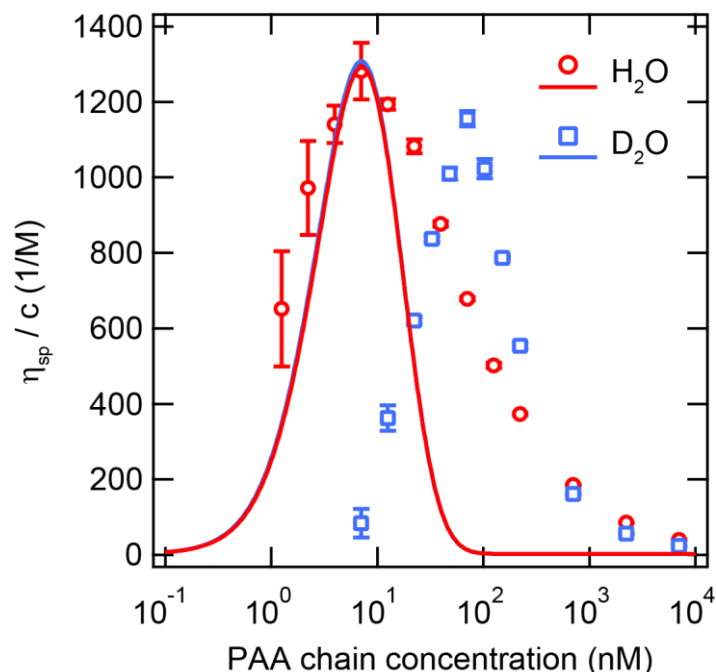


Figure 4.5: Comparison of the measured reduced viscosity of PAA with a theoretical model. Reduced specific viscosity of PAA as a function of PAA concentration in H₂O (red) and D₂O (blue). The markers are the measured data shown previously. The overlapping lines represent the curves that are predicted by the mean-field model for H₂O and D₂O. The details of the calculation are described in the appendix (Section 4.4.3).

As mentioned in the introduction, the fs-ESHS data for simple electrolyte solutions in Figure 4.1A, is different for H₂O and D₂O. This difference was assigned to nuclear quantum effects. H-bonds between water molecules can be broken along two different orthogonal axes. Figure 4.1B illustrates two H-bonded water molecules that are orientationally correlated, and the black arrows illustrate the two axes of motion, a stretching motion or a rotational motion. The stretching motion does not lead to differences in orientational correlations in contrast to the rotations, rendering fs-ESHS more sensitive to H-bond breaking via rotation. Since the H-bond bending mode is predicted to be stronger in D₂O than in H₂O [57, 239, 262], the fs-ESHS response of pure D₂O is larger than that of H₂O [41], as is its resistance to restructuring due to ions [41] or ionic groups on polyelectrolytes as is observed here. Since the fs-ESHS data and the specific viscosity data are similar, it is plausible that a similar decoupling effect also contributes to viscosity. Viscosity depends on the movement of molecules through water and this naturally involves the breaking of H-bonds [263]. Our combined data suggest that the breaking of H-bonds by rotation plays a relatively larger role in determining the viscosity than the breaking of H-bonds by stretching. Namely, if both modes would contribute equally, no viscosity difference between H₂O and D₂O solutions would be observed. If the stretching mode would contribute more the D₂O / H₂O difference would be reversed. Our observation and assessment are in agreement with spectroscopic measurements since the H-bond stretch

mode was detected at $\sim 183\text{ cm}^{-1}$, while the H-bond bending mode was found to occur at lower frequencies $\sim 50\text{ cm}^{-1}$ (for H_2O) [264, 265]. Although both values are below the thermal energy (219 cm^{-1}), the bending mode is energetically more favorable and therefore may contribute more than the stretching mode. Such a mechanism could also explain an isotope effect observed in adhesion hysteresis [266]. Thus, long-range interactions are present in more systems than simple electrolyte solutions and can lead to dramatic changes in macroscopic properties as well as unexpected significant nuclear quantum effects. As water plays an omnipresent role in diverse disciplines as physics, chemistry, biology, and medicine, the observed effects can have consequences for all processes where electrically charged molecules are involved.

4.3. Summary and Conclusions

We investigated long-range interactions between polyelectrolytes and the H-bond network of water. We found an increase in the orientational order of water and an even larger difference between H_2O and D_2O solutions compared to simple electrolyte solutions. Upon increasing the polyelectrolyte concentration the fs-ESHS intensity increases, up to a maximum and then reduces and levels off. Qualitatively this behavior can be explained by two parallel effects: increasing polyelectrolyte number density and screening of the electrostatic field by counterions. Macroscopically, we observed similar behavior for the reduced viscosity. The reduced viscosity changes up to two orders of magnitude with increasing concentration, shifts by a factor of $\sim 8\text{-}14$ in the concentration and decreases in maximum value (20-300 %) when D_2O is used instead of H_2O . Traditional mean-field models cannot explain such a difference. We conclude that the anomalous viscosity of polyelectrolyte solutions cannot be entirely explained by intra- and inter-polyelectrolyte correlations but that changes in water-water orientational correlations influence the reduced viscosity as well. Moreover, our data suggest that H-bond breaking through rotations occurs more readily than through H-bond stretching and is more important for viscous flow.

4.4. Appendix

4.4.1. fs-ESHS and reduced viscosity of poly(styrene sulfonate)

Figure 4.6 shows the fs-ESHS measurements for PSS for both H_2O and D_2O (purple and green data in panel A), as well as the reduced viscosity measurements for PSS in H_2O and D_2O (purple and green data in panel B).

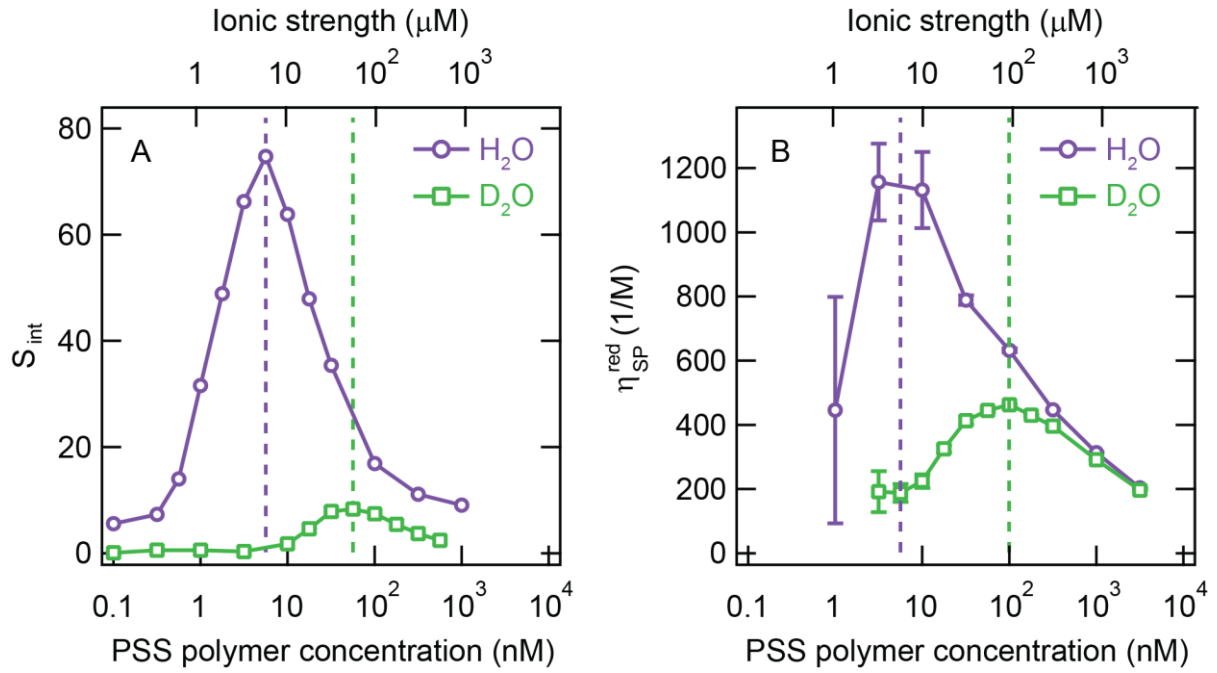


Figure 4.6: Polyelectrolytes induce strong orientational correlations leading to viscosity changes. (A) fs-ESHS intensities, relative to that of pure H₂O / D₂O, of PSS obtained by integrating the fs-ESHS intensity in the angular range $-90^\circ < \theta < +90^\circ$. The dashed line indicates the peak concentration. The data was recorded with all beams polarized parallel to the horizontal scattering plane (ppp). (B) Reduced specific viscosity of PSS dissolved in H₂O and D₂O. The average molecular weight of the PSS used was 1000 kDa.

4.4.2. Calculation of the reduced specific viscosity of PEG

The concentration dependence of reduced viscosity of dilute PEG shown in Figure 4.4B in the main text was calculated from the Huggins equation [255]: $\eta_{red} = [\eta] + k_\eta [\eta]^2 c$ where $[\eta] = 4.4 \cdot 10^{-5}$ L/g is the intrinsic viscosity and $k_\eta = 0.322$ L/g is the Huggins coefficient of PEG (values taken from Ref. [260]).

4.4.3. Modeling the reduced specific viscosity of PAA

The curve of the reduced specific viscosity of polyelectrolytes can be qualitatively reproduced by several mean-field models with varying accuracy and computational difficulty. As an example, we will calculate the reduced viscosity of PAA (mol. wt. 450 000 Da) using a spherically symmetric model based on the Rice-Kirkwood theory [261]. Although this model is not the most accurate representation of the polyelectrolyte geometry, it provides an analytical solution. According to this theory, the contribution of electric charges to the reduced specific viscosity is given by the following equation [254, 261]:

$$\eta_{red} \approx c^2 \int_{r_0}^{\infty} r^2 \left(\frac{\partial^2 u(r)}{\partial r^2} + \frac{4}{r} \frac{\partial u(r)}{\partial r} \right) 4\pi r^2 g(r) dr \quad (4.4)$$

The electrostatic potential $u(r)$ is given by:

$$u(r) = \frac{(ze)^2}{4\pi\epsilon_0\epsilon r} e^{-\kappa r} \quad (4.5)$$

where $z = 1$ is the ion valence. The radial distribution function $g(r)$ is given by:

$$g(r) = e^{-u(r)/k_B T} \quad (4.6)$$

where k_B is the Boltzmann constant and T is the temperature. For $u(r) \ll k_B T$ we can make the approximation $g(r) \approx 1 - u(r)/k_B T$. By solving the above integral, we obtain the following expression for the reduced specific viscosity [254]:

$$\eta_{red} \approx c^2 \left[z^2 \lambda_B (r_0^2 + r_0^3 \kappa) e^{-\kappa r_0} + z^4 \lambda_B^2 \left(-\frac{1}{2} r_0^2 \kappa + \frac{1}{2} r_0 + \frac{5}{4} \kappa^{-1} \right) e^{-2\kappa r_0} \right] \quad (4.7)$$

The lower integration bound $r_0 = 528$ nm is chosen arbitrarily to align the peak position of the model curve with the measured H₂O data. The vertical scale of the model is adjusted to match the measured data as well. To calculate the H₂O (D₂O) curve we used the relative permittivity $\epsilon = 78.7854$ (78.2618) [27] and the self-ionization constant $pK_w = 13.997$ (14.869). The comparison of the model against experimental data is shown in Figure 4.5.

The model predicts a virtually identical curve for H₂O and D₂O which is not surprising since the dielectric constants of the two solvents differ by less than 0.4 %. We can also see that the shape of the predicted curve does not accurately follow the experimental data. This could be improved by using a more sophisticated model, such as a skewed rod model, and by including polyelectrolyte chain expansion [243]. However, such models are still mean-field approximations that approximate water with a single dielectric constant and neglect collective H-bonding. They would, therefore, still not predict a significant difference between H₂O and D₂O.

Chapter 5: Membrane–Protein–Hydration Interaction of α -Synuclein with Anionic Vesicles Probed via Angle-Resolved Second-Harmonic Scattering

Amyloid formation of the protein α -synuclein promotes neurodegeneration in Parkinson's disease. The normal function of α -synuclein includes synaptic vesicle transport and fusion, and the protein binds strongly to negatively charged vesicles in-vitro. Here we demonstrate that non-resonant angle-resolved second harmonic scattering detects α -synuclein binding to liposomes through changes in water orientational correlations and can thus be used as high accuracy and high throughput label-free probe of protein-liposome interactions. The obtained results suggest a binding model in which the N-terminus of α -synuclein adopts an α -helical conformation that lies flat on the vesicle surface while the negatively-charged C-terminus remains in solution.

This chapter is based on the article by Jan Dedic, Sandra Rocha, Halil I. Okur, Pernilla Wittung-Stafshede and Sylvie Roke entitled “Membrane–Protein–Hydration Interaction of α -Synuclein with Anionic Vesicles Probed via Angle-Resolved Second-Harmonic Scattering” published in the Journal of Physical Chemistry B, 2019, 123 (5), p. 1044-1049

5.1. Introduction

The protein alpha-synuclein (α S) is a major component of amyloid aggregates found in Lewy body inclusions, which are the pathological hallmark of Parkinson's disease (PD), the second most common neurological disorder after Alzheimer's [267]. The assembly process of the 140-residue protein α S into amyloid fibrils, via oligomeric intermediates, has been linked to the molecular basis of PD [268, 269]. The exact function of α S is unknown, but it is suggested that the protein is involved in synaptic vesicle release and trafficking, regulation of enzymes and transporters, and control of the neuronal apoptotic response [270, 271]. α S is present at presynaptic nerve terminals [272-274] and it is reported that the protein exists *in vivo* in both free cytosolic and membrane-bound states [275]. PD pathology may be associated with change or disruption of α S-lipid interactions, and *in vitro* studies have indicated that early-onset PD mutations can affect the binding of α S to phospholipids [276].

The monomeric α S form in solution has a disordered structure, whereas the membrane-bound state has a chiral α -helical structure [274, 277-279]. The N-terminus was shown to be responsible for membrane association and α -helix formation upon binding to lipid bilayers, whereas the C-terminal is unstructured and extends out from the bilayer [274, 278, 280-283]. Although there exists a significant body of work on α S-lipid interactions, such as detailed solid-state NMR [278, 279], CD and calorimetric studies [284, 285], it has proven difficult to characterize the membrane-bound state of α S in liquid water at standard conditions and to probe the interaction with the membrane's interfacial aqueous environment in a surface-specific manner. Using high-resolution solution NMR it was proposed that the first two-thirds of the α S polypeptide adopt two helical regions (both with $\alpha_{11/3}$ conformation) with a short linker between them when bound to SDS micelle surfaces [286]. In this slightly unwound helical model, a set of Lys residues forms a boundary between hydrophobic and hydrophilic faces on both sides of the helix. A subsequent NMR structure gave clear evidence of a broken helix when α S bound to SDS micelles, but the helical conformation of α S appeared more ideal in this study [287]. Micelles are small membrane mimics and thereby highly curved; it is unclear what happens when α S is bound to a more realistic membrane model [288]. For example, the $\alpha_{11/3}$ helical model for α S was supported by site-specific spin-label continuous wave EPR measurements using another membrane mimic but, instead of a broken helix, an extended one was observed [289]. To better understand the complex mechanism of membrane – protein interaction, label-free interface-specific methods with molecular sensitivity would help greatly. In addition, information about the structure of the aqueous phase in realistic membrane systems is currently unavailable. Second-order nonlinear optical techniques such as sum-frequency and second harmonic generation are useful as they are intrinsically surface-specific [73, 114, 125, 144, 290-294] and can interrogate the molecular structure of interfacial water

[79, 115, 295, 296]. Sum frequency measurements of DNA [121] and artificial pores [122] show that chiral macromolecular protein structures can be passed on to the adjacent aqueous phase underlining the important role water plays in protein-surface interactions. Second-harmonic scattering can be performed on liposomes in aqueous solutions where it probes interfacial water molecules[128]. The reason for why the SHS signal is dominated by interfacial water molecules, and not the lipids that form the liposomes themselves, is the following: a non-resonant SHS experiment reports on all dipolar molecules that are not centrosymmetrically distributed, and each dipolar molecule has a response that is of the same order of magnitude [102]. The non-centrosymmetric distribution of dipolar molecules arises from chemical interactions at the interface (quantified by the second-order surface susceptibility tensor $\chi_s^{(2)}$) and the interaction with the interfacial electrostatic field (quantified by the surface potential Φ_0). At an aqueous interface, the most abundant dipolar species by far is water (30 H₂O molecules per nm³), even in the interfacial double layer region, where the orientational distribution of dipolar molecules is changed by the surface electrostatic field. Moreover, the measured SH intensity scales quadratically with the surface density of correlated dipolar species[125], further increasing the contribution of water molecules. For this reason, liposomes in aqueous solutions exhibit an SHS response that arises predominantly from the reorientation of water at the liposome surface [69, 76, 82, 115, 137]. Using polarimetric angle-resolved SHS (AR-SHS) [76, 172] in combination with nonlinear optical models [137] allows one to quantify the orientation of the interfacial water with respect to the liposome radius, as well as the surface potential (Φ_0). For the case of non-resonant elastic AR-SHS the second-order surface susceptibility tensor $\chi_s^{(2)}$ reduces to a single element: $\chi_{s,2}^{(2)} = \chi_{s,\theta'\theta'r'}^{(2)}$ which provides an indication of the orientational alignment of water along the interfacial normal. More detailed information about the model and its assumptions can be found in Chapter 2 or in the literature [69, 76]. In addition, chiral structures such as α -helices would give rise to additional (chiral) components of $\chi_s^{(2)}$ that can be probed separately using different polarization states of the incoming and outgoing light [160, 168].

Here, we use electrokinetic mobility measurements and polarimetric AR-SHS to characterize the interaction of α S with 1,2-dioleoyl-*sn*-glycero-3-phospho-(1'-*rac*-glycerol) (DOPG, structure shown in Figure 5.1A) liposomes and their aqueous environment. We find that the non-chiral AR-SHS patterns are modified by the α S-liposome interfacial-region interaction, while the electrokinetic mobility of the liposomes is unaffected by α S binding. Scattering patterns geared at sensing chirality, do not show evidence of it. This combined effect can be explained in terms of a reorientation of water near the interface, which can occur when α S binds only with the α -helix lying flat on the liposome while the negatively-charged part of the protein remains in the solution as a consequence of electrostatic repulsive interactions.

5.2. Experimental section

5.2.1. Chemicals

DOPG (1,2-dioleoyl-*sn*-glycero-3-phospho-(1'-*rac*-glycerol) sodium salt in chloroform solution, Avanti Polar Lipids) – structure shown in Figure 5.1A, sodium hydroxide (99.99%, Sigma), and sodium chloride ($\geq 99.999\%$, Acros) were used as received. The stock NaCl solution was filtered through a 0.1 μm pore PVDF membrane (Merck Millipore Ltd). Water used (H_2O) was double distilled (resistivity 18.2 $\text{M}\Omega\cdot\text{cm}$, Milli-Q UF-Plus, Millipore Inc).

5.2.2. Protein expression and purification

Wild type α -synuclein was prepared by transforming the construct into BL21 (DE3) (Novagen) cells. The construct carries the gene for α -synuclein in tandem with the gene for the 434 repressor protein with an N-terminal His-tag and a caspase 7 cleavage. Cells were grown to an OD_{600} of 0.6 in LB broth containing 100 $\mu\text{g}/\text{ml}$ carbenicillin at 37 °C and then induced with 1 mM isopropyl β -D-1-thiogalactopyranoside (IPTG) and grown overnight at 25 °C post-induction.

The cells were centrifuged for 30 min at 15000 g, and the pellet re-suspended in 8 M urea, 20 mM Tris, 20 mM imidazole, pH 8.0, sonicated on ice using a probe sonicator in pulse mode, in the presence of protease inhibitor cocktail (Roche), followed by centrifugation at 20000 rpm for 30 mins. The supernatant was filtered through 0.2-micron filter and loaded on an affinity column (Ni Sepharose 6 Fast Flow, GE Healthcare), equilibrated with 20 mM Tris, 50 mM NaCl, 20 mM imidazole, 5% glycerol, pH 7.5. Elution was carried out with the same buffer containing 250 mM imidazole. For removal of the His-tag, the peptidase caspase 7 was added in a ratio of 1:100 (w/w) and was incubated further overnight at 4°C. Cleavage efficiency was verified with SDS-PAGE. The sample was then loaded on an anion-exchange column (HiTrap Q FF, GE Healthcare) equilibrated with 20 mM Tris pH 8.0 and eluted with a linear NaCl gradient of 20 mM Tris, 1 M NaCl, pH 8.0. Finally, the sample was run through a gel filtration column (HiLoad 16/60 Superdex 75, GE Healthcare), equilibrated with 50 mM ammonium carbonate. The protein was stored in a lyophilized form at -80 °C.

5.2.3. Sample preparation

α -Synuclein (1 mg) was first dissolved in 20 μL of 54 mM NaOH and then ultrapure water was added to obtain a concentration of αS monomer of approximately 60 μM . The sample was filtered through syringe filters with a pore size of 0.2 μm . The pH of the protein solution was 7.2, the conductivity was 112 $\mu\text{S}/\text{cm}$ and the final concentration was determined

spectrophotometrically using a molar extinction coefficient of $5960 \text{ M}^{-1} \text{ cm}^{-1}$ at 280 nm. DOPG lipid vesicles were prepared by the lipid film hydration method. Suitable volumes of DOPG chloroform solution were transferred to a round bottom flask and the solvent was removed by rotary evaporation. The lipid film was then dried under vacuum for at least 3 hours and hydrated in ultrapure water. The resulting multilamellar vesicle suspensions were extruded through polycarbonate filters with a pore diameter of 100 nm using a Mini extruder (Avanti Polar Lipids). The size of the resulting liposomes was determined by dynamic light scattering (DLS) using a ZetaSizer Nano ZS instrument (Malvern Instruments Ltd., UK). The concentration of the lipids in the sample was 0.26 mg lipids/mL weight ratio for DLS, ζ -potential measurements, and second harmonic scattering (SHS) experiments. A control α S-free sample based on a common stock of DOPG liposomes was prepared as well. The conductivity of the control was adjusted with NaCl to match that of α S-DOPG.

Liposome number density after extrusion (1.215×10^{12} liposomes/mL) was calculated assuming area per lipid of 0.7 nm^2 [297] and a 10% loss of lipids during extrusion. The ionic strengths of the solutions $I(\text{DOPG}) = 310 \text{ }\mu\text{M}$ and $I(\alpha\text{S-DOPG}) = 493 \text{ }\mu\text{M}$ were calculated based on molar conductivities of the solutions [298]. The size distribution was determined from 5 DLS measurements whose results were averaged. The error represents the standard deviation of the mean. The Z-average radius of pure DOPG liposomes is $128.3 \pm 0.9 \text{ nm}$ with a PDI of 0.061 ± 0.012 . For α S-DOPG, the Z-average size is $123.2 \pm 1.0 \text{ nm}$ and the PDI is 0.185 ± 0.010 . The size distribution becomes broader on α S binding, possibly because the hydrodynamics of the liposomes are affected by protein binding. However, the size distribution remains monomodal as can be seen in Figure 5.1B.

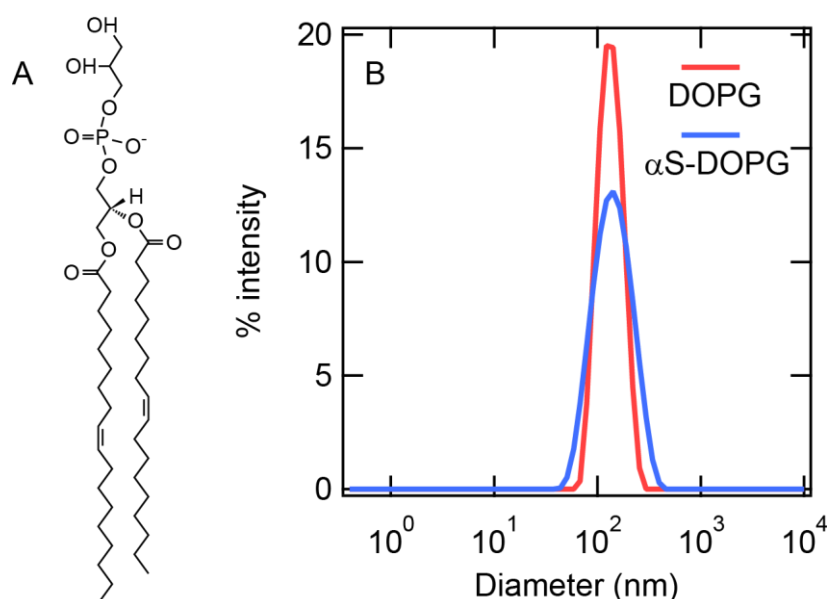


Figure 5.1: The lipids and liposomes used in this study. (A) Molecular structure of the lipid DOPG used in the model of lipid membranes. (B) The intensity-weighted size distribution of the liposome

samples used in the AR-SHS experiments obtained from dynamic light scattering. The size distribution broadens slightly as a result of α S binding but remains monomodal.

5.2.4. AR-SHS measurements

Angle-resolved second harmonic scattering (AR-SHS) measurements were performed using a previously described optical system [172]. Scattering patterns were obtained by measuring SHS intensity at 5-degree intervals between -90° and $+90^\circ$ relative to the forward direction. The average incident laser power was 60 mW. At each angle, 20 exposures with 1 s integration time were taken and averaged. The normalized SHS intensity at angle θ was calculated as $S(\theta) = \left(I_{sample}^{(OI)}(\theta) - I_{solvent}^{(OI)}(\theta) \right) / I_{HRS}^{(SSS)}(\theta)$ where $I_{sample}^{(OI)}$ and $I_{solvent}^{(OI)}$ are the average SHS intensities of the sample and the solvent, respectively. O (I) stand for the polarization state of the outgoing (incident) light relative to the scattering plane (p-parallel or s-perpendicular). To make sure that the results obtained from AR-SHS experiments are consistent we prepared and measured the α S-DOPG samples three times. The unprocessed SHS patterns of all three samples are nearly identical as can be seen in Figure 5.2.

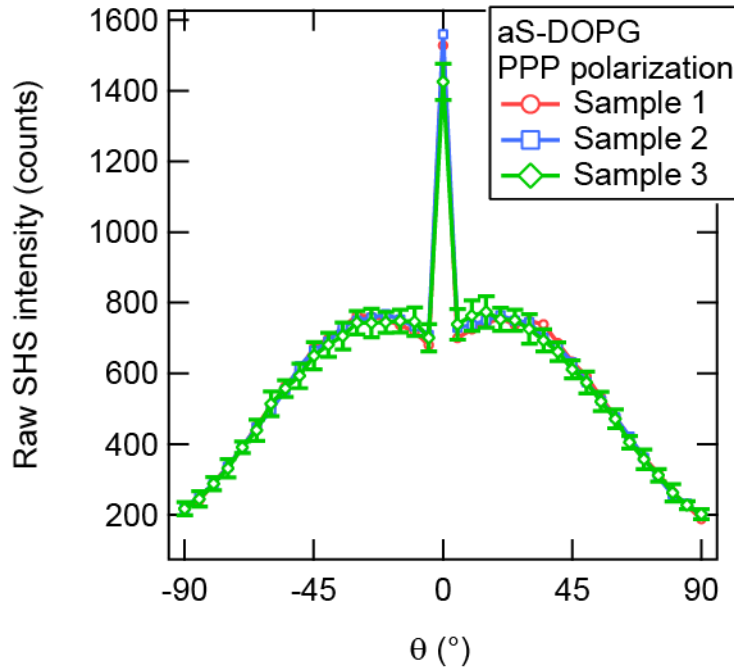


Figure 5.2: Reproducibility of the SHS measurements. Unprocessed SHS patterns in ppp polarization combination of three α S-DOPG samples showing good reproducibility of the scattering patterns.

5.2.5. Fitting the AR-SHS patterns

To obtain values of the second-order surface susceptibility ($\chi_{s,2}^{(2)}$) and the surface potential (Φ_0), the normalized SHS patterns in ppp and pss polarization combinations were fitted using the following set of equations [76]:

$$\begin{aligned} S(\theta)_{ppp} &= \frac{E_p^4(\omega)}{\langle \bar{\mu}^2 \rangle} \frac{N_p}{N_b} \left| \cos\left(\frac{\theta}{2}\right)^3 \Gamma_1^{(2)} \cos\left(\frac{\theta}{2}\right) \left(\Gamma_2^{(2)} + \Gamma_2^{(3)'} \right) (2 \cos(\theta) + 1) \right|^2 \\ S(\theta)_{pss} &= \frac{E_s^4(\omega)}{\langle \bar{\mu}^2 \rangle} \frac{N_p}{\langle \bar{\mu}^2 \rangle N_b} \left| \cos\left(\frac{\theta}{2}\right) \left(\Gamma_2^{(2)} + \Gamma_2^{(3)'} \right) \right|^2 \end{aligned} \quad (5.1)$$

Where $\bar{\mu} = \bar{\beta}_{H_2O}^{(2)} E(\omega)^2$ is the average induced dipole moment of a water molecule and N_p is the number density of liposomes (discussed above). The effective susceptibility elements are given by [164]:

$$\begin{aligned} \Gamma_1^{(2)} &= (2F_1 - 5F_2) \chi_{s,1}^{(2)} \\ \Gamma_2^{(2)} &= F_2 \chi_{s,1}^{(2)} + 2F_1 \chi_{s,2}^{(2)} \\ \Gamma_2^{(3)} &= F_2 \chi_2^{(3)'} \Phi_0 (F_1 + F_3) \\ \chi_2^{(3)'} &= \frac{N_b}{\epsilon_0} \left(\bar{\beta}_{H_2O}^{(3)} + \frac{\bar{\beta}_{H_2O}^{(2)} \mu_{dc}}{3k_B T} \right) \end{aligned} \quad (5.2)$$

Where F_1 , F_2 , and F_3 are the scattering form-factors defined in Chapter 2 and in Refs. [76, 137]. To fit the AR-SHS patterns, we used the constants listed in Table 5.1. We assume that the distribution of the water tilt angles at the interface is broad which simplifies the above equations as $\chi_{s,1}^{(2)} \rightarrow 0$ [299-301]. Lastly, the susceptibility elements are corrected for discontinuity of the electric field at the liposome-water interface via the Fresnel factors [137, 214]:

$$\begin{aligned} \chi_{s,2}^{(2)} &\rightarrow \frac{27\eta}{(2+\eta)^3} \chi_{s,2}^{(2)} \\ \chi_2^{(3)} &\rightarrow \frac{27\eta}{(2+\eta)^3} \chi_3^{(2)} \\ \eta &= (n_{lip}/n_{H_2O})^2 \end{aligned} \quad (5.3)$$

Additional information about the assumptions of the SHS model can be found in Chapter 2 of this thesis and in Refs. [69, 76, 137], including the supplementary material.

Table 5.1: List of constants used in the fitting procedure of AR-SHS patterns.

Constant	Value	Unit
Refractive index of water n_{H_2O}	1.33	-
Refractive index of liposomes n_{lip} [302]	1.4	-
Dipole moment of water μ_{dc} [303]	$8.97 \cdot 10^{-30}$	C m
Average 2 nd order hyperpolarizability of water $\bar{\beta}_{H_2O}^{(2)}$ [303]	$3.09 \cdot 10^{-52}$	C ³ m ³ J ⁻²
Average 3 rd order hyperpolarizability of water $\bar{\beta}_{H_2O}^{(3)}$ [303]	$4.86 \cdot 10^{-62}$	C ⁴ m ⁴ J ⁻³
2 nd order surface susceptibility element $\chi_{s,1}^{(2)}$ [299-301]	0	m ² V ⁻¹
Effective 3 rd order susceptibility element $\chi_2^{(3)'} [164]$	$1.03 \cdot 10^{-22}$	m ² V ⁻²
Number density of water N_b	$3.34 \cdot 10^{28}$	m ⁻³
Number density of liposomes N_p	$1.215 \cdot 10^{12}$	lip mL ⁻¹

5.3. Results and Discussion

α S is known to bind to negatively-charged DOPG liposomes with a stoichiometry of approximately 20 lipids per protein and, approximately 100 of the 140 residues adopt a helical conformation based on earlier far-UV CD experiments [277]. At the α S concentration used (with 11.6 lipid/ α S ratio), the membrane surface is fully covered. Using these conditions, we measured AR-SHS patterns of DOPG liposomes alone (DOPG) and DOPG liposomes mixed with α S (α S-DOPG) under pH-neutral conditions. Figure 5.3A, and Figure 5.3B show the AR-SHS patterns of the two systems together with ζ -potential measurements (Figure 5.3C) and extracted $\chi_{s,2}^{(2)}$ values (Figure 5.3D).

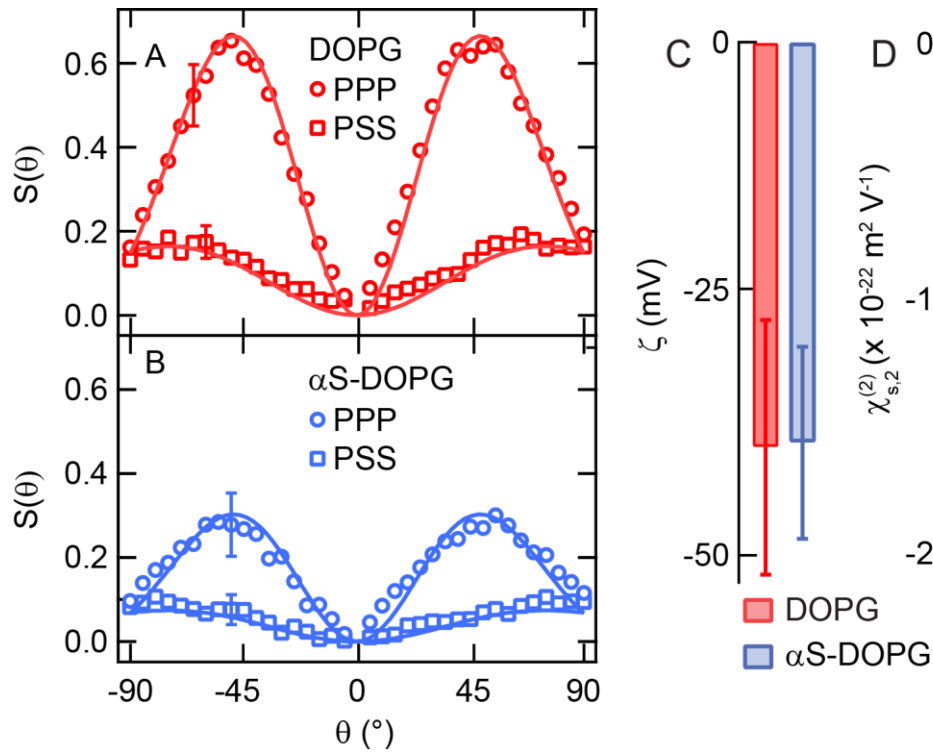


Figure 5.3: SHS and electrophoretic mobility measurements of DOPG and α S-DOPG. (A) AR-SHS pattern of DOPG in PPP (red circles) and PSS (squares) polarization combination. (B) AR-SHS pattern of α S-DOPG in PPP (blue circles) and PSS (squares) polarization combination. Solid lines represent the fit using the AR-SHS formalism. (C) Measured ζ -potential of the DOPG and α S-DOPG samples. (d) Second-order surface susceptibility of the DOPG and α S-DOPG samples obtained from fitting of the AR-SHS patterns.

These patterns were measured with varying states of polarization of the incoming and outgoing light. Here, p (s) refers to light polarized parallel (perpendicular) to the scattering plane and the three-letter codes are ordered according to the polarization states of each participating photon: (SH, fundamental, fundamental). As stated in the introduction, a major advantage of AR-SHS is its surface specificity which means that non-bound α S molecules do not contribute significantly to the SHS response. Although the hydration shells of freely dissolved α S may break the centrosymmetry of bulk water, and thus satisfy the condition for second-harmonic generation, their contribution to the SHS response is insignificant compared to liposomes due to their small size. This is because the SHS intensity scales with the sixth power of the particle's size but only linearly with bulk concentration [172, 304]. If we assume that freely dissolved α S is a particle with an effective diameter of 5 nm [305, 306] (approx. 1/24 of the liposome diameter), its contribution to the signal will be nearly $2 \cdot 10^8$ times less than that of a liposome. Our samples contain approx. 9300 α S molecules per liposome. Even if all of the α S molecules were freely dissolved in the bulk, their overall contribution to the AR-SHS

intensity would still be $2 \cdot 10^4$ times less than that of the liposomes. The SHS patterns can be described with an AR-SHS formalism that depends on two parameters: $\chi_{s,2}^{(2)}$ and Φ_0 . AR-SHS patterns of the DOPG liposome solution were fitted using a formalism described previously [69, 76]. A global fit of the patterns in ppp and pss polarizations (solid lines in Figure 5.3A) yields unique values of the second-order surface susceptibility ($\chi_{s,2}^{(2)} = -1.82 \pm 0.25 \times 10^{-22} \text{ m}^2 \text{ V}^{-1}$) and the surface potential ($\Phi_0 = -40.0 \pm 15.0 \text{ mV}$). The electrokinetic mobility measurement of the same sample gave a value of $-39.5 \pm 12.4 \text{ mV}$ for the ζ -potential. That the ζ -potential and the surface potential are nearly identical suggests that the slipping plane is very close to the surface. It is possible that a distinct (Stern) layer of condensed charges that one would normally expect to be present at highly charged interfaces is virtually absent.

Turning now to the α S-DOPG system, we find ζ -potential values of $-39.0 \pm 9.4 \text{ mV}$. This suggests, somewhat surprisingly, that even though the CD data [277] shows the surface coverage is high, the binding of α S does not seem to influence the net charge contained within the slipping plane. Upon the interaction with proteins, two things can happen: the ζ -potential can change, and the charge within the slip plane is changed, or the ζ -potential does not change, and the charge within the slip plane does not change. Either of these outcomes can be accompanied by a change in the position of the slip plane. With the α S positioned in close proximity to the surface, the electrokinetic mobility will report on the charge contained within the slip plane of both objects as they move together. Previous studies have shown clear adsorption of α S on the PG liposomes [277]. We, therefore, expect that the slip plane will now contain both the protein and the lipid, and within this surface, the net amount of electrostatic charge is the same as for the DOPG liposomes. Since the protein has charged residues, there has to be a partial cancelation of charge for the ζ -potential to remain unchanged.

Comparing the AR-SHS response without α S (Figure 5.3A) and with α S (Figure 5.3B), we also observe that the SHS intensity drops by 47 % upon the addition of α S. The decrease in SHS intensity can be accounted for by changes in $\chi_{s,2}^{(2)}$ or Φ_0 . Since the fitting routine takes in two variable parameters: $\chi_{s,2}^{(2)}$ and Φ_0 , there are three ways by which the data can be fitted: 1) leave $\chi_{s,2}^{(2)}$ and Φ_0 free, 2) fix $\chi_{s,2}^{(2)}$ and leave Φ_0 free, or 3) leave $\chi_{s,2}^{(2)}$ free and fix Φ_0 . Furthermore, the output of the AR-SHS model is constrained by physical feasibility and consistency of the results with other measurements and with reasonable expectations that derive from mean-field models such as the absence of charge inversion with the electric double layer. Fitting according to scenario 1 generates a negative value for $\chi_{s,2}^{(2)}$ ($-3.39 \times 10^{-22} \text{ m}^2 \text{ V}^{-1}$) and a positive value of Φ_0 ($+96 \text{ mV}$). Fitting according to scenario 2 generates an increase of Φ_0 to -0.04 mV . If we follow scenario 3 we obtain $\chi_{s,2}^{(2)} = -1.26 \pm 0.02 \times 10^{-22} \text{ m}^2 \text{ V}^{-1}$, a reduction

of $\chi_{s,2}^{(2)}$ by 30 %. In the first and second scenarios the fitted value of Φ_0 is larger than the ζ -potential, and requires a charge inversion to take place in the electric double layer. This contrasts with predictions by any mean-field theory of the electrical double layer[175]. Thus, the physically meaningful result here is that a 30% decrease in the $\chi_{s,2}^{(2)}$ magnitude occurs compared to pure DOPG (Figure 5.3D), representing a 30% loss in water directionality.

Biomolecules have been shown to imprint their chirality into the surrounding water [121, 122] and it is therefore interesting to determine if this is the case here as well. Figure 5.4A presents the chiral response of the aqueous environment obtained by measuring the scattering pattern using the spp polarization combination, which probes chiral elements of the second-order susceptibility tensor [160]. Here, one would expect a strong response of the chiral units if they have a non-zero projection in the direction of the surface normal (assuming they are isotropically distributed). As can be seen from Figure 5.4A, no detectable SH intensity was found (purple diamonds). Combined with the knowledge that α S does bind to the membrane with a significant surface fraction, this means that the α -helix units are oriented in the surface plane of the liposome. Since the water ordering is decreased by the presence of α S on the membrane despite not having any changes in the surface potential we suggest that the negatively charged C-terminus is not actually attached to the surface but protrudes into the solution as illustrated in Figure 5.4B. This would also make sense from an electrostatics perspective since DOPG and the C-terminus are both of like charge and thus repel each other. Our conclusion that the C-terminus extends into the solution is consistent with findings in previous reports based on NMR [278, 279, 281] and neutron scattering [283] using free-floating lipid vesicles, and QCM-D measurements using supported lipid bilayers [282]. Having such a geometry leads to oppositely oriented hydration shells of water around the liposome and the C-terminus as illustrated in Figure 5.4C. The SH light emitted from oppositely oriented water interferes destructively, resulting in a smaller magnitude of $\chi_{s,2}^{(2)}$. Thus, we see that probing the water at the liposome aqueous α -synuclein interface provides valuable information, not only about the interaction of the membrane interface and the protein, but also about the balance of electrostatic interactions and the important role water plays in it. Similar measurements can be performed on a wide variety of liposomes or lipid droplet interface systems.

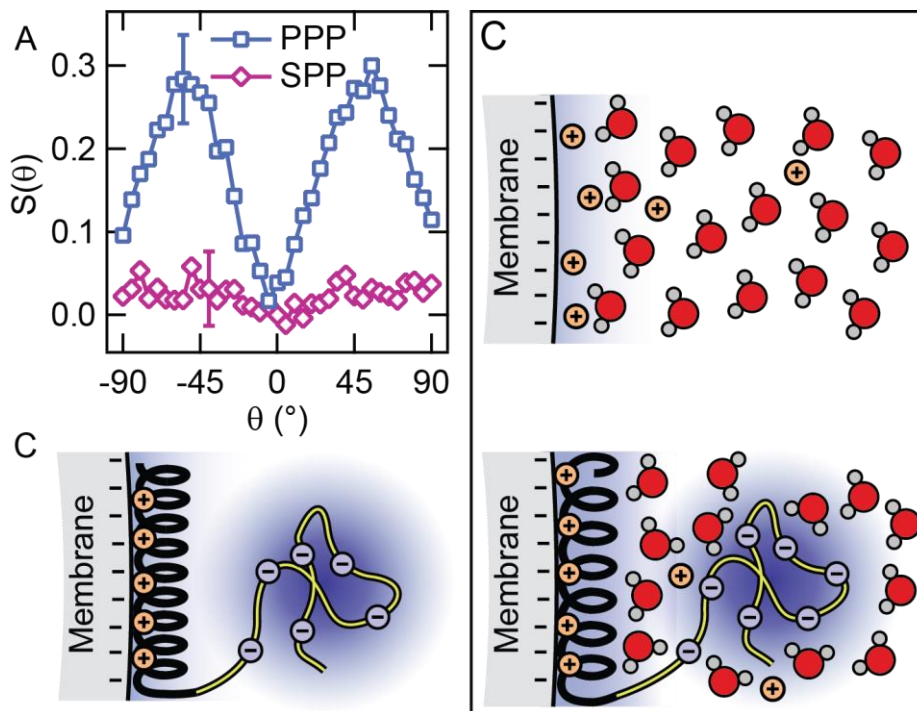


Figure 5.4: Chiral measurements and proposed structure of the α S-DOPG-water interface. (A) AR-SHS pattern of α S-DOPG acquired in a chiral polarization combination (SPP). An achiral response (ppp) is shown for comparison. (B) Structure of membrane-bound α S. The N-terminus region of α S that binds to the membrane is an α -helix. The C-terminus region (highlighted in yellow) is a random coil with a high negative charge. This creates a region of negative charge that is separated from the interface. (C) The structure of the interface around the outer leaflet of the DOPG membrane with and without α S. Top: in the absence of α S, the interfacial water molecules experience only the E-field originating from DOPG and the generated SH signals from the oriented water molecules add constructively. Bottom: the proposed binding model of α S to the DOPG membrane with the associated rearrangement of the water structure. The negatively-charged region of α S is highlighted. SH signal from water molecules reoriented by α S interferes destructively with the signal from other water molecules leading to a decrease in SHS intensity.

5.4. Conclusions

Polarimetric AR-SHS was used in combination with electrokinetic mobility measurements to investigate α S interaction with DOPG liposomes. Upon α S binding, no changes were found in electrokinetic mobility. We measured changes in the AR-SHS patterns and found an absence of chiral interfacial signals. The data is interpreted as follows: The α -helix binds parallel to the interface through electrostatic interactions while the negatively-charged C-terminus region of α S remains solubilized in the aqueous solution. The presence of two adjacent negatively charged interfaces (membrane and protein) leads to a reduction of average water orientation but retains the surface charge of the liposomes. This study demonstrates the potential of chiral and non-chiral AR-SHS to investigate α S-membrane interactions in-situ and label-free and highlights the amount of information can be obtained by measuring the hydration. Further

studies regarding this system could focus on the influence of charge and liposome substructure. For example, a positive charge would likely generate a different structure and the clustering of negative charge in lipid domains will also affect the binding behavior. Plaques are also expected to be clearly visible from the point of view that they should possess a sizeable chiral signature [86]. At the same time, this study heralds the possibility of investigation of the hydration – interaction of other membrane proteins with their native membranes, a field where much fundamental insight into the role of water is needed. Examples are ion channels, pore-forming proteins, and receptors.

Chapter 6: Self-assembly of cyclodextrin-lipid complexes probed by nonlinear scattering

Methyl- β -cyclodextrin (m β CD) is widely used to solubilize and encapsulate lipids and water-insoluble drugs by forming a host-guest complex. Using sum-frequency scattering on liposome dispersions in the presence of m β CD, we show that m β CD has a strong preference towards lipids with phosphatidylserine and phosphatidylglycerol headgroups over phosphatidylcholine and phosphatidic acid. This selectivity is explained by the presence of a larger number of H-bonding sites on certain headgroups. Analysis of angle-resolved second-harmonic scattering measurements shows that the m β CD-lipid complexes self-assemble into micron-long ordered fibers over the course of hours and days. Isotope exchange measurements indicate that the self-assembled structure is spanned by a large number of hydrating water molecules, suggesting that hydration plays a role in the self-assembly process and stabilization. Dynamic light scattering shows that the stability of the liposomes is not compromised throughout the process but does not detect the presence of the fibers due to the low sensitivity of the method. Our observations highlight the advantage of nonlinear scattering over traditional techniques for probing nanoscale molecular order.

6.1. Introduction

Cyclodextrins (CDs) are a class of cyclic oligosaccharides and are natural byproducts of the enzymatic digestion of starch [100]. The shape of the CDs resembles a truncated cone with a hydrophobic inner cavity and a hydrophilic exterior [307, 308]. This structure allows CDs to form water-soluble inclusion complexes with water-insoluble guest molecules such as lipids and various drugs [309-311]. These properties are exploited in pharmacology, cosmetics, foods, and basic research [96, 97, 307, 312-314]. Despite the widespread use of CDs, little is known about their interaction with lipids on the molecular level [98, 315, 316]. CD-lipid and CD-CD interactions have been studied extensively by calorimetry [317, 318], fluorescence [307, 319-321], electron spin resonance [307], plasmon resonance [316], light scattering [320, 322, 323], and microscopy [324]. Despite this, a unified picture of CD-lipid interaction does yet not exist. CDs are generally thought to interact more with the lipid acyl chains onto which they attach rather than the head groups [318, 320, 321, 325]. However, there is some evidence that CDs hydrogen (H)-bond to the phosphate [326, 327] or carboxyl groups [328-331]. Most studies on CD-lipid interaction were performed on phosphatidylcholine (PC) membranes [307, 316-318, 322, 325]. The few studies that have investigated the lipid selectivity of CD were not performed in a surface-specific manner or relied on labelled lipids [319, 320, 332, 333]. In addition to PC lipids, biological membranes contain also phosphatidylserine (PS), phosphatidic acid (PA), and phosphatidylglycerol (PG) [334, 335] which should also be investigated. Moreover, hydration is assumed to play a significant part in lipid self-assembly [59] and in CD-CD interactions [336, 337] but its role has not yet been experimentally investigated.

Here, we present a study on cyclodextrin-liposome interaction using nonlinear optical scattering techniques that are inherently sensitive to the breaking of centrosymmetry. This allows us to directly measure the molecular structure of interfaces and the formation of ordered structures [73, 74]. Sum-frequency scattering (SFS) probes vibrational modes of molecules in non-centrosymmetric arrangements [126]. Second-harmonic scattering (SHS) is a non-resonant technique that probes the orientational order of all molecules in the solution. The angular distribution of the SHS response contains information about the size, shape, and symmetry of the scattering objects.

The CD variant used here is methyl- β -cyclodextrin (m β CD, chemical structure, and shape shown in Figure 6.1A). It is composed of 7 D-glucose molecules linked by $\alpha(1-4)$ bonds. On average, 1.6 to 2 of the 3 hydroxyl groups of m β CD are methylated which significantly increases its solubility in water compared to the native β CD [100, 309]. Despite the high solubility of m β CD, we show that m β CD-lipid complexes are prone to self-assemble into ordered fibers. The self-assembly process shows strong head group specificity - PS and PG head groups interact favorably with m β CD while PC and PA do not, indicating that H-bonding

between m β CD and the head group is key. This effect is observed at an m β CD concentration as low as 1 mM, an order of magnitude below the concentration needed to solubilize the liposomes [320]. Unlike lipid extraction from membranes, the self-assembly follows slow kinetics (hours to days). An isotope exchange experiment indicates that the self-assembled fiber is enclosed in a hydrating shell of water, suggesting that hydration plays a major role in the self-assembly process. Complementary dynamic light scattering (DLS) and electrophoretic mobility measurements show no significant difference between bare liposomes and liposomes in the presence of m β CD, underlining the inherent sensitivity of nonlinear light scattering to the breaking of centrosymmetry which is not visible by linear light scattering.

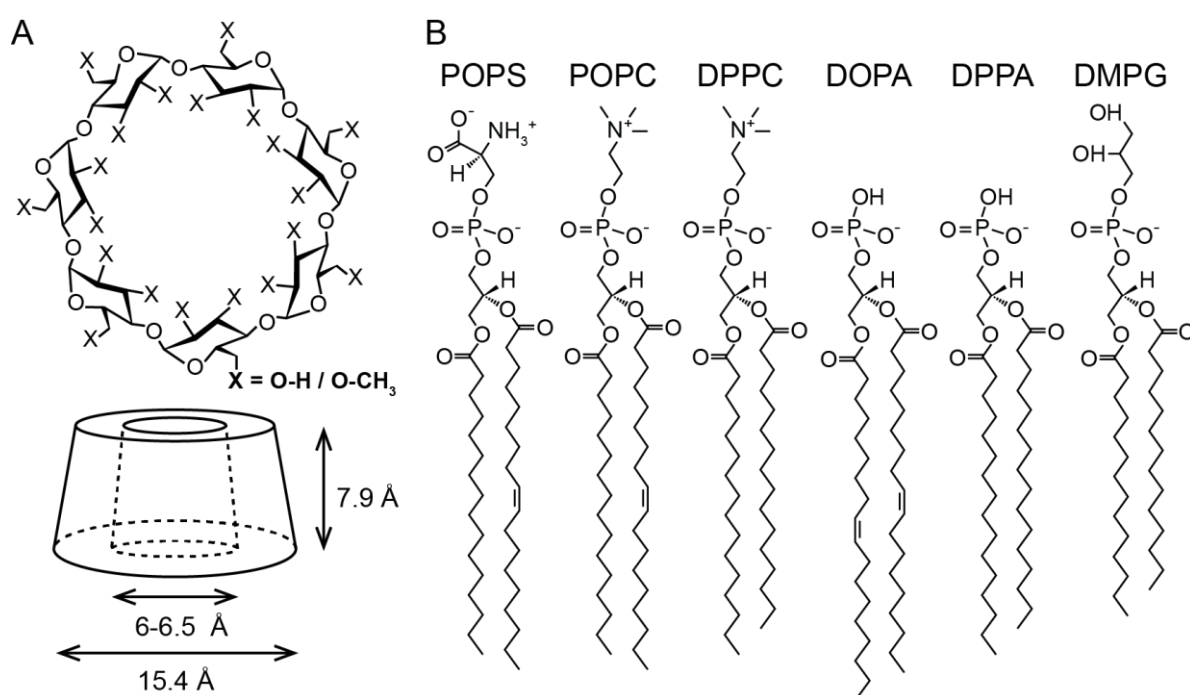


Figure 6.1: Molecular structures of m β CD and the lipids used in this work. (A) Top: structure of methyl- β -cyclodextrin (m β CD) - a 7-membered ring of glucose units with randomly methylated hydroxyl groups (X = O-H or O-CH₃). Bottom: the shape of m β CD resembles a tapered hollow cone with a hydrophobic inner cavity approx. 6 Å wide and 7.9 Å high [308, 338]. (B) The molecular structures of the 6 phospholipids used in this work.

6.2. Experimental section

6.2.1. Chemicals

Methyl- β -cyclodextrin (m β CD, $\geq 98\%$) produced by Wacker Chemie AG, Germany was used as received. The degree of methylation is 1.6-2.0 CH₃ per glucose unit. The molecular structure and shape of m β CD are shown in Figure 6.1A. The lipids 1-palmitoyl-2-oleoyl-sn-glycero-3-

phospho-L-serine (POPS), 1-palmitoyl-2-oleoyl-glycero-3-phosphocholine (POPC), 1,2-dipalmitoyl-sn-glycero-3-phosphocholine (DPPC), 1,2-dioleoyl-sn-glycero-3-phosphate (sodium salt) (DOPA), 1,2-dipalmitoyl-sn-glycero-3-phosphate (sodium salt) (DPPA), and 1,2-dimyristoyl-sn-glycero-3-phospho-(1'-rac-glycerol) (sodium salt) (DMPG) were purchased in powder form (>99 %) from Avanti Polar Lipids (Alabama, USA) and stored at -20 °C. The chemical structures of the lipids are shown in Figure 6.1B. Sodium Chloride (NaCl, 99.999 %) was purchased from abcr GmbH, Germany. Chloroform (CHCl₃) for analysis (Reag. Ph. Eur) was purchased from Merck, Germany. Heavy water (D₂O, 99.8 % D) with a resistivity of 2 MΩ·cm⁻¹ was purchased from Armar. Ultrapure H₂O with a resistivity of 18.2 MΩ·cm⁻¹ was obtained from a Milli-Q UF plus instrument (Millipore Inc.).

6.2.2. Sample preparation and measurements

The liposomes (small unilamellar vesicles - SUVs) were prepared by extrusion of rehydrated multilamellar vesicles according to the protocols described in [339, 340]. Briefly, a weighted amount of lipid powder was dissolved in CHCl₃ in a round-bottom glass container. A lipid film was formed on the glass surface by rotary evaporation of the solution under N₂ flow. The containers were placed in a vacuum for at least 2 hours to evaporate the remaining CHCl₃. The film was then rehydrated in D₂O with 25 mM NaCl. The dispersion was sonicated and vortexed. Liposomes were formed by extruding the dispersion 30-50× through a polycarbonate membrane with a pore size of 100 nm above the transition temperature of the lipid using a Miniextruder (Avanti Polar Lipids, Al, USA). The size distribution of the resulting liposomes was determined by dynamic light scattering (DLS) using a NanoSizer ZS (Malvern Ltd, UK). The liposome stocks were then stored in closed containers at 4 °C and used within a few weeks. The Z-average of the diameter of the extruded liposomes was in the range 100 – 130 nm, depending on the lipid with a polydispersity index (PDI) of < 0.1.

The liposome stocks were mixed with an mβCD solution in D₂O (25 mM NaCl) to obtain a final lipid concentration of 5 mg/mL and an mβCD concentration of 1 mM. Unless stated otherwise, the samples were stored in the dark and incubated in closed plastic containers at room temperature for ~24 hours. For SHS and DLS measurements the samples were diluted 10× with 25 mM NaCl in D₂O prior to the measurement for a final lipid concentration of 0.5 mg/mL. For SFS measurements the samples were used undiluted. The stability of the samples after incubation was verified by DLS before or after the SHS / SFS measurements. Each time 3 DLS measurements consisting of at least 10 runs were performed and their results were averaged.

Dry m β CD samples for reflection sum-frequency generation (SFG) measurements were prepared by evaporating a droplet of a concentrated aqueous m β CD solution (without salt) on piranha-cleaned glass slides. The slides were placed on a hot plate to speed up the evaporation of water. After a few hours, the solutions turned into a heterogeneous film on the glass whose SFG spectrum could be measured in reflection geometry.

6.2.3. The m β CD-liposome interaction is lipid-specific

Small unilamellar vesicles (liposomes) composed of POPS, POPC, DPPC, DOPA, DPPA and DMPG (molecular structures are shown in Figure 6.1B) incubated with 1 mM of m β CD for approx. 24 hours. We verified that the liposomes were stable after the incubation by measuring their size distribution using DLS. We can see in Figure 6.2A that the size distribution of all of the tested liposomes remains narrow with a Z-average diameter of 100-130 nm, depending on the lipid. This confirms that the aggregation of liposomes does not occur over the tested period of time. Comparing the size distribution of the incubated liposomes to untreated control samples from the same batch (black curves), we see that the average size of POPS, POPC, and DOPA liposomes was virtually unchanged by the incubation with m β CD. The size of DPPC, DPPA and DMPG liposomes increased slightly but remained narrow and monomodal.

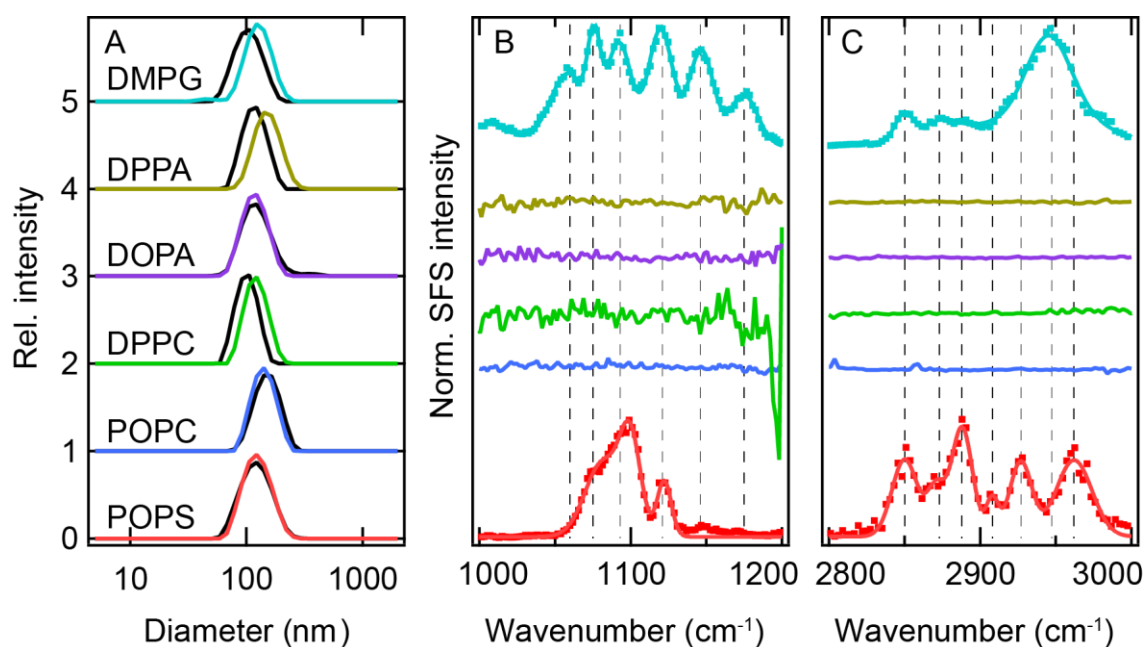


Figure 6.2: m β CD-liposome interaction is highly specific to the lipid head group. (A) The size distribution of liposomes incubated with 1 mM m β CD for ~24 hours (colored) versus control samples of liposomes from the same stock (black) obtained by DLS. (B) SFS spectra of the same liposome samples incubated with m β CD in the vibrational region 1000-1200 cm⁻¹ (PO region). The dashed lines indicate

approximate peak positions of 6 of the fitted vibrational modes. The fitted peak positions for POPS/DMPG are: -/1008, -/1057, 1077, 1090/1093, 1100/-, 1119/1120, 1145/1147, 1167/1175, and -/1220 cm^{-1} . The spectra are offset vertically for clarity. (C) SFS spectra of the same samples in the vibrational region 2800-3000 cm^{-1} (CH region). The dashed lines indicate fitted vibrational modes. The details of the fitting procedure are discussed in the appendix. The SFS spectra were obtained in ssp polarization combination.

Next, we measured the SFS response of the liposomes incubated with m β CD in two spectral regions: 1000-1200 cm^{-1} (PO region) and 2800-3000 cm^{-1} (CH region). The spectra were obtained in the ssp polarization combination where s-perpendicular and p-parallel designate the polarization of the light with respect to the scattering plane in the order SF, VIS, IR. The SFS spectra of the PO region are shown in Figure 6.2B. We can see that the SFS spectra of the treated liposomes vary dramatically depending on the constituent lipid. POPS and DMPG liposomes display a strong response with multiple vibrational peaks while POPC, DPPC, DOPA and DPPA liposomes do not. Similarly, in the CH region shown in Figure 6.2C, a strong response appears from POPS and DMPG liposomes incubated with m β CD but no response from POPC, DPPA, DOPA and DPPA liposomes. This difference in SFS responses indicates that the m β CD-lipid interaction selective to the headgroup. Next, we will analyze in detail the features in the SFS spectra of the POPS+m β CD and DMPG+m β CD samples.

The PO region (Figure 6.2B) contains 7-8 resolvable peaks for DMPG and 6 peaks for POPS. Since there are two potentially SFS-active molecules in our samples (the lipid and m β CD), we will consider the vibrational modes of both molecules in the measured spectral windows. The SFS-active modes of lipids are well known as there is a large body of literature on sum-frequency spectroscopic studies of lipid membranes which is not the case for m β CD. Starting with the lipids, the peak at $\sim 1057 \text{ cm}^{-1}$ can be assigned to the symmetric stretching of the CO-O-C group. This vibration is typically seen at 1070 cm^{-1} [82, 135, 140, 341] but H-bonding to the oxygen can lower the resonance frequency [67]. Peaks above 1070 cm^{-1} are assigned to the symmetric stretching of the phosphate group ($\nu_s(\text{PO}_2^-)$). The position of the $\nu_s(\text{PO}_2^-)$ peak is highly sensitive to H-bonding which lowers the resonance frequency. The peak at 1075 cm^{-1} likely corresponds to $\nu_s(\text{CO-O-C})$ or $\nu_s(\text{PO}_2^-)$. The 1093 cm^{-1} could also be assigned to the phosphate [82, 135, 140, 341]. The peaks around 1120 cm^{-1} are assigned $\nu_s(\text{PO}_2^-)$ from a dehydrated phosphate group [342, 343]. To verify whether m β CD has any SFS-active resonances in this spectral region, we have measured the sum-frequency spectra in a reflection geometry from a dried film of m β CD on a glass slide. The resulting spectrum shown in Figure 6.3A displays several resonances (green arrows): 1021, 1079, 1133, and 1160 cm^{-1} . These are similar to known IR/Raman active vibrations of β CD in this region. The vibrational modes of β CD reported in the literature are 1010-1046 cm^{-1} (C-C stretching, C-O-H bending,

C-C-H bending, C-C-O bending), 1050 cm^{-1} (C-O stretching, C-C stretching), 1079/1085 cm^{-1} (C-O stretching, C-C stretching, C-O-H bending), 1127 cm^{-1} (C-O-C stretching, C-C stretching) and 1157 cm^{-1} (C-O-C stretching, C-O stretching, C-C stretching, C-O-H bending) [344-346]. We can thus conclude that the SFS spectrum in the PO region contains vibrational modes of both the lipid headgroup and m β CD. Lastly, we note that freely dissolved m β CD in water, even if highly concentrated (100 mM), does not produce a measurable SFS response as can be seen from the SFS spectrum is shown in Figure 6.3A (red). This is due to a lack of orientational correlations between the dissolved m β CD molecules which leads to destructive interference of the SFS signal. The peak assignments are summarized in Table 6.1.

Table 6.1: Assignment of the peaks in the SFS spectra of the POPS+m β CD and DMPG+m β CD samples to vibrational modes. v_s -symmetric stretching, v_{as} -asymmetric stretching, FR stands for fermi resonance. For m β CD, which may contribute many vibrational modes, we refer to the discussion in the main text.

k (cm^{-1})	Vibrational mode	k (cm^{-1})	Vibrational mode
1057	$v_s(\text{CO-O-C})$	2850	$v_s(\text{CH}_2)$
1075	$v_s(\text{PO}_2^-)$, m β CD	2873	$v_s(\text{CH}_3)$
1090- 1110	$v_s(\text{PO}_2^-)$	2888	$v_{as}(\text{CH}_2)$
1120	$v_s(\text{PO}_2^-)$, m β CD	2908	$v_s\text{-FR}(\text{CH}_2)$ / $v_{as}(\text{CH}_2)$
1008, 1146, 1175	m β CD	2927	$v_s\text{-FR}(\text{CH}_3)$
		2946	$v_s\text{-FR}(\text{CH}_2)$
		2962	$v_{as}(\text{CH}_3)$

The peak positions in the SFS spectra of the CH region match those previously reported for planar lipid membranes [89] and lipid monolayers on oil nanodroplets [135, 140]. This indicates that the SFS spectrum in the CH region in Figure 6.2B originates from the CH_2 and CH_3 groups in the acyl chains of the lipids. However, the same groups are also present in m β CD. To confirm whether these groups are also SFS-active, we measured sum-frequency spectra in reflection mode from dry films of m β CD on a glass slide. To overcome a possible structural heterogeneity of the dry film, we measured the SF reflection from 2 different spots to obtain a complete spectrum (black and gray lines), the measured spectra are shown in Figure 6.3B. The observed peaks (green arrows) are 2814, 2842, 2893, and 2940 cm^{-1} from the first spot and 2871, and 2967 cm^{-1} from the second spot. Based on the peak positions, it

seems that the first spot probes mostly CH₂ groups while the second spot probes CH₃ groups. The origin of the peak at 2814 cm⁻¹ is unknown but it does not appear in the SFS spectra of the liposome samples. Reflection SFG spectra from dry m β CD films in the CH region confirm that vibrational modes corresponding to symmetric and asymmetric methyl and methylene stretching in m β CD are also SFS-active. All spectra shown here were recorded in the spp polarization combination. The SFS spectra of all 8 polarization combinations are shown in Figure 6.7 in the appendix. The appearance of the SFS signal in all 8 polarization combinations indicates that the SFS signal is at least in part of bulk origin [162, 168].

As shown before, m β CD freely dissolved in water does not contribute any SFS signal in the CH spectral region (also in Figure 6.2B) for the same reasons as given for the PO region above. Lastly, we measured the SFS spectra of samples containing only POPS liposomes. The results for the PO and CH vibrational region are shown in Figure 6.3A and Figure 6.3B. As expected, the bare liposomes do not generate any SFS response due to complete destructive interference of the sum-frequency light generated by the two opposing lipid leaflets. This is consistent with previous SFS measurements of unilamellar, single-lipid liposomes [82].

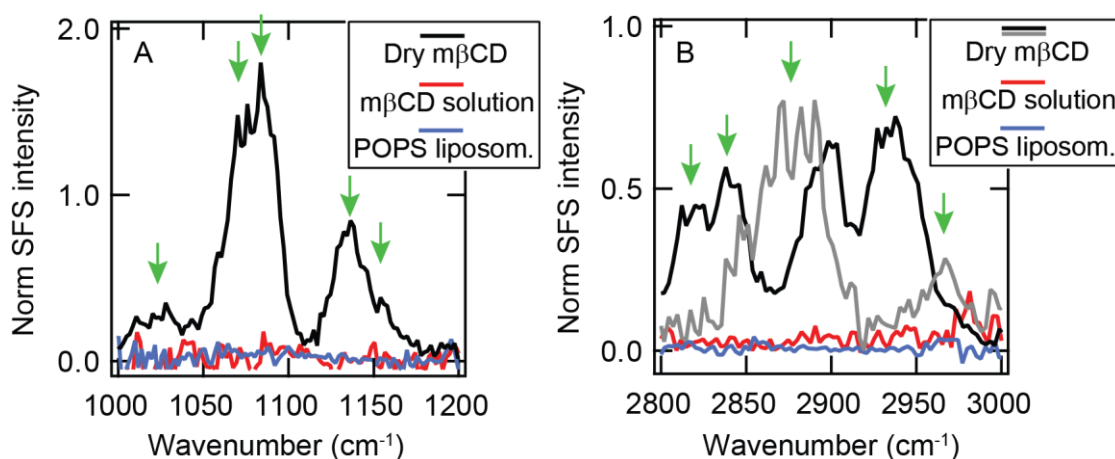


Figure 6.3: Control sum-frequency measurements of separate m β CD and POPS. (A) SF spectra of dry m β CD film, m β CD in solution (100 mM), and POPS liposomes alone in the PO region (1000-1200 cm⁻¹) recorded in the spp polarization combination. (B) SFS spectra of the same samples in the CH region (2800-3000 cm⁻¹). The gray and black curves correspond to different spots on the samples.

6.2.4. Time and concentration dependence of the SFS response

To estimate the minimum concentration of m β CD necessary to observe a nonlinear optical response, we measured the SFS spectra of POPS liposomes incubated with 0.001 – 1 mM m β CD for ~24 hours. Figure 6.4A shows the total SFS intensity in the PO and CH regions plotted against m β CD concentration. We can see that no response is seen below 1 mM which confirms that the lower limit of the m β CD concentration is around 1 mM. At this concentration,

the m β CD:lipid ratio is approx. 1:6 which is significantly lower compared to the concentrations used in other studies. In calorimetry experiments, the m β CD:lipid ratios used were >2:1 [317, 318], for fluorescence experiments 6.6:1, and for m β CD-mediated lipid transfer an 8:1 ratio is used [96, 347, 348]. DPPC liposomes are destabilized at the ratio of 7:1 [322] while the ratio required to completely dissolve POPC liposomes was estimated to be ~16:1 [318]. Therefore, at the 1:6 ratio employed here the liposome stability is not expected to be compromised.

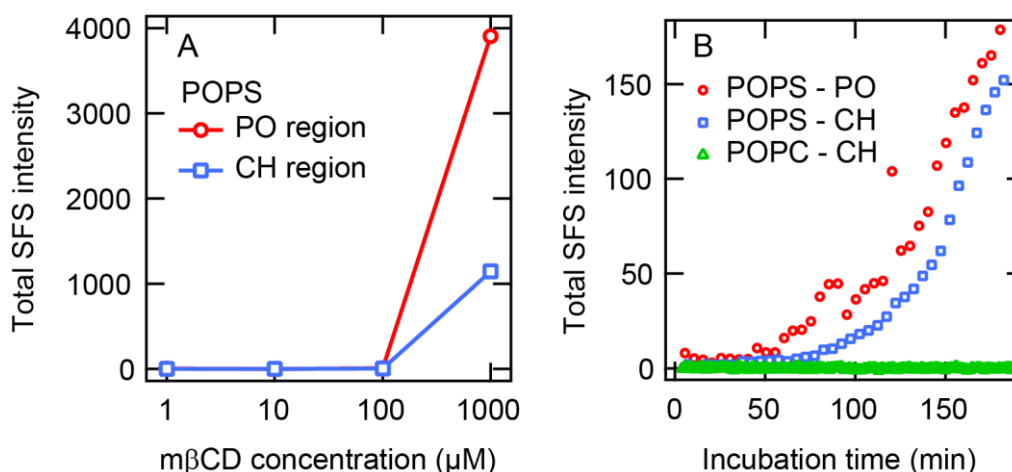


Figure 6.4: Concentration and time dependence of the SFS response from POPS and POPC liposomes incubated with m β CD. (A) Total SFS intensity obtained from POPS liposomes incubated with m β CD for ~24 hours as a function of m β CD concentration. The PO region corresponds to SFS intensity integrated in the region 1000-1200 cm^{-1} , the CH region corresponds to the region 2800-3000 cm^{-1} . (B) Time-lapse of the total SFS intensity from POPS and POPC liposomes incubated with 1 mM m β CD as a function of incubation time. All SFS spectra were recorded in the ssp polarization combination.

Next, we measured the SFS intensity of POPS incubated with 1 mM m β CD as a function of incubation time. The results for the PO and CH spectral regions are plotted in Figure 6.4B. We can see that there is no SFS response in either region for the first ~1 hour of incubation. Afterward, the SFS intensity rises over time with the PO region slightly ahead of the CH region. The intensity rise does not level off within the measured time frame of 3 hours. This observation indicates that the m β CD-liposome interaction is not a simple diffusion-limited adsorption of m β CD from the bulk to the liposome surface. Such a process would reach an equilibrium almost instantaneously. The observed kinetics are neither limited by the rate of lipid extraction from the membrane by m β CD which occurs within minutes [321]. There must be a different process driving the slow increase of the SFS response. We will explore this further by measuring the angular distribution of the scattered light.

6.2.5. Structure of the m β CD-liposome complex

The SFS measurements presented above point to slowly evolving but significant structural changes in the POPS+m β CD samples. To elucidate what structural changes are taking place, we used angle-resolved second-harmonic scattering (SHS). Here, we measure the non-resonant response of the sample at the second-harmonic frequency (514 nm) as a function of the scattering angle (θ). The angular distribution of the scattered SH intensity (scattering pattern) carries information about the size, shape, and symmetry of the scattering object [162, 166, 214, 304].

The SHS patterns of POPS+m β CD, as well as POPS liposomes alone and m β CD alone, were recorded in ppp polarization combination and are shown in Figure 6.5A. The SHS pattern of m β CD (black triangles) is virtually 0 everywhere, confirming that dissolved m β CD does not self-associate into large structures and that the individual solutes have a negligible SHS response due to their small size. The SHS patterns of bare POPS liposomes (blue squares) contain two symmetric lobes (at approx. $\pm 50^\circ$) with an amplitude of ~ 0.34 and no forward scattering. This type of scattering originates from orientationally correlated water at the liposome-water interface and is consistent with previously reported patterns of a wide range of liposomes [69, 76, 82, 137, 140]. In contrast, the SHS pattern of the POPS+m β CD sample (red circles) differs drastically from both POPS and m β CD individually. For scattering angles above 45° the POPS+m β CD matches the POPS pattern. Below 45° the intensity of the POPS+m β CD sample increases in intensity and peaks at 0° . The drastic difference in the scattering pattern of POPS+m β CD compared to POPS alone suggests that there is another particle present in the POPS+m β CD with completely different symmetry from the POPS liposomes.

To extract information about the molecular structure of the unknown object from the scattering pattern, let us consider the theory of nonlinear scattering [153, 156, 160, 162, 166, 214]. Under collinear excitation, centrosymmetric particles (e.g. liposomes) with an isotropic surface do not generate SHS intensity in the forward direction (around 0°) [156, 160, 162]. The presence of a forward peak in the scattering pattern is an indication of scattering from the bulk of a noncentrosymmetric particle [168]. The width of the peak is inversely proportional to the size of the scattering object. The DLS measurements (Figure 6.2A) show evidence of no particles other than the liposomes (diameter ~ 120 nm). However, 120 nm particles would generate a broader scattering pattern. This can be seen from the calculated patterns for particles ranging from 1 to 10000 nm shown in Figure 6.8A. We must consider the possibility that DLS cannot resolve the large particle. Such an effect can occur if the linear scattering cross-section of the unknown particle is negligible compared to the liposomes. To illustrate

how this can happen, we will explore two extreme cases: the unknown particle as a sphere or as a fiber.

From the narrow width of the SHS pattern, we can already estimate that the particle necessary to produce such a pattern is $\sim 1 \mu\text{m}$ in size, regardless of its exact shape. If we assume that the particle is spherical, it can easily be shown that the particle should be visible with DLS: The intensity of light scattered in the (linear) RGD approximation is given by [349]:

$$I_{RGD} \propto N_p V_p^2 \quad (6.1)$$

Where N_p is the number density and V_p is the volume of the particle. Using the above formula, we can calculate the relative intensities of light scattered by the liposomes and the unknown particle by taking a ratio of their intensities:

$$Rel. intensity = \frac{N_{liposome}}{N_{particle}} \left(\frac{V_{liposome}}{V_{particle}} \right)^2 \quad (6.2)$$

Where the volume of the liposome is calculated from its hydrodynamic radius (115 nm): $V_{liposome} \cong 6.4 \times 10^6 \text{ nm}^3$. The number density of the liposomes can be calculated from the known lipid concentration and the area per lipid ($N_{liposome} = 2.9 \times 10^{12}$ liposomes/mL for the DLS and SHS measurements). The volume of an m β CD molecule (from Figure 6.2A) is $\sim 0.26 \text{ nm}^3$ which means that to fill a sphere of $1 \mu\text{m}$ diameter would require $\sim 2 \times 10^6$ m β CD molecules. At the m β CD concentration used here (1 mM), the number density of such particles would be at least 10^5 less than that of the liposomes. However, the volume squared of a $1 \mu\text{m}$ sphere is 2.3×10^6 times larger than that for a 115 nm liposome. In total, using the above equation, this would amount to $\sim 4 \times$ more light scattered by the unknown particle relative to the liposome if it were spherical which would have been detected in the DLS measurements shown in Figure 6.2A. If instead, we suppose that the particle is a thin 1-micron long fiber with a radius of 1 nm, the intensity scattered by one such a fiber would be $> 6 \times 10^4$ times less than the intensity scattered a liposome due to the large difference in volume. The number density of the fibers would be approximately twice that of liposomes. In total, the fibers would scatter nearly 4×10^4 times less light than the liposomes. To account for at least 1% of the scattered intensity, the fibers would have to have a radius of 200 nm. The same considerations that we use for linear scattering also hold for SHS. However, unlike linear scattering, SHS requires the breaking of inversion symmetry. Since the liposomes in 25 mM NaCl are nearly perfectly centrosymmetric (except for a slight asymmetry in the hydration [82]) this means that the SHS intensity of the

liposomes is relatively weak (blue squares in Figure 6.5A). In comparison, the fibers are non-centrosymmetric which enhances their SHS intensity relative to the liposomes.

To confirm that fiber can produce the measured SHS response, we calculated scattering patterns of elongated cylinders with various symmetries and dimensions. The theory of SHS from cylindrical particles is discussed in Chapter 2 and was developed in Ref. [166]. The details of the calculation are discussed in detail in the appendix. The calculations indicate that the measured SHS pattern corresponds to $\sim 1.2 \mu\text{m}$ long fiber with a single non-vanishing susceptibility element $\chi_{x'z'z'}^{(2)}$ where \hat{z}' is the direction of the cylinder's axis. The green solid curve in Figure 6.5A represents the calculated SHS pattern of such a fiber averaged over all orientations in space. For the radius of the fiber, we used the value $R = 1 \text{ nm}$. However, the model is not insensitive to the exact value of R , as long as $R \ll \text{length}$. The shape of the pattern is mostly determined by used $\chi^{(2)}$ element and the length. The occurrence of the $\chi_{x'z'z'}^{(2)}$ element indicates that the fiber lacks a two-fold rotational symmetry [102]. This can be explained if we consider that the structure of m β CD is a 7-membered ring (Figure 6.1A). As such, we can expect the fiber to have at most a 7-fold rotational symmetry. Given that the hydroxyl groups of m β CD are randomly methylated the molecule may not possess any rotational symmetry.

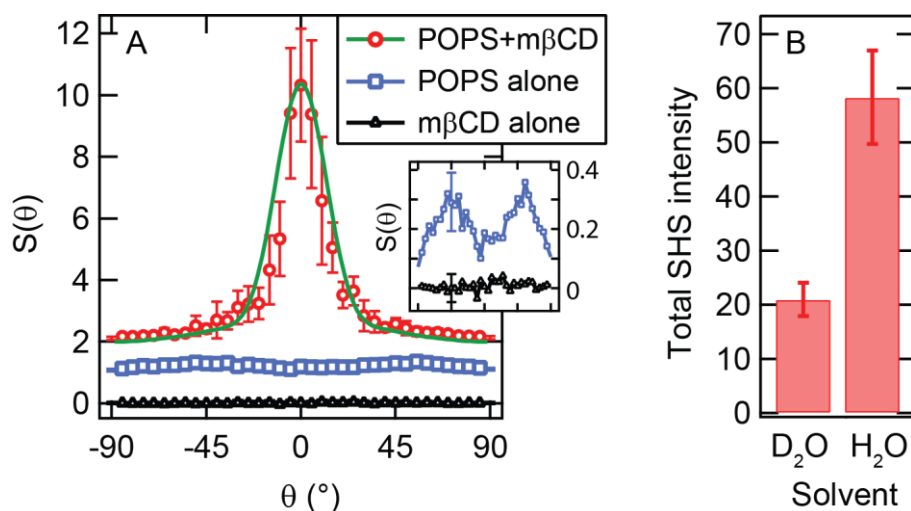


Figure 6.5: Second-harmonic scattering from POPS+m β CD. (A) SHS patterns of POPS+m β CD, POPS liposomes alone, and m β CD alone in the same solvent (25 mM NaCl in D₂O). For clarity, the patterns are offset vertically. The m β CD pattern is virtually 0 everywhere, i.e. the SHS intensity is the same as that of the solvent, the POPS pattern contains 2 symmetric lobes at $\pm 50^\circ$ with an amplitude of ~ 0.34 (visible in the inset) typical for centrosymmetric particles. Inset: detailed view of the POPS and m β CD patterns. The POPS+m β CD pattern differs significantly from the two previous patterns in that it shows a strong forward peak. The green solid curve represents a calculated pattern from of a randomly oriented, noncentrosymmetric cylinder ($L = 1.2 \mu\text{m}$, $R = 1 \text{ nm}$, $\chi_{x'z'z'}^{(2)} \neq 0$). All patterns were recorded in

the ppp polarization combination. (B) Total SHS intensity (integrated pattern) of the same POPS+m β CD sample in D₂O vs H₂O. The 3 \times higher scattered intensity from H₂O solutions indicates that the SHS response originates from hydrating water molecules that are orientationally correlated.

6.2.6. Hydration

In SHS experiments on lipid membranes, the response is dominated by the hydrating water molecules rather than the membrane itself due to the large number density of water (30 water molecules per nm³) [69, 75, 76, 79, 82, 115, 350]. To determine the extent to which hydrating water contributes to the measured SHS response of the fiber, we performed an isotope exchange experiment where the heavy water used as a solvent is replaced by light water. D₂O forms stronger H-bonds with itself [11] and therefore its orientational order is less influenced by an added particle. If all else is equal, and the source of SHS are orientationally correlated water molecules, then D₂O solutions should scatter less SHS light compared to H₂O [41, 210]. To make the intensities of the two samples comparable, we used the same stock solution POPS+m β CD sample and dilutes it 10 times using either H₂O or D₂O (+25 mM NaCl). The comparison of the total SHS intensity of the two samples is shown in Figure 6.5B. We can see that diluting the sample with H₂O leads to a nearly 3 \times increase in the total (normalized) SHS intensity compared to a sample diluted in D₂O. Although we cannot give a quantitative estimate of the relative contribution of water compared to the fiber itself, the large difference in the SHS intensities suggests that most if not all of the intensity could originate from hydrating water. This observation is interesting for two reasons: 1. It suggests that hydration plays an important role in the self-assembly and stabilization of the fiber, and 2. The orientational correlations between water molecules extend up to 1.2 μ m in distance (the length of the fiber).

6.2.7. The self-assembly mechanism

The high degree of selectivity to the lipid head groups indicates that the H-bonding of m β CD to the head groups is key. The m β CD contains 14 oxygen atoms in which can potentially serve as H-bond acceptors and up to 21 O-H groups (depending on the degree of methylation) that can serve as H-bond donors or acceptors. On the lipid side, each tested lipid has at least 8 H-bond acceptor sites (2 from each fatty acid + 4 from the phosphate). Assuming that the phosphate is ionized, the PA lipids possess 1 additional H-bond donor while the PC lipids possess no additional H-bonding sites. In contrast, POPS contains 2 more acceptor sites (carboxyl) and 1-2 donor sites (amine and carboxyl, depending on its ionization state). DMPG also contains 2 donors and 2 acceptors (O-H groups). In summary, POPS and DMPG contain significantly more H-bonding sites than the other tested lipids. Moreover, the additional

bonding sites are situated on the outermost part of the headgroup where it is most easily accessible for bonding. This would explain the preference of m β CD for PS and PG over PC and PA. The suggested binding models between m β CD and lipid headgroups are illustrated in Figure 6.6. Our observation is also in agreement with previous reports of β CD binding to the carboxyl and phosphate groups [328-331].

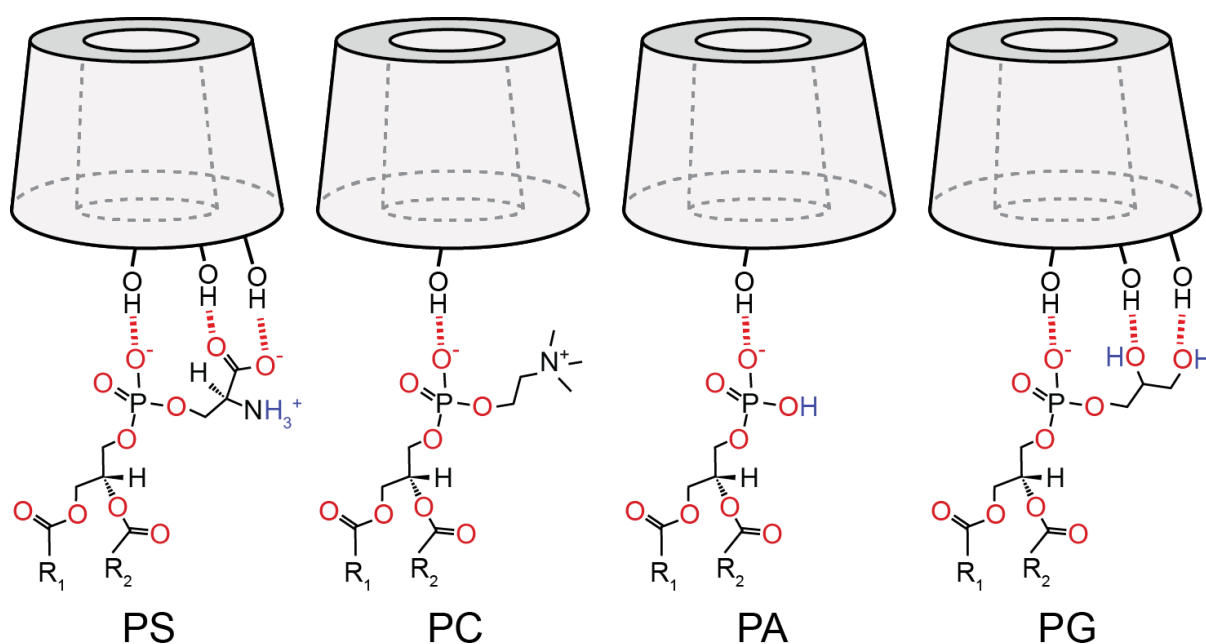


Figure 6.6: Suggested binding model of m β CD to lipid head groups. The preference of m β CD for PS and PG over PA and PC is due to H-bonding of the lipid headgroup to hydroxyl (OH) groups on m β CD. PS and PG contain significantly more H-bond donor (blue) and acceptor sites (red) than PA and PC. (OH) groups on m β CD. Some of the possible H-bond configurations are illustrated by dashed red lines. Other configurations are possible as well.

Going back to the SFS data (Figure 6.2B,C), we have shown that the measured vibrational modes originate from the lipids as well as m β CD. This indicates that the spatial arrangement of both molecules breaks the inversion symmetry. This means that the lipids and m β CD stack in approximately the same direction, allowing for constructive interference from successive molecules along the length of the fiber. If this were not the case (i.e. random stacking of antiparallel stacking) there would be a destructive interference SFS signal would be measured [82, 126, 135].

6.3. Discussion

The strong lipid head group selectivity of the m β CD-liposome interaction as measured by SFS (Figure 6.2B,C) is surprising compared to what has been reported in the literature. Huang et al [320] measured the concentration of m β CD needed to dissolve liposomes with different compositions and reported only slight differences between lipid headgroups: PG (18 mM) and PS (25 mM), PC (28 mM) but such concentrations are an order of magnitude higher than the concentration used here (1 mM).

To the best of our knowledge, the self-assembly of m β CD into micron-sized large structures has not been reported before. m β CD is highly soluble in water (up to 0.5 M) and forms only nanoscopic aggregates near the solubility limit [323]. In contrast, the native, non-methylated variant (β CD) is poorly soluble in water (\sim 16 mM) and forms aggregates in the 100 nm range near saturation [323]. The low solubility and self-assembly of native β CD are driven by the hydrophobic interactions and H-bonding between β CD which is countered by methylation of some OH groups in m β CD [323, 351]. In light of this, how can we explain the self-assembly of m β CD into micrometer long fibers at only 1 mM? It is known that the self-assembly of CDs can be driven by complexation with guest molecules. This has been shown for complexes of β CD which can grow into rod-shaped microcrystals [336, 337, 352-356]. Our results indicate that m β CD behaves in a similar fashion in the presence of PS and PG lipids. Vertical stacking of the m β CD-lipid complexes can proceed via H-bonding of the lipid head groups to hydroxyl groups on m β CD as shown above.

6.4. Conclusion

We have investigated the interaction of methyl- β -cyclodextrin (m β CD) with liposomes composed of various lipids using a combination of dynamic light scattering (DLS), sum-frequency scattering (SFS), second-harmonic scattering (SHS) and theoretical modeling. According to DLS measurements, there is no significant change in the size distribution of the liposomes after introducing m β CD. In contrast, SFS measurements reveal significant structural changes that occur over hours and days. m β CD is shown to be strongly selective to the lipid head group with a preference for phosphatidylserine (PS) and phosphatidylglycerol (PG) over phosphatidylcholine (PC) and phosphatidic acid (PA). We explain this selectivity stems from the larger number of H-bonding sites in PS and PG over PC and PA which can bind to the hydroxyl groups and oxygen atoms on m β CD. By performing angle-resolved SHS measurements and modeling the resulting scattering patterns using the theory of nonlinear scattering, we find that the m β CD-lipid complexes self-assembled into micron-long ordered fibers. Isotope exchange between heavy and light water reveals the SHS response originates

from hydrating water molecules that are spatially correlated with the fiber. The strong isotope effect in the hydration suggests that hydration contributes to the self-assembly and stability of the fibers. The observed self-assembly of m β CD is reminiscent of the less soluble variants of cyclodextrins that tend to self-assemble into microscopic rod-shaped crystals via complexation. Such behavior has not been observed before in m β CD and is surprising given that m β CD was specifically designed to be highly soluble. Our observations highlight the intrinsic sensitivity of nonlinear scattering to changes in the molecular order on the nanoscale which are difficult if not impossible to detect by other techniques. The present findings are highly relevant in light of the widespread use of cyclodextrins in the pharmaceutical or food industries, and in fundamental research.

6.5. Appendix

6.5.1. SFS spectra of POPS+m β CD in all polarization combinations

The SFS spectra of the POPS+m β CD sample were recorded in all 8 polarization combinations: sss, ssp, ppp, pps, pss, sps, psp, spp. The spectra of the PO region are shown in Figure 6.7A-D, the spectra of the CH region are shown in Figure 6.7E-H. The appearance of the SFS signal in all 8 polarization combinations is inconsistent with scattering from centrosymmetric particles with an anisotropic surface (single-lipid liposomes) [162]. Instead, this is indicative of scattering from non-centrosymmetric particles [168].

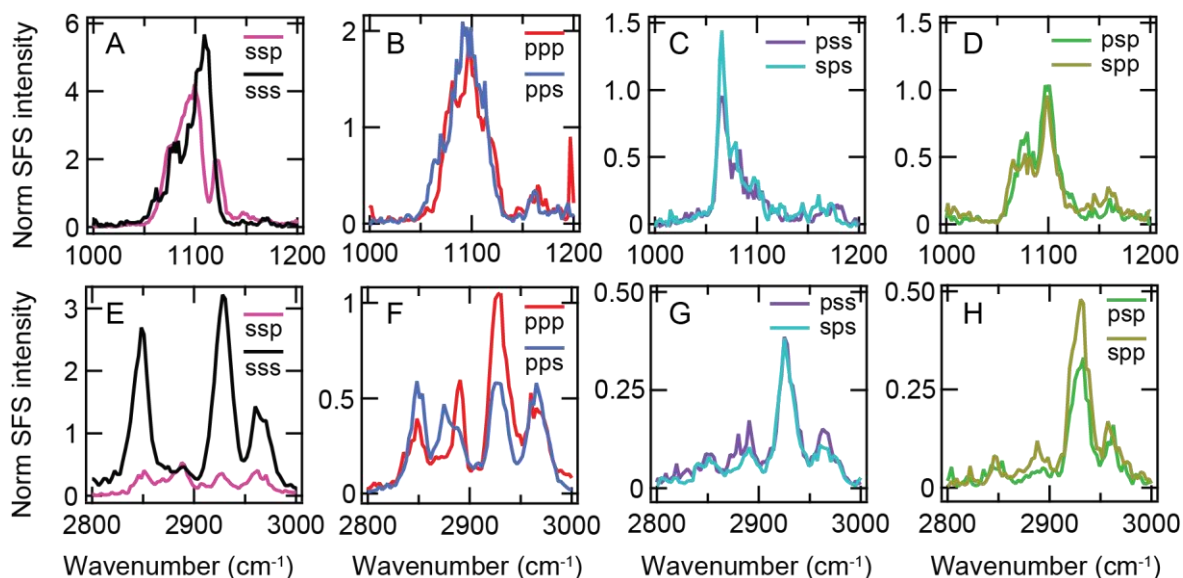


Figure 6.7: SFS spectra of POPS+m β CD in all 8 polarization combinations. (A-D): PO region. (E-H): CH region

6.5.2. Fitting of the SFS spectra

The SFS spectra in Figure 6.2B,C were fitted according to Eq. (2.39). The fitted amplitude (A_i), frequency (ω_i) and linewidth (γ_i) for POPS+m β CD and DMPG+m β CD are shown in Table 6.2.

Table 6.2: Fitted amplitude, frequency and linewidth of the POPS and DMPG samples.

POPS+m β CD				DMPG+m β CD		
A_i	ω_i (cm $^{-1}$)	γ_i (cm $^{-1}$)		A_i	ω_i (cm $^{-1}$)	γ_i (cm $^{-1}$)
3.08	1077	5.24		8.03	1008	10.08
12.13	1090	9.11		21.30	1057	10.20
9.00	1100	6.75		18.87	1076	6.12
3.41	1119	3.76		23.15	1093	7.88
1.09	1145	4.07		32.65	1120	9.06
0.36	1167	3.00		26.80	1147	9.11
				11.37	1175	7.12
				3.27	1220	11.43
1.23	2851	9.40		3.40	2853	3.92
1.80	2887	9.99		9.60	2873	11.65
0.06	2909	3.00		11.10	2892	13.13
0.81	2927	6.58		32.22	2930	17.19
1.64	2962	11.36		31.52	2947	13.07
				0.46	2977	3.00

6.5.3. SH scattering from a randomly oriented cylinder

The theory of SHS from cylindrical particles was developed by J.I. Dadap [166] and is elaborated in detail in Chapter 2. By solving the equations for the scattered SH intensity from a non-centrosymmetric cylinder with a single non-vanishing susceptibility element $\chi_{x'z'z'}^{(2)}$ (with the axis of the cylinder along the \hat{z}' direction) in the ppp polarization combination, we obtain the expressions:

$$\begin{aligned}
 I_{cyl}(\alpha, \beta; \theta) &= \left| s_\alpha^2 c_\alpha s_\beta^2 c_\theta f_{cyl} \chi_{x'z'z'}^{(2)} \right|^2 \\
 f_{cyl} &= 2 \frac{J_1(QR)}{QR} \frac{\sin(Q_3 L/2)}{Q_3 L/2} \\
 Q &= k_0 \sqrt{c_\alpha^2 s_\theta^2 + \left((c_\theta - 1) s_\beta - c_\beta s_\alpha s_\theta \right)^2} \\
 Q_3 &= k_0 [c_\beta (c_\theta - 1) + s_\alpha s_\beta s_\theta]
 \end{aligned} \tag{6.3}$$

where J_1 is the Bessel function of the first kind and first order, $s_i = \sin(i)$, $c_i = \cos(i)$, $k_0 = 2\pi/\lambda_{SH}$, $\lambda_{SH} = 514$ nm, R is the radius of the cylinder, L is its length, and α and β are Euler angles defining its orientation in space.

The SHS intensity the angle θ of an orientationally averaged cylinder is obtained by numerically integrating the following expression over the Euler angles α and β :

$$\langle I_{cyl}(\theta) \rangle = \int_0^{2\pi} \int_0^\pi I_{cyl}(\alpha, \beta; \theta) \sin(\beta) d\beta d\alpha \quad (6.4)$$

The integration was performed in Wolfram Mathematica 12.0 using the function `NIntegrate` on automatic settings with θ increments of 2° .

6.5.4. Dependence of SHS on the dimensions of the cylinder

By inserting the expressions in Eq. (6.3) into Eq. (6.4) and solving it numerically for a given radius, length, and scattering angle, we can calculate SHS patterns of randomly oriented cylinders of varying lengths and radii. Figure 6.8A shows calculated SHS patterns of cylinders with lengths from 1 to 10000 nm and a constant radius (1 nm). We can see that the best match between the actual and calculated pattern is found for a cylinder with a length of approx. 1200 nm. Figure 6.8B, shows calculated patterns for cylinders with a fixed length (1200 nm) and variable radii (1-1000 nm). The patterns are not sensitive to the value of $R < 100$ nm.

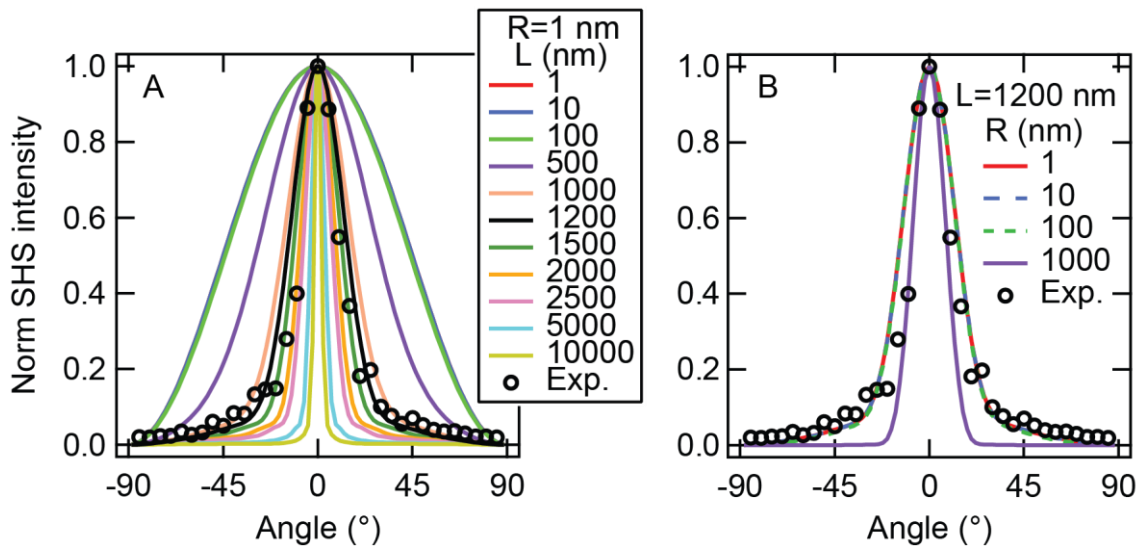


Figure 6.8: Calculated SHS patterns of randomly oriented, noncentrosymmetric cylinders. (A) SHS patterns of cylinders with 1 nm radius and length from 1 to 10000 nm. The length that matches

best with the experimental data (black rings) is approx. 1200 nm. (B) SHS patterns of cylinders 1200 nm long and with radius from 1 to 1000 nm. For radii much smaller than the length, the shape of the pattern is virtually independent of the radius. All patterns were calculated with a single non-zero susceptibility element $\chi_{x'z'z'}^{(2)}$ and in ppp polarization combination. All patterns are normalized to 1.

6.5.5. The choice of the $\chi^{(2)}$ element

Since we have no apriori knowledge about the symmetry of the self-assembled POPS-m β CD fiber, we cannot predict which elements of the $\chi^{(2)}$ tensor will be nonvanishing (and what are their values). To determine the $\chi^{(2)}$ element that dominates the SHS response, we have calculated the scattering patterns from a randomly oriented cylinder ($L = 1.2 \mu\text{m}$, $R = 1 \text{ nm}$) for 9 different $\chi^{(2)}$ elements to see which element best represents the measured data. In Figure 6.9 we show the calculated patterns for a cylinder ($L = 1200 \text{ nm}$, $R = 1 \text{ nm}$) using the following $\chi^{(2)}$ elements: $\chi_{z'z'z'}^{(2)}$, $\chi_{z'z'x'}^{(2)}$, $\chi_{z'x'x'}^{(2)}$, $\chi_{x'z'z'}^{(2)}$, $\chi_{x'x'z'}^{(2)}$, $\chi_{y'x'x'}^{(2)}$, $\chi_{x'x'y'}^{(2)}$, $\chi_{x'y'z'}^{(2)}$, $\chi_{x'x'x'}^{(2)}$. Each $\chi^{(2)}$ element produces a scattering pattern with a distinct shape. The best match is found for the element $\chi_{x'z'z'}^{(2)}$.

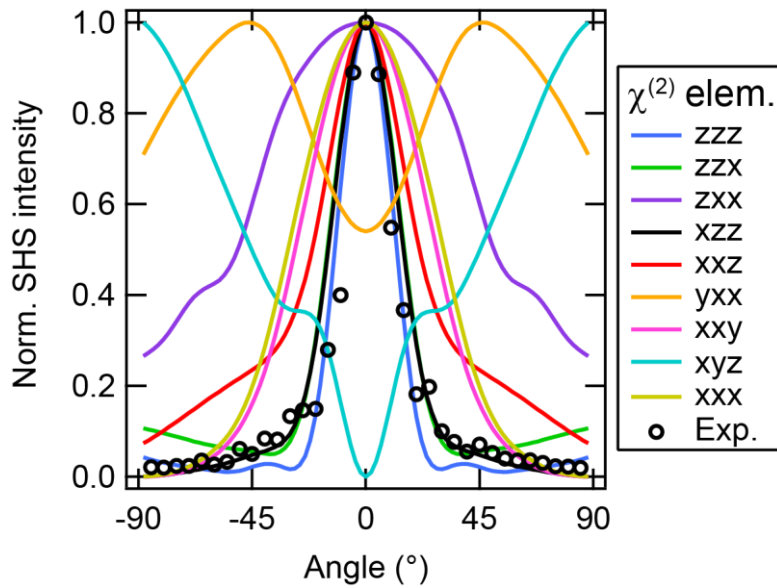


Figure 6.9: Calculated SHS patterns of a randomly oriented cylinder ($L=1200 \text{ nm}$, $R=1 \text{ nm}$) for different non-zero $\chi^{(2)}$ elements. The experimental data is shown with black rings. All patterns were calculated for the ppp polarization combination and are normalized to 1.

Chapter 7: Conclusion and outlook

7.1. Summary

In this thesis, we studied several systems that can be broadly categorized as soft matter: aqueous polyelectrolyte solutions and aqueous dispersions of liposomes. We used nonlinear spectroscopic techniques to elucidate the presence, spatial extent and consequences of extended hydration induced by polyelectrolytes, the electrostatics and hydration in protein-membrane interaction, and the molecular structure and hydration of a supramolecular assembly.

Chapter 2 provided an overview of the theory of nonlinear light scattering from the surfaces of neutral and charged spherical particles, from cylindrical particles, and from bulk liquids of orientationally-correlated molecules. The experimental realizations of angle-resolved elastic second-harmonic scattering (SHS) and vibrational sum-frequency scattering (SFS) used in this thesis were discussed, as well as the supporting techniques.

In Chapter 3 we probed the orientational order in aqueous solutions of hyaluronan, a linear polyelectrolyte of biological origin. We showed that at low ionic strength the electric field of the polyelectrolyte induces a long-range order in the aqueous solvent. This leads to SHS patterns reminiscent of charged particles dispersed in water. We used a theoretical model of SHS from charged particles to explain the SHS response. The concentration-dependence of the SHS response is attributed to a combination of shrinking Debye length, and a suppression of intra- and inter-chain correlations mediated by the weakly screened electric field generated by hyaluronan. A solvent isotope exchange where light water (H_2O) was replaced by heavy water (D_2O) led to a 6.3-fold decrease in the scattered intensity and a 2.4-fold shift of the concentration vs. intensity curve. A similar effect was previously observed in electrolyte solutions and indicates that hyaluronan enhances water-water orientational correlations. The isotope effect in the fs-ESHS response is thus ascribed to a nuclear quantum effect. Finally, based on temperature dependence measurements, we estimated the extent of the hydration shell of HA to be 475 nm in H_2O and 260 nm in D_2O .

In Chapter 4 we investigated the orientational order and viscosity of aqueous solutions of two common synthetic polyelectrolytes: poly(acrylic acid) and poly(styrene sulfonate). We showed that there is a strong correlation between the reduced viscosity and the orientational order in the water (measured by SHS). The viscosity and SHS curves shifted to 10 times higher concentration after replacing H_2O by D_2O but the correlation between both quantities was preserved. The viscosity of the polyelectrolytes displays a known anomalous increase upon

dilution. Existing mean-field models explain the anomaly through inter- and intra-polyelectrolyte correlations. Our data shows that such models cannot explain the difference between H₂O and D₂O and conclude that water-water correlations must contribute to the anomalous viscosity of polyelectrolytes.

In chapter 5 we studied the binding of the protein alpha-synuclein to anionic small unilamellar vesicles (liposomes) from the perspective of hydration using angle- and polarization-resolved SHS. The protein binding leads to a decrease in the SHS intensity but no change in the electrophoretic mobility (zeta potential) of the liposomes is observed. By applying a theoretical model to the SHS patterns we find that the net orientational order of the interfacial water is decreased by 30% but the surface potential is unaffected. We propose that the negatively-charged C-terminal of the protein is detached from the surface, disrupting the structure of the interfacial water. A polarization-resolved SHS measurement reveals no chiral response from the bound protein indicating that the α -helix at the N-terminal lies flat on the liposome surface.

Chapter 6 presents a study of the interaction between methyl- β -cyclodextrin (m β CD) and liposomes composed of various lipids. Cyclodextrins are widely used to extract membrane lipids by forming water-soluble inclusion complexes. We show that lipids with a high number of H-bonding sites (i.e. phosphatidylserine and phosphatidylglycerol) bind via H-bonding to the oxygen atoms or hydroxyl groups on m β CD. This causes the lipid-cyclodextrin complexes to self-assemble into micrometer-long fibers. Isotope exchange experiments indicate that the assemblies contain a large amount of hydrating water which suggests that hydration plays a role in the assembly process.

7.2. Outlook

This work has opened several possibilities for future studies. In Chapters 3 and 4, we showed that polyelectrolytes carry extended hydration shells spanning up to hundreds of nanometers. Although water is the most interesting liquid from a biological perspective, there are other polar liquids in which we can expect to observe long-range orientational ordering, such as acetone, ethanol, dimethylsulfoxide, and dimethylformamide. Performing the same experiments in other solvents may highlight the differences between water and other polar liquids that do not form H-bonds or whose H-bonding only 1- or 2-dimensional.

Chiral surface-bound molecules have been shown to imprint chirality into the structure of the hydrating water but the same effect has not yet been observed in dissolved molecules. Given that proteins, DNA and other polyelectrolytes have a helical structure in water can we

expect to observe a non-zero chiral response from these solutions? Some of the data for hyaluronan (not included in this thesis) suggests that this might be the case but the results are inconclusive. More accurate polarization-resolved measurements may give a definitive answer.

In Chapter 5 we developed a novel approach to measuring protein binding to vesicles in a label-free and surface-specific manner using angle-resolved SHS and theoretical modeling. Here, we used the protein α -synuclein which is known to strongly bind to anionic vesicles. The same approach should be applicable to study the binding of a wide range of proteins, not only those that bind electrostatically to the surface, but also membrane-spanning and pore-forming proteins. One drawback of measuring changes in the interfacial water and surface electrostatics as proxies for protein binding is the need to work at a relatively low ionic strength (< 1 mM) compared to physiological conditions (> 100 mM) which may affect the behavior of some proteins. This limitation could be partly overcome by increasing the sensitivity of the measurements such as by using larger vesicles that scatter more light. Another way to circumvent this limitation would be to use sum-frequency scattering (SFS) to detect vibrational modes of the amide (~ 1650 cm^{-1}), N-H (~ 3300 cm^{-1}), phosphate (~ 1100 cm^{-1}), methyl and methylene groups (~ 2900 cm^{-1}) found on the proteins or the lipids. Here, it may also be necessary to use larger vesicles to increase the number of scattered photons.

Apart from proteins, peptides are another class of molecules whose interaction with membranes is of considerable interest but remains poorly understood. For example, in light of the growing number of bacteria with antimicrobial resistance, a better molecular-level understanding of the mechanism by which antimicrobial peptides disrupt lipid membranes could inform the development of new medicines.

In Chapter 6 we explored the interaction of methyl- β -cyclodextrin with various lipids. We showed that nonlinear scattering techniques were able to detect molecular-level structural changes in cyclodextrin-lipid complexes that were not measurable by traditional light scattering. To further elucidate the role of H-bonding in the self-assembly process the experiments could be repeated at different pH which would change the protonation state of the lipid headgroups. To assess more accurately the importance of hydration, one could attempt to disassemble the fibers by introducing structure breaking agents such as urea that are also used to denature proteins. Lastly, the results shown in this chapter imply that using vibrational SFS to probe transmembrane asymmetry in liposomes prepared by the cyclodextrin-mediated lipid exchange method will be challenging. This is due to the strong SFS signal from the self-assembled complexes which would overwhelm the (presumably weak) signal from the asymmetric liposomes. It may still be feasible to use SFS to probe induced transmembrane

asymmetry in liposomes if a way is found to prevent the self-assembly of the m β CD-lipid or to purify the samples without disrupting the liposomes, or by using an entirely different protocol for asymmetry in liposomes.

List of publications

This thesis is based on the following publications or manuscripts:

1. **Dedic, J.**, Okur, H.I., Roke, S., Hyaluronan orders water up to hundreds of nanometers and induces significant nuclear quantum effects. In preparation.
2. **Dedic, J.**, Okur, H.I., Roke, S., Polyelectrolytes induce water-water correlations that result in dramatic viscosity changes and nuclear quantum effects. *Sci. Adv.* **5**, eaay1443, doi:10.1126/sciadv.aay1443 (2019).
3. **Dedic, J.**, Rocha, S., Okur, H.I., Wittung-Stafshede, P., Roke, S., Membrane–Protein–Hydration Interaction of A-Synuclein with Anionic Vesicles Probed Via Angle-Resolved Second-Harmonic Scattering. *J. Phys. Chem. B* **123**(5), 1044-1049 (2019).
4. **Dedic, J.**, Okur, H.I., Roke, S., Self-assembly of methyl- β -cyclodextrin/lipid complexes probed by nonlinear scattering. In preparation.

Publications not described in this thesis:

5. Chen, Y., Okur, H.I., Dupertuis, N., **Dedic, J.**, Wilkins, D.M., Ceriotti, M., Roke, S., Comment on “Water-Water Correlations in Electrolyte Solutions Probed by Hyper-Rayleigh Scattering” [*J. Chem. Phys.* 147, 214505 (2017)]. *J. Chem. Phys.* 149(16), 167101 (2018).
6. **Dedic, J.**, Okur, H., Roke, S. Probing Lipid Membranes with Vibrational Sum-Frequency Scattering. *Frontiers in Optics (conference)*, FM4B.3, (2018)

References

1. Russo, J., Akahane, K., Tanaka, H., Water-Like Anomalies as a Function of Tetrahedrality. *Proc. Natl. Acad. Sci. U. S. A.* 115(15), E3333-E3341 (2018).
2. Berger, A., Ciardi, G., Sidler, D., Hamm, P., Shalit, A., Impact of Nuclear Quantum Effects on the Structural Inhomogeneity of Liquid Water. *Proc. Natl. Acad. Sci. U. S. A.* 116(7), 2458-2463 (2019).
3. Narten, A., Thiessen, W., Blum, L., Atom Pair Distribution Functions of Liquid Water at 25 C from Neutron Diffraction. *Science* 217(4564), 1033-1034 (1982).
4. Bakker, H.J., Skinner, J.L., Vibrational Spectroscopy as a Probe of Structure and Dynamics in Liquid Water. *Chem. Rev. (Washington, DC, U. S.)* 110(3), 1498-1517 (2010).
5. Smith, J.D., *et al.*, Energetics of Hydrogen Bond Network Rearrangements in Liquid Water. *Science* 306(5697), 851-853 (2004).
6. Boyarkin, O.V., *et al.*, Accurate Bond Dissociation Energy of Water Determined by Triple-Resonance Vibrational Spectroscopy and Ab Initio Calculations. *Chem. Phys. Lett.* 568, 14-20 (2013).
7. Hindman, J.C., Svirmickas, A., Wood, M., Relaxation Processes in Water. A Study of the Proton Spin-Lattice Relaxation Time. *J. Chem. Phys.* 59(3), 1517-1522 (1973).
8. Kindt, J., Schmuttenmaer, C., Far-Infrared Dielectric Properties of Polar Liquids Probed by Femtosecond Terahertz Pulse Spectroscopy. *J. Phys. Chem.* 100(24), 10373-10379 (1996).
9. Omta, A.W., Kropman, M.F., Woutersen, S., Bakker, H.J., Negligible Effect of Ions on the Hydrogen-Bond Structure in Liquid Water. *Science* 301(5631), 347-349 (2003).
10. Bakker, H., Rezus, Y., Timmer, R., Molecular Reorientation of Liquid Water Studied with Femtosecond Midinfrared Spectroscopy. *J. Phys. Chem. A* 112(46), 11523-11534 (2008).
11. Soper, A.K., Benmore, C.J., Quantum Differences between Heavy and Light Water. *Phys. Rev. Lett.* 101(6), 065502 (2008).
12. Marcus, Y., Effect of Ions on the Structure of Water: Structure Making and Breaking. *Chem. Rev. (Washington, DC, U. S.)* 109(3), 1346-1370 (2009).
13. Chaplin, M., Do We Underestimate the Importance of Water in Cell Biology? *Nature Reviews Molecular Cell Biology* 7, 861 (2006).
14. Ball, P., Water Is an Active Matrix of Life for Cell and Molecular Biology. *Proc. Natl. Acad. Sci. U. S. A.* 114(51), 13327-13335 (2017).
15. Laage, D., Elsaesser, T., Hynes, J.T., Water Dynamics in the Hydration Shells of Biomolecules. *Chem. Rev. (Washington, DC, U. S.)* 117(16), 10694-10725 (2017).
16. Ma, L., Gaisinskaya-Kipnis, A., Kampf, N., Klein, J., Origins of Hydration Lubrication. *Nat Commun* 6, (2015).
17. Gat, J.R., Oxygen and Hydrogen Isotopes in the Hydrologic Cycle. *Annual Review of Earth and Planetary Sciences* 24(1), 225-262 (1996).
18. Ceriotti, M., *et al.*, Nuclear Quantum Effects in Water and Aqueous Systems: Experiment, Theory, and Current Challenges. *Chem. Rev. (Washington, DC, U. S.)* 116(13), 7529-7550 (2016).
19. Kuharski, R.A., Rossky, P.J., A Quantum Mechanical Study of Structure in Liquid H₂O and D₂O. *J. Chem. Phys.* 82(11), 5164-5177 (1985).
20. Millero, F.J., Dexter, R., Hoff, E., Density and Viscosity of Deuterium Oxide Solutions from 5-70. Deg. *Journal of Chemical & Engineering Data* 16(1), 85-87 (1971).
21. Hill, P.G., MacMillan, R.D., Lee, V., *Tables of Thermodynamic Properties of Heavy Water in SI Units*, 1981: Canada. p. 196.

22. Hill, P., MacMillan, R.C., Lee, V., A Fundamental Equation of State for Heavy Water. *Journal of Physical and Chemical Reference Data* 11(1), 1-14 (1982).
23. Korson, L., Drost-Hansen, W., Millero, F.J., Viscosity of Water at Various Temperatures. *J. Phys. Chem.* 73(1), 34-39 (1969).
24. Clough, S.A., Beers, Y., Klein, G.P., Rothman, L.S., Dipole Moment of Water from Stark Measurements of H₂O, HDO, and D₂O. *J. Chem. Phys.* 59(5), 2254-2259 (1973).
25. Tilton, L., Taylor, J., Refractive Index and Dispersion of Distilled Water for Visible Radiation, at Temperatures 0 to 60 C. *J. Res. Natl. Bur. Stand.* 20, 419-477 (1938).
26. Frontas' Ev, V., Shraiber, L., Study of the Variation in the Electron Polarizability of Molecules of Ordinary and Heavy Water under the Influence of Temperature. *Journal of Structural Chemistry* 6(4), 493-500 (1965).
27. Wyman Jr, J., Ingalls, E., The Dielectric Constant of Deuterium Oxide. *J. Am. Chem. Soc.* 60(5), 1182-1184 (1938).
28. Shoesmith, D.W., Lee, W., The Ionization Constant of Heavy Water (D₂O) in the Temperature Range 298 to 523 K. *Canadian Journal of Chemistry* 54(22), 3553-3558 (1976).
29. Eisenberg, D., Kauzmann, W., *The Structure and Properties of Water*. (Oxford University Press on Demand, 2005).
30. Tennyson, J., *et al.*, IUPAC Critical Evaluation of the Rotational–Vibrational Spectra of Water Vapor, Part III: Energy Levels and Transition Wavenumbers for H₂16O. *Journal of quantitative spectroscopy and radiative transfer* 117, 29-58 (2013).
31. Tennyson, J., *et al.*, IUPAC Critical Evaluation of the Rotational–Vibrational Spectra of Water Vapor. Part IV. Energy Levels and Transition Wavenumbers for D₂16O, D₂17O, and D₂18O. *Journal of Quantitative Spectroscopy and Radiative Transfer* 142, 93-108 (2014).
32. Ch'ng, L.C., Samanta, A.K., Czako, G., Bowman, J.M., Reisler, H., Experimental and Theoretical Investigations of Energy Transfer and Hydrogen-Bond Breaking in the Water Dimer. *J. Am. Chem. Soc.* 134(37), 15430-15435 (2012).
33. Rocher-Casterline, B.E., Ch'ng, L.C., Mollner, A.K., Reisler, H., Communication: Determination of the Bond Dissociation Energy (D₀) of the Water Dimer, (H₂O)₂, by Velocity Map Imaging. *J. Chem. Phys.* 134(21), 211101 (2011).
34. Lo Nostro, P., Ninham, B.W., Hofmeister Phenomena: An Update on Ion Specificity in Biology. *Chem. Rev. (Washington, DC, U. S.)* 112(4), 2286-2322 (2012).
35. Jungwirth, P., Cremer, P.S., Beyond Hofmeister. *Nature Chemistry* 6, 261 (2014).
36. Okur, H.I., *et al.*, Beyond the Hofmeister Series: Ion-Specific Effects on Proteins and Their Biological Functions. *J. Phys. Chem. B* 121(9), 1997-2014 (2017).
37. Smith, J.D., Saykally, R.J., Geissler, P.L., The Effects of Dissolved Halide Anions on Hydrogen Bonding in Liquid Water. *J. Am. Chem. Soc.* 129(45), 13847-13856 (2007).
38. Jungwirth, P., Laage, D., Ion-Induced Long-Range Orientational Correlations in Water: Strong or Weak, Physiologically Relevant or Unimportant, and Unique to Water or Not? *J. Phys. Chem. Lett.* 9(8), 2056-2057 (2018).
39. Duignan, T.T., Baer, M.D., Mundy, C.J., Ions Interacting in Solution: Moving from Intrinsic to Collective Properties. *Current Opinion in Colloid & Interface Science* 23, 58-65 (2016).
40. Chen, Y., Dupertuis, N., Okur, H.I., Roke, S., Temperature Dependence of Water-Water and Ion-Water Correlations in Bulk Water and Electrolyte Solutions Probed by Femtosecond Elastic Second Harmonic Scattering. *J. Chem. Phys.* 148(22), 222835 (2018).
41. Chen, Y., *et al.*, Electrolytes Induce Long-Range Orientational Order and Free Energy Changes in the H-Bond Network of Bulk Water. *Sci. Adv.* 2(4), e1501891 (2016).

42. Schröder, A., Berton-Carabin, C., Venema, P., Cornacchia, L., Interfacial Properties of Whey Protein and Whey Protein Hydrolysates and Their Influence on O/W Emulsion Stability. *Food Hydrocolloids* 73, 129-140 (2017).
43. Rout, D., Verma, R., Agarwal, S.K., Polyelectrolyte Treatment — an Approach for Water Quality Improvement. *Water Science and Technology* 40(2), 137-141 (1999).
44. Bolto, B., Gregory, J., Organic Polyelectrolytes in Water Treatment. *Water Research* 41(11), 2301-2324 (2007).
45. Thierry, B., Winnik, F.M., Merhi, Y., Silver, J., Tabrizian, M., Bioactive Coatings of Endovascular Stents Based on Polyelectrolyte Multilayers. *Biomacromolecules* 4(6), 1564-1571 (2003).
46. Lewis, J.A., Matsuyama, H., Kirby, G., Morissette, S., Young, J.F., Polyelectrolyte Effects on the Rheological Properties of Concentrated Cement Suspensions. *Journal of the American Ceramic Society* 83(8), 1905-1913 (2000).
47. Theocharis, A.D., Skandalis, S.S., Gialeli, C., Karamanos, N.K., Extracellular Matrix Structure. *Advanced drug delivery reviews* 97, 4-27 (2016).
48. Cowman, M.K., Lee, H.G., Schwertfeger, K.L., McCarthy, J.B., Turley, E.A., The Content and Size of Hyaluronan in Biological Fluids and Tissues. *Frontiers in immunology* 6, 261 (2015).
49. Stick, R.V., Williams, S.J., *Chapter 11 - Glycoproteins and Proteoglycans*, in *Carbohydrates: The Essential Molecules of Life (Second Edition)*, R.V. Stick, S.J. Williams, Editors. 2009, Elsevier: Oxford. p. 369-412.
50. Rice, S.A., Dinner, A.R., *Physical Chemistry of Polyelectrolyte Solutions*. (John Wiley & Sons, 2015).
51. Förster, S., Schmidt, M., *Polyelectrolytes in Solution*, in *Physical Properties of Polymers*. 1995, Springer. p. 51-133.
52. Eisenberg, H., Polyelectrolytes, Thirty Years Later. *Biophysical Chemistry* 7(1), 3-13 (1977).
53. Dobrynin, A.V., Colby, R.H., Rubinstein, M., Scaling Theory of Polyelectrolyte Solutions. *Macromolecules* 28(6), 1859-1871 (1995).
54. Netz, R.R., Andelman, D., Neutral and Charged Polymers at Interfaces. *Physics reports* 380(1), 1-95 (2003).
55. Alberts, B., *et al.*, *Molecular Biology of the Cell. Fourth Edition.*, (Garland Science, New York, 2002).
56. Van Meer, G., Voelker, D.R., Feigenson, G.W., Membrane Lipids: Where They Are and How They Behave. *Nature reviews Molecular cell biology* 9(2), 112-124 (2008).
57. Escribá, P.V., *et al.*, Membranes: A Meeting Point for Lipids, Proteins and Therapies. *Journal of cellular and molecular medicine* 12(3), 829-875 (2008).
58. Israelachvili, J.N., Mitchell, D.J., Ninham, B.W., Theory of Self-Assembly of Lipid Bilayers and Vesicles. *Biochim. Biophys. Acta, Biomembr.* 470(2), 185-201 (1977).
59. Hammer, M.U., Anderson, T.H., Chaimovich, A., Shell, M.S., Israelachvili, J., The Search for the Hydrophobic Force Law. *Faraday discussions* 146, 299-308 (2010).
60. Perera, L., Essmann, U., Berkowitz, M.L., Role of Water in the Hydration Force Acting between Lipid Bilayers. *Langmuir* 12(11), 2625-2629 (1996).
61. Ruiz, M. *Cell Membrane*. [Image] 2007 [cited 2019 11.09.2019]; Available from: https://en.wikipedia.org/wiki/Cell_membrane.
62. Fukuma, T., Higgins, M.J., Jarvis, S.P., Direct Imaging of Individual Intrinsic Hydration Layers on Lipid Bilayers at Ångstrom Resolution. *Biophys. J.* 92(10), 3603-3609 (2007).
63. Higgins, M.J., *et al.*, Structured Water Layers Adjacent to Biological Membranes. *Biophys. J.* 91(7), 2532-2542 (2006).

64. Israelachvili, J.N., Pashley, R.M., Molecular Layering of Water at Surfaces and Origin of Repulsive Hydration Forces. *Nature* 306(5940), 249-250 (1983).
65. Berkowitz, M.L., Bostick, D.L., Pandit, S., Aqueous Solutions Next to Phospholipid Membrane Surfaces: Insights from Simulations. *Chem. Rev. (Washington, DC, U. S.)* 106(4), 1527-1539 (2006).
66. Vácha, R., *et al.*, Mechanism of Interaction of Monovalent Ions with Phosphatidylcholine Lipid Membranes. *J. Phys. Chem. B* 114(29), 9504-9509 (2010).
67. Okur, H.I., Chen, Y., Smolentsev, N., Zdrali, E., Roke, S., Interfacial Structure and Hydration of 3d Lipid Monolayers in Aqueous Solution. *J. Phys. Chem. B* 121(13), 2808-2813 (2017).
68. Dreier, L.B., *et al.*, Saturation of Charge-Induced Water Alignment at Model Membrane Surfaces. *Sci. Adv.* 4(3), (2018).
69. Lütgebaucks, C., Macias-Romero, C., Roke, S., Characterization of the Interface of Binary Mixed Dopc:Dops Liposomes in Water: The Impact of Charge Condensation. *J. Chem. Phys.* 146(4), 044701 (2017).
70. Petrache, H.I., *et al.*, Structure and Fluctuations of Charged Phosphatidylserine Bilayers in the Absence of Salt. *Biophys. J.* 86(3), 1574-1586 (2004).
71. Björneholm, O., *et al.*, Water at Interfaces. *Chem. Rev. (Washington, DC, U. S.)* 116(13), 7698-7726 (2016).
72. Asakawa, H., Yoshioka, S., Nishimura, K.-i., Fukuma, T., Spatial Distribution of Lipid Headgroups and Water Molecules at Membrane/Water Interfaces Visualized by Three-Dimensional Scanning Force Microscopy. *ACS Nano* 6(10), 9013-9020 (2012).
73. Roke, S., Nonlinear Optical Spectroscopy of Soft Matter Interfaces. *ChemPhysChem* 10(9-10), 1380-1388 (2009).
74. Roke, S., Nonlinear Spectroscopy of Bio-Interfaces. *International Journal of Materials Research* 102(7), 906-912 (2011).
75. Okur, H.I., Tarun, O.B., Roke, S., Chemistry of Lipid Membranes from Models to Living Systems: A Perspective of Hydration, Surface Potential, Curvature, Confinement and Heterogeneity. *J. Am. Chem. Soc.* 141(31), 12168-12181 (2019).
76. Lütgebaucks, C., Gonella, G., Roke, S., Optical Label-Free and Model-Free Probe of the Surface Potential of Nanoscale and Microscopic Objects in Aqueous Solution. *Phys. Rev. B* 94(19), 195410 (2016).
77. Zdrali, E., Chen, Y., Okur, H.I., Wilkins, D.M., Roke, S., The Molecular Mechanism of Nanodroplet Stability. *ACS nano* 11(12), 12111-12120 (2017).
78. Kovacik, F., Okur, H.I., Smolentsev, N., Scheu, R., Roke, S., Hydration Mediated Interfacial Transitions on Mixed Hydrophobic/Hydrophilic Nanodroplet Interfaces. *J. Chem. Phys.* 149(23), 234704 (2018).
79. Tarun, O.B., Hanneschläger, C., Pohl, P., Roke, S., Label-Free and Charge-Sensitive Dynamic Imaging of Lipid Membrane Hydration on Millisecond Time Scales. *Proc. Natl. Acad. Sci. U. S. A.* 115(16), 4081-4086 (2018).
80. Zdrali, E., Baer, M.D., Okur, H.I., Mundy, C.J., Roke, S., The Diverse Nature of Ion Speciation at the Nanoscale Hydrophobic/Water Interface. *J. Phys. Chem. B* 123(10), 2414-2423 (2019).
81. Zdrali, E., Okur, H.I., Roke, S., Specific Ion Effects at the Interface of Nanometer-Sized Droplets in Water: Structure and Stability. *J. Phys. Chem. C* 123(27), 16621-16630 (2019).
82. Smolentsev, N., Lütgebaucks, C., Okur, H.I., de Beer, A.G.F., Roke, S., Intermolecular Headgroup Interaction and Hydration as Driving Forces for Lipid Transmembrane Asymmetry. *J. Am. Chem. Soc.* 138(12), 4053-4060 (2016).
83. Zhao, H., Lappalainen, P., A Simple Guide to Biochemical Approaches for Analyzing Protein-Lipid Interactions. *Mol Biol Cell* 23(15), 2823-2830 (2012).

84. Levy, Y., Onuchic, J.N., Water Mediation in Protein Folding and Molecular Recognition. *Annu. Rev. Biophys. Biomol. Struct.* 35(1), 389-415 (2006).
85. Yan, E.C.Y., Wang, Z., Fu, L., Proteins at Interfaces Probed by Chiral Vibrational Sum Frequency Generation Spectroscopy. *J. Phys. Chem. B* 119(7), 2769-2785 (2015).
86. Yan, E.C.Y., Fu, L., Wang, Z., Liu, W., Biological Macromolecules at Interfaces Probed by Chiral Vibrational Sum Frequency Generation Spectroscopy. *Chem. Rev. (Washington, DC, U. S.)* 114(17), 8471-8498 (2014).
87. Siontorou, C.G., Nikoleli, G.-P., Nikolelis, D.P., Karapetis, S.K., Artificial Lipid Membranes: Past, Present, and Future. *Membranes* 7(3), 38 (2017).
88. Liljeblad, J.F.D., Bulone, V., Tyrode, E., Rutland, M.W., Johnson, C.M., Phospholipid Monolayers Probed by Vibrational Sum Frequency Spectroscopy: Instability of Unsaturated Phospholipids. *Biophys. J.* 98(10), L50-L52 (2010).
89. Liu, J., Conboy, J.C., Structure of a Gel Phase Lipid Bilayer Prepared by the Langmuir–Blodgett/Langmuir-Schaefer Method Characterized by Sum-Frequency Vibrational Spectroscopy. *Langmuir* 21(20), 9091-9097 (2005).
90. Wah, B., *et al.*, Reconciling Differences between Lipid Transfer in Free-Standing and Solid Supported Membranes: A Time Resolved Small Angle Neutron Scattering Study. *Langmuir*, (2017).
91. McMahon, H.T., Boucrot, E., Membrane Curvature at a Glance. *Journal of Cell Science* 128(6), 1065 (2015).
92. Drin, G., Antonny, B., Amphipathic Helices and Membrane Curvature. *FEBS letters* 584(9), 1840-1847 (2010).
93. Goebel, A., Lunkenheimer, K., Interfacial Tension of the Water/N-Alkane Interface. *Langmuir* 13(2), 369-372 (1997).
94. Backus, E.H.G., Bonn, D., Cantin, S., Roke, S., Bonn, M., Laser-Heating-Induced Displacement of Surfactants on the Water Surface. *J. Phys. Chem. B* 116(9), 2703-2712 (2012).
95. Rothman, J., Lenard, J., Membrane Asymmetry. *Science* 195(4280), 743-753 (1977).
96. Doktorova, M., *et al.*, Preparation of Asymmetric Phospholipid Vesicles for Use as Cell Membrane Models. *Nature Protocols* 13(9), 2086-2101 (2018).
97. Marquardt, D., Geier, B., Pabst, G., Asymmetric Lipid Membranes: Towards More Realistic Model Systems. *Membranes* 5(2), 180-196 (2015).
98. Zidovetzki, R., Levitan, I., Use of Cyclodextrins to Manipulate Plasma Membrane Cholesterol Content: Evidence, Misconceptions and Control Strategies. *Biochim. Biophys. Acta, Biomembr.* 1768(6), 1311-1324 (2007).
99. Loftsson, T., Brewster, M.E., Pharmaceutical Applications of Cyclodextrins. 1. Drug Solubilization and Stabilization. *Journal of Pharmaceutical Sciences* 85(10), 1017-1025 (1996).
100. Kurkov, S.V., Loftsson, T., Cyclodextrins. *International Journal of Pharmaceutics* 453(1), 167-180 (2013).
101. Crini, G., *et al.*, Fundamentals and Applications of Cyclodextrins. *Cyclodextrin Fundamentals, Reactivity and Analysis*, 1-55 (2018).
102. Boyd, R.W., *Nonlinear Optics*. (Elsevier, Amsterdam, 2008).
103. Long, D.A., *Classical Theory of Rayleigh and Raman Scattering*, in *The Raman Effect*. 2002, John Wiley & Sons Ltd. p. 31-48.
104. de Aguiar, H.B., Scheu, R., Jena, K.C., de Beer, A.G., Roke, S., Comparison of Scattering and Reflection Sfg: A Question of Phase-Matching. *Phys. Chem. Chem. Phys.* 14, 6826-6832 (2012).
105. Franken, e.P., Hill, A.E., Peters, C., Weinreich, G., Generation of Optical Harmonics. *Phys. Rev. Lett.* 7(4), 118 (1961).

106. Maiman, T.H., Stimulated Optical Radiation in Ruby. (1960).
107. Bloembergen, N., Pershan, P.S., Light Waves at the Boundary of Nonlinear Media. *Physical Review* 128(2), 606-622 (1962).
108. Bloembergen, N., Chang, R.K., Jha, S., Lee, C., Optical Second-Harmonic Generation in Reflection from Media with Inversion Symmetry. *Physical Review* 174(3), 813 (1968).
109. Wang, C.C., Second-Harmonic Generation of Light at the Boundary of an Isotropic Medium. *Physical Review* 178(3), 1457 (1969).
110. Guyot-Sionnest, P., Chen, W., Shen, Y., General Considerations on Optical Second-Harmonic Generation from Surfaces and Interfaces. *Phys. Rev. B* 33(12), 8254 (1986).
111. Chen, J.M., Bower, J.R., Wang, C.S., Lee, C.H., Optical Second-Harmonic Generation from Submonolayer Na-Covered Ge Surfaces. *Optics Communications* 9(2), 132-134 (1973).
112. Heinz, T., Tom, H., Shen, Y.R., Determination of Molecular Orientation of Monolayer Adsorbates by Optical Second-Harmonic Generation. *Physical Review A* 28(3), 1883 (1983).
113. Hicks, J., Kemnitz, K., Eisenthal, K., Heinz, T., Studies of Liquid Surfaces by Second Harmonic Generation. *J. Phys. Chem.* 90(4), 560-562 (1986).
114. Shen, Y., Surface Properties Probed by Second-Harmonic and Sum-Frequency Generation. *Nature* 337(6207), 519 (1989).
115. Ong, S., Zhao, X., Eisenthal, K.B., Polarization of Water Molecules at a Charged Interface: Second Harmonic Studies of the Silica/Water Interface. *Chem. Phys. Lett.* 191(3), 327-335 (1992).
116. Zhu, X., Suhr, H., Shen, Y., Surface Vibrational Spectroscopy by Infrared-Visible Sum Frequency Generation. *Phys. Rev. B* 35(6), 3047 (1987).
117. Hunt, J., Guyot-Sionnest, P., Shen, Y., Observation of CH Stretch Vibrations of Monolayers of Molecules Optical Sum-Frequency Generation. *Chem. Phys. Lett.* 133(3), 189-192 (1987).
118. McGuire, J.A., Shen, Y.R., Ultrafast Vibrational Dynamics at Water Interfaces. *Science* 313(5795), 1945-1948 (2006).
119. Ji, N., Ostroverkhov, V., Chen, C.-Y., Shen, Y.-R., Phase-Sensitive Sum-Frequency Vibrational Spectroscopy and Its Application to Studies of Interfacial Alkyl Chains. *J. Am. Chem. Soc.* 129(33), 10056-10057 (2007).
120. Singh, P.C., Nihonyanagi, S., Yamaguchi, S., Tahara, T., Ultrafast Vibrational Dynamics of Water at a Charged Interface Revealed by Two-Dimensional Heterodyne-Detected Vibrational Sum Frequency Generation. *J. Chem. Phys.* 137(9), 094706 (2012).
121. McDermott, M.L., Vanselous, H., Corcelli, S.A., Petersen, P.B., Dna's Chiral Spine of Hydration. *ACS Cent. Sci.* 3(7), 708-714 (2017).
122. Kocsis, I., *et al.*, Oriented Chiral Water Wires in Artificial Transmembrane Channels. *Sci. Adv.* 4(3), eaao5603 (2018).
123. Fu, L., Liu, J., Yan, E.C.Y., Chiral Sum Frequency Generation Spectroscopy for Characterizing Protein Secondary Structures at Interfaces. *J. Am. Chem. Soc.* 133(21), 8094-8097 (2011).
124. Terhune, R.W., Maker, P.D., Savage, C.M., Measurements of Nonlinear Light Scattering. *Phys. Rev. Lett.* 14(17), 681-684 (1965).
125. Wang, H., Yan, E.C.Y., Borguet, E., Eisenthal, K.B., Second Harmonic Generation from the Surface of Centrosymmetric Particles in Bulk Solution. *Chem. Phys. Lett.* 259(1), 15-20 (1996).
126. Roke, S., *et al.*, Vibrational Sum Frequency Scattering from a Submicron Suspension. *Phys. Rev. Lett.* 91(25), 258302 (2003).
127. Yan, E.C.Y., Liu, Y., Eisenthal, K.B., New Method for Determination of Surface Potential of Microscopic Particles by Second Harmonic Generation. *J. Phys. Chem. B* 102(33), 6331-6336 (1998).

128. Liu, Y., Yan, E.C.Y., Zhao, X., Eienthal, K.B., Surface Potential of Charged Liposomes Determined by Second Harmonic Generation. *Langmuir* 17(7), 2063-2066 (2001).
129. Schürer, B., Wunderlich, S., Sauerbeck, C., Peschel, U., Peukert, W., Probing Colloidal Interfaces by Angle-Resolved Second Harmonic Light Scattering. *Phys. Rev. B* 82(24), 241404 (2010).
130. Scheu, R., Chen, Y., Subinya, M., Roke, S., Stern Layer Formation Induced by Hydrophobic Interactions: A Molecular Level Study. *J. Am. Chem. Soc.* 135(51), 19330-19335 (2013).
131. Scheu, R.d., *et al.*, Specific Ion Effects in Amphiphile Hydration and Interface Stabilization. *J. Am. Chem. Soc.* 136(5), 2040-2047 (2014).
132. Scheu, R., *et al.*, Charge Asymmetry at Aqueous Hydrophobic Interfaces and Hydration Shells. *Angew. Chem.* 126(36), 9714-9717 (2014).
133. Schürer, B., *et al.*, Second Harmonic Light Scattering from Spherical Polyelectrolyte Brushes. *J. Phys. Chem. C* 115(37), 18302-18309 (2011).
134. Sauerbeck, C., Braunschweig, B., Peukert, W., Surface Charging and Interfacial Water Structure of Amphoteric Colloidal Particles. *J. Phys. Chem. C* 118(19), 10033-10042 (2014).
135. Chen, Y., Jena, K.C., Lütgebaucks, C., Okur, H.I., Roke, S., Three Dimensional Nano "Langmuir Trough" for Lipid Studies. *Nano letters* 15(8), 5558-5563 (2015).
136. Chen, Y., Jena, K.C., Roke, S., From Hydrophobic to Hydrophilic: The Structure and Density of the Hexadecane Droplet/Alkanol/Water Interface. *J. Phys. Chem. C* 119(31), 17725-17734 (2015).
137. Gonella, G., Lütgebaucks, C., de Beer, A.G.F., Roke, S., Second Harmonic and Sum-Frequency Generation from Aqueous Interfaces Is Modulated by Interference. *J. Phys. Chem. C* 120(17), 9165-9173 (2016).
138. Zdrali, E., Etienne, G., Smolentsev, N., Amstad, E., Roke, S., The Interfacial Structure of Nano- and Micron-Sized Oil and Water Droplets Stabilized with Sds and Span80. *J. Chem. Phys.* 150(20), 204704 (2019).
139. Olenick, L.L., *et al.*, Polycation Interactions with Zwitterionic Phospholipid Monolayers on Oil Nanodroplet Suspensions in Water (D2o) Probed by Sum Frequency Scattering. *J. Phys. Chem. B* 122(19), 5049-5056 (2018).
140. Chen, Y., Okur, H.I., Lütgebaucks, C., Roke, S., Zwitterionic and Charged Lipids Form Remarkably Different Structures on Nanoscale Oil Droplets in Aqueous Solution. *Langmuir*, (2017).
141. Eienthal, K.B., Liquid Interfaces Probed by Second-Harmonic and Sum-Frequency Spectroscopy. *Chem. Rev. (Washington, DC, U. S.)* 96(4), 1343-1360 (1996).
142. Eienthal, K.B., Second Harmonic Spectroscopy of Aqueous Nano- and Microparticle Interfaces. *Chem. Rev. (Washington, DC, U. S.)* 106(4), 1462-1477 (2006).
143. Roke, S., Gonella, G., Nonlinear Light Scattering and Spectroscopy of Particles and Droplets in Liquids. *Annu. Rev. Phys. Chem.* 63, 353-378 (2012).
144. Tran, R.J., Sly, K.L., Conboy, J.C., Applications of Surface Second Harmonic Generation in Biological Sensing. *Annu. Rev. Anal. Chem.* 10, 387-414 (2017).
145. Cyvin, S.J., Rauch, J.E., Decius, J.C., Theory of Hyper-Raman Effects (Nonlinear Inelastic Light Scattering): Selection Rules and Depolarization Ratios for the Second-Order Polarizability. *J. Chem. Phys.* 43(11), 4083-4095 (1965).
146. Bersohn, R., Pao, Y.H., Frisch, H., Double-Quantum Light Scattering by Molecules. *J. Chem. Phys.* 45(9), 3184-3198 (1966).
147. Kauranen, M., Persoons, A., Theory of Polarization Measurements of Second-Order Nonlinear Light Scattering. *J. Chem. Phys.* 104(10), 3445-3456 (1996).
148. Clays, K., Persoons, A., Hyper-Rayleigh Scattering in Solution. *Phys. Rev. Lett.* 66(23), 2980-2983 (1991).

149. Chen, Y., Okur, H.I., Liang, C., Roke, S., Orientational Ordering of Water in Extended Hydration Shells of Cations Is Ion-Specific and Is Correlated Directly with Viscosity and Hydration Free Energy. *Phys. Chem. Chem. Phys.* 19(36), 24678-24688 (2017).
150. Tocci, G., Liang, C., Wilkins, D.M., Roke, S., Ceriotti, M., Second-Harmonic Scattering as a Probe of Structural Correlations in Liquids. *J. Phys. Chem. Lett.* 7(21), 4311-4316 (2016).
151. Liang, C., *et al.*, Solvent Fluctuations and Nuclear Quantum Effects Modulate the Molecular Hyperpolarizability of Water. *Phys. Rev. B* 96(4), 041407 (2017).
152. Wilkins, D.M., Manolopoulos, D.E., Roke, S., Ceriotti, M., Communication: Mean-Field Theory of Water-Water Correlations in Electrolyte Solutions. *J. Chem. Phys.* 146(18), 181103 (2017).
153. Roke, S., Bonn, M., Petukhov, A.V., Nonlinear Optical Scattering: The Concept of Effective Susceptibility. *Phys. Rev. B* 70(11), 115106 (2004).
154. Landau, L.D., *et al.*, *Electrodynamics of Continuous Media*. (elsevier, 2013), vol. 8.
155. Mie, G., Contributions to the Optics of Turbid Media, Particularly of Colloidal Metal Solutions. *Ann. Phys.(Leipzig)* 25(3), 377-445 (1908).
156. de Beer, A.G., Roke, S., Nonlinear Mie Theory for Second-Harmonic and Sum-Frequency Scattering. *Phys. Rev. B* 79(15), 155420 (2009).
157. Pavlyukh, Y., Hübner, W., Nonlinear Mie Scattering from Spherical Particles. *Phys. Rev. B* 70(24), 245434 (2004).
158. Dewitz, J.P., Hübner, W., Bennemann, K.H., Theory for Nonlinear Mie-Scattering from Spherical Metal Clusters. *Zeitschrift für Physik D Atoms, Molecules and Clusters* 37(1), 75-84 (1996).
159. Hulst, H.C., van de Hulst, H.C., *Light Scattering by Small Particles*. (Courier Corporation, 1957).
160. de Beer, A.G.F., Roke, S., Sum Frequency Generation Scattering from the Interface of an Isotropic Particle: Geometrical and Chiral Effects. *Phys. Rev. B* 75(24), 245438 (2007).
161. Bishop, D.M., *Group Theory and Chemistry*. (Courier Corporation, 1993).
162. de Beer, A.G., Roke, S., Dadap, J.I., Theory of Optical Second-Harmonic and Sum-Frequency Scattering from Arbitrarily Shaped Particles. *JOSA B* 28(6), 1374-1384 (2011).
163. Bishop, D.M., Kirtman, B., Kurtz, H.A., Rice, J.E., Calculation of Vibrational Dynamic Hyperpolarizabilities for H₂O, CO₂, and NH₃. *J. Chem. Phys.* 98(10), 8024-8030 (1993).
164. de Beer, A.G.F., Campen, R.K., Roke, S., Separating Surface Structure and Surface Charge with Second-Harmonic and Sum-Frequency Scattering. *Phys. Rev. B* 82(23), (2010).
165. Oshima, H., *Theory of Colloid and Interfacial Phenomena*, 2006, Academic Press New York.
166. Dadap, J.I., Optical Second-Harmonic Scattering from Cylindrical Particles. *Phys. Rev. B* 78(20), 205322 (2008).
167. Landau, L., Lifshitz, E., *Classical Mechanics*. (Pergamon Press, Oxford, UK, 1960).
168. De Beer, A., De Aguiar, H., Nijssen, J., Roke, S., Detection of Buried Microstructures by Nonlinear Light Scattering Spectroscopy. *Phys. Rev. Lett.* 102(9), 095502 (2009).
169. Palmer, C.A., Loewen, E.G., *Diffraction Grating Handbook*. (Thermo RGL New York, 2002), vol. 5.
170. De Aguiar, H.B., Strader, M.L., de Beer, A.G., Roke, S., Surface Structure of Sodium Dodecyl Sulfate Surfactant and Oil at the Oil-in-Water Droplet Liquid/Liquid Interface: A Manifestation of a Nonequilibrium Surface State. *J. Phys. Chem. B* 115(12), 2970-2978 (2011).
171. Guyot-Sionnest, P., Hunt, J., Shen, Y., Sum-Frequency Vibrational Spectroscopy of a Langmuir Film: Study of Molecular Orientation of a Two-Dimensional System. *Phys. Rev. Lett.* 59(14), 1597 (1987).

172. Gomopoulos, N., Lütgebaucks, C., Sun, Q., Macias-Romero, C., Roke, S., Label-Free Second Harmonic and Hyper Rayleigh Scattering with High Efficiency. *Opt. Express* 21(1), 815-821 (2013).
173. Pecora, R., *Dynamic Light Scattering: Applications of Photon Correlation Spectroscopy*. (Springer Science & Business Media, 2013).
174. Atkins, P., De Paula, J., Keeler, J., *Atkins' Physical Chemistry*. (Oxford university press, 2018).
175. Hunter, R.J., *Zeta Potential in Colloid Science: Principles and Applications*. (Academic press, San Diego, USA, 2013), vol. 2.
176. Lyklema, J., Electrokinetics after Smoluchowski. *Colloids and Surfaces A: Physicochemical and Engineering Aspects* 222(1), 5-14 (2003).
177. Bellissent-Funel, M.-C., *et al.*, Water Determines the Structure and Dynamics of Proteins. *Chem. Rev. (Washington, DC, U. S.)* 116(13), 7673-7697 (2016).
178. Zhang, L., *et al.*, Mapping Hydration Dynamics around a Protein Surface. *Proc. Natl. Acad. Sci. U. S. A.* 104(47), 18461-18466 (2007).
179. Briscoe, W.H., *et al.*, Boundary Lubrication under Water. *Nature* 444(7116), 191-194 (2006).
180. Fraser, J., Laurent, T., Laurent, U., Hyaluronan: Its Nature, Distribution, Functions and Turnover. *Journal of internal medicine* 242(1), 27-33 (1997).
181. Seror, J., *et al.*, Normal and Shear Interactions between Hyaluronan–Aggrecan Complexes Mimicking Possible Boundary Lubricants in Articular Cartilage in Synovial Joints. *Biomacromolecules* 13(11), 3823-3832 (2012).
182. Moreland, L.W., Intra-Articular Hyaluronan (Hyaluronic Acid) and Hylans for the Treatment of Osteoarthritis: Mechanisms of Action. *Arthritis Research & Therapy* 5(2), 54-67 (2003).
183. Mráček, A., *et al.*, The Influence of Hofmeister Series Ions on Hyaluronan Swelling and Viscosity. *Molecules* 13(5), 1025 (2008).
184. Albersdörfer, A., Sackmann, E., Swelling Behavior and Viscoelasticity of Ultrathin Grafted Hyaluronic Acid Films. *The European Physical Journal B-Condensed Matter and Complex Systems* 10(4), 663-672 (1999).
185. Shah, C.B., Barnett, S.M., Swelling Behavior of Hyaluronic Acid Gels. *Journal of applied polymer science* 45(2), 293-298 (1992).
186. Cohen, M., Klein, E., Geiger, B., Addadi, L., Organization and Adhesive Properties of the Hyaluronan Pericellular Coat of Chondrocytes and Epithelial Cells. *Biophys. J.* 85(3), 1996-2005 (2003).
187. Cohen, M., Joester, D., Sabanay, I., Addadi, L., Geiger, B., Hyaluronan in the Pericellular Coat: An Additional Layer of Complexity in Early Cell Adhesion Events. *Soft Matter* 3(3), 327 (2007).
188. Benz, M., Chen, N., Israelachvili, J., Lubrication and Wear Properties of Grafted Polyelectrolytes, Hyaluronan and Hylan, Measured in the Surface Forces Apparatus. *Journal of Biomedical Materials Research Part A: An Official Journal of The Society for Biomaterials, The Japanese Society for Biomaterials, and The Australian Society for Biomaterials and the Korean Society for Biomaterials* 71(1), 6-15 (2004).
189. Seror, J., *et al.*, Articular Cartilage Proteoglycans as Boundary Lubricants: Structure and Frictional Interaction of Surface-Attached Hyaluronan and Hyaluronan–Aggrecan Complexes. *Biomacromolecules* 12(10), 3432-3443 (2011).
190. Joshi, H.N., Topp, E.M., Hydration in Hyaluronic Acid and Its Esters Using Differential Scanning Calorimetry. *International Journal of Pharmaceutics* 80(1), 213-225 (1992).
191. Liu, J., Cowman, M., Thermal Analysis of Semi-Dilute Hyaluronan Solutions. *Journal of thermal analysis and calorimetry* 59(1-2), 547-557 (2000).

192. Servaty, R., Schiller, J., Binder, H., Arnold, K., Hydration of Polymeric Components of Cartilage—an Infrared Spectroscopic Study on Hyaluronic Acid and Chondroitin Sulfate. *International Journal of Biological Macromolecules* 28(2), 121-127 (2001).
193. Maréchal, Y., Milas, M., Rinaudo, M., Hydration of Hyaluronan Polysaccharide Observed by Ir Spectrometry. Iii. Structure and Mechanism of Hydration. *Biopolymers* 72(3), 162-173 (2003).
194. Hunger, J., Bernecker, A., Bakker, H.J., Bonn, M., Richter, R.P., Hydration Dynamics of Hyaluronan and Dextran. *Biophys. J.* 103(1), L10-L12 (2012).
195. Davies, A., Gormally, J., Wyn-Jones, E., Wedlock, D., Phillips, G., A Study of Factors Influencing Hydration of Sodium Hyaluronate from Compressibility and High-Precision Densimetric Measurements. *Biochemical Journal* 213(2), 363-369 (1983).
196. Dedic, J., Okur, H.I., Roke, S., Polyelectrolytes Induce Water-Water Correlations That Result in Dramatic Viscosity Changes and Nuclear Quantum Effects. *Sci. Adv.* 5(12), eaay1443 (2019).
197. Laage, D., Stirnemann, G., Sterpone, F., Rey, R., Hynes, J.T., Reorientation and Allied Dynamics in Water and Aqueous Solutions. *Annual review of physical chemistry* 62, 395-416 (2011).
198. Bakker, H., Structural Dynamics of Aqueous Salt Solutions. *Chem. Rev. (Washington, DC, U. S.)* 108(4), 1456-1473 (2008).
199. Funkner, S., *et al.*, Watching the Low-Frequency Motions in Aqueous Salt Solutions: The Terahertz Vibrational Signatures of Hydrated Ions. *J. Am. Chem. Soc.* 134(2), 1030-1035 (2012).
200. Buchner, R., Hefter, G.T., May, P.M., Dielectric Relaxation of Aqueous NaCl Solutions. *J. Phys. Chem. A* 103(1), 1-9 (1999).
201. Mancinelli, R., Botti, A., Bruni, F., Ricci, M.A., Soper, A.K., Perturbation of Water Structure Due to Monovalent Ions in Solution. *Phys. Chem. Chem. Phys.* 9(23), 2959-2967 (2007).
202. Howell, I., Neilson, G., Hydration in Concentrated Aqueous Solution. *Journal of Physics: Condensed Matter* 8(25), 4455 (1996).
203. Tielrooij, K.J., Garcia-Araez, N., Bonn, M., Bakker, H.J., Cooperativity in Ion Hydration. *Science* 328(5981), 1006-1009 (2010).
204. Stirnemann, G., Wernersson, E., Jungwirth, P., Laage, D., Mechanisms of Acceleration and Retardation of Water Dynamics by Ions. *J. Am. Chem. Soc.* 135(32), 11824-11831 (2013).
205. Pluharova, E., Jungwirth, P., Matubayasi, N., Marsalek, O., Structure and Dynamics of the Hydration Shell: Spatially Decomposed Time Correlation Approach. *Journal of Chemical Theory and Computation*, (2018).
206. Duboisset, J., Brevet, P.-F., Salt-Induced Long-to-Short Range Orientational Transition in Water. *Phys. Rev. Lett.* 120(26), 263001 (2018).
207. Gaiduk, A.P., Galli, G., Local and Global Effects of Dissolved Sodium Chloride on the Structure of Water. *J. Phys. Chem. Lett.* 8(7), 1496-1502 (2017).
208. Belloni, L., Borgis, D., Levesque, M., Screened Coulombic Orientational Correlations in Dilute Aqueous Electrolytes. *J. Phys. Chem. Lett.* 9(8), 1985-1989 (2018).
209. Borgis, D., Belloni, L., Levesque, M., What Does Second Harmonic Scattering Measure in Diluted Electrolytes? *J. Phys. Chem. Lett.*, (2018).
210. Okur, H.I., Chen, Y., Wilkins, D.M., Roke, S., The Jones-Ray Effect Reinterpreted: Surface Tension Minima of Low Ionic Strength Electrolyte Solutions Are Caused by Electric Field Induced Water-Water Correlations. *Chem. Phys. Lett.* 684(Supplement C), 433-442 (2017).
211. Okur, H.I., Drexler, C.I., Tyrode, E.C., Cremer, P.S., Roke, S., The Jones-Ray Effect Is Not Caused by Surface Active Impurities. *J. Phys. Chem. Lett.*, (2018).
212. Skolnick, J., Fixman, M., Electrostatic Persistence Length of a Wormlike Polyelectrolyte. *Macromolecules* 10(5), 944-948 (1977).

213. Odijk, T., Polyelectrolytes near the Rod Limit. *Journal of Polymer Science: Polymer Physics Edition* 15(3), 477-483 (1977).
214. Dadap, J.I., Shan, J., Heinz, T.F., Theory of Optical Second-Harmonic Generation from a Sphere of Centrosymmetric Material: Small-Particle Limit. *J. Opt. Soc. Am. B* 21(7), 1328-1347 (2004).
215. Manning, G.S., Limiting Laws and Counterion Condensation in Polyelectrolyte Solutions I. Colligative Properties. *J. Chem. Phys.* 51(3), 924-933 (1969).
216. De Gennes, P.-G.d., Pincus, P., Velasco, R., Brochard, F., Remarks on Polyelectrolyte Conformation. *Journal de physique* 37(12), 1461-1473 (1976).
217. Le Bret, M., Electrostatic Contribution to the Persistence Length of a Polyelectrolyte. *J. Chem. Phys.* 76(12), 6243-6255 (1982).
218. Degiorgio, V., Bellini, T., Mantegazza, F., Measurements of the Persistence Length of Flexible Polyelectrolytes. *International Journal of Polymer Analysis and Characterization* 2(1), 83-93 (1995).
219. Barrat, J.-L., Joanny, J.-F., Persistence Length of Polyelectrolyte Chains. *EPL (Europhysics Letters)* 24(5), 333 (1993).
220. Buhler, E., Boué, F., Persistence Length for a Model Semirigid Polyelectrolyte as Seen by Small Angle Neutron Scattering: A Relevant Variation of the Lower Bound with Ionic Strength. *The European Physical Journal E* 10(2), 89-92 (2003).
221. Maréchal, Y., The Molecular Structure of Liquid Water Delivered by Absorption Spectroscopy in the Whole Ir Region Completed with Thermodynamics Data. *J. Mol. Sci.* 1004(1), 146-155 (2011).
222. Xu, C., Shear, J.B., Webb, W.W., Hyper-Rayleigh and Hyper-Raman Scattering Background of Liquid Water in Two-Photon Excited Fluorescence Detection. *Analytical Chemistry* 69(7), 1285-1287 (1997).
223. Maurice, A., *et al.*, *Hyper Rayleigh and Hyper Raman from Neat Water*. Spie Nanoscience + Engineering (SPIE, 2014), vol. 9171.
224. Leontidis, E., Hofmeister Anion Effects on Surfactant Self-Assembly and the Formation of Mesoporous Solids. *Current Opinion in Colloid & Interface Science* 7(1), 81-91 (2002).
225. Pal, S.K., Zhao, L., Zewail, A.H., Water at DNA Surfaces: Ultrafast Dynamics in Minor Groove Recognition. *Proc. Natl. Acad. Sci. U. S. A.* 100(14), 8113-8118 (2003).
226. Jayaram, B., Jain, T., The Role of Water in Protein-DNA Recognition. *Annu. Rev. Biophys. Biomol. Struct.* 33, 343-361 (2004).
227. McLaughlin, S., Szabo, G., Eisenman, G., Divalent Ions and the Surface Potential of Charged Phospholipid Membranes. *The Journal of general physiology* 58(6), 667-687 (1971).
228. Raviv, U., *et al.*, Lubrication by Charged Polymers. *Nature* 425(6954), 163-165 (2003).
229. Jenkins, H.D.B., Marcus, Y., Viscosity B-Coefficients of Ions in Solution. *Chem. Rev. (Washington, DC, U. S.)* 95(8), 2695-2724 (1995).
230. Kunz, W., *Specific Ion Effects*. (World Scientific, 2010).
231. Waluyo, I., *et al.*, A Different View of Structure-Making and Structure-Breaking in Alkali Halide Aqueous Solutions through X-Ray Absorption Spectroscopy. *J. Chem. Phys.* 140(24), 244506 (2014).
232. Soper, A.K., Weckström, K., Ion Solvation and Water Structure in Potassium Halide Aqueous Solutions. *Biophysical Chemistry* 124(3), 180-191 (2006).
233. Sun, Q., Raman Spectroscopic Study of the Effects of Dissolved NaCl on Water Structure. *Vibrational Spectroscopy* 62, 110-114 (2012).
234. Li, R., Jiang, Z., Chen, F., Yang, H., Guan, Y., Hydrogen Bonded Structure of Water and Aqueous Solutions of Sodium Halides: A Raman Spectroscopic Study. *J. Mol. Sci.* 707(1), 83-88 (2004).

235. Kondoh, M., Ohshima, Y., Tsubouchi, M., Ion Effects on the Structure of Water Studied by Terahertz Time-Domain Spectroscopy. *Chem. Phys. Lett.* 591, 317-322 (2014).
236. Hribar, B., Southall, N.T., Vlachy, V., Dill, K.A., How Ions Affect the Structure of Water. *J. Am. Chem. Soc.* 124(41), 12302-12311 (2002).
237. Kunz, W., Specific Ion Effects in Liquids, in Biological Systems, and at Interfaces. *Pure and applied chemistry* 78(8), 1611-1617 (2006).
238. Zhang, Y., Cremer, P.S., Chemistry of Hofmeister Anions and Osmolytes. *Annual Review of Physical Chemistry* 61(1), 63-83 (2010).
239. Li, X.-Z., Walker, B., Michaelides, A., Quantum Nature of the Hydrogen Bond. *Proc. Natl. Acad. Sci. U. S. A.* 108(16), 6369-6373 (2011).
240. Bergmann, U., *et al.*, Isotope Effects in Liquid Water Probed by X-Ray Raman Spectroscopy. *Phys. Rev. B* 76(2), 024202 (2007).
241. Perticaroli, S., *et al.*, Structural Relaxation, Viscosity, and Network Connectivity in a Hydrogen Bonding Liquid. *Phys. Chem. Chem. Phys.* 19(38), 25859-25869 (2017).
242. Cohen, J., Priel, Z., Rabin, Y., Viscosity of Dilute Polyelectrolyte Solutions. *J. Chem. Phys.* 88(11), 7111-7116 (1988).
243. Nishida, K., Kaji, K., Kanaya, T., Theoretical Calculation of Reduced Viscosity of Polyelectrolyte Solutions. *Polymer* 42(21), 8657-8662 (2001).
244. Manning, G.S., The Critical Onset of Counterion Condensation: A Survey of Its Experimental and Theoretical Basis. *Berichte der Bunsengesellschaft für physikalische Chemie* 100(6), 909-922 (1996).
245. Lifson, S., Katchalsky, A., The Electrostatic Free Energy of Polyelectrolyte Solutions. II. Fully Stretched Macromolecules. *Journal of Polymer Science* 13(68), 43-55 (1954).
246. Stevens, M.J., Kremer, K., The Nature of Flexible Linear Polyelectrolytes in Salt Free Solution: A Molecular Dynamics Study. *J. Chem. Phys.* 103(4), 1669-1690 (1995).
247. Eisenberg, H., Pouyet, J., Viscosities of Dilute Aqueous Solutions of a Partially Quaternized Poly-4-Vinylpyridine at Low Gradients of Flow. *Journal of polymer science* 13(68), 85-91 (1954).
248. Antonietti, M., Briel, A., Förster, S., Intrinsic Viscosity of Small Spherical Polyelectrolytes: Proof for the Intermolecular Origin of the Polyelectrolyte Effect. *J. Chem. Phys.* 105(17), 7795-7807 (1996).
249. Nishida, K., Kaji, K., Kanaya, T., Shibano, T., Added Salt Effect on the Intermolecular Correlation in Flexible Polyelectrolyte Solutions: Small-Angle Scattering Study. *Macromolecules* 35(10), 4084-4089 (2002).
250. Fort, R., Moore, W., Viscosities of Binary Liquid Mixtures. *Transactions of the Faraday Society* 62, 1112-1119 (1966).
251. Lamb, W.J., Jonas, J., Nmr Study of Compressed Supercritical Water. *J. Chem. Phys.* 74(2), 913-921 (1981).
252. Cho, C., Urquidi, J., Robinson, G.W., Molecular-Level Description of Temperature and Pressure Effects on the Viscosity of Water. *J. Chem. Phys.* 111(22), 10171-10176 (1999).
253. Pals, D.T.F., Hermans, J.J., Sodium Salts of Pectin and of Carboxy Methyl Cellulose in Aqueous Sodium Chloride. I. Viscosities. *Recueil des Travaux Chimiques des Pays-Bas* 71(5), 433-457 (1952).
254. Shibayama, M., Moriwaki, R., Ikkai, F., Nomura, S., Viscosity Behaviour of Weakly Charged Polymer-Ion Complexes Comprising Poly(Vinyl Alcohol) and Congo Red. *Polymer* 35(26), 5716-5721 (1994).
255. Huggins, M.L., The Viscosity of Dilute Solutions of Long-Chain Molecules. IV. Dependence on Concentration. *J. Am. Chem. Soc.* 64(11), 2716-2718 (1942).

256. Fernandes, A., Martins, R., da Trindade Neto, C., Pereira, M., Fonseca, J., Characterization of Polyelectrolyte Effect in Poly (Acrylic Acid) Solutions. *Journal of applied polymer science* 89(1), 191-196 (2003).
257. Roure, I., Rinaudo, M., Milas, M., Frollini, E., Viscometric Behaviour of Polyelectrolytes in the Presence of Low Salt Concentration. *Polymer* 39(22), 5441-5445 (1998).
258. Cohen, J., Priel, Z., Viscosity of Dilute Polyelectrolyte Solutions: Concentration Dependence on Sodium Chloride, Magnesium Sulfate and Lanthanum Nitrate. *Macromolecules* 22(5), 2356-2358 (1989).
259. Thomas, D., Charlesby, A., Viscosity Relationship in Solutions of Polyethylene Glycols. *Journal of Polymer Science* 42(139), 195-202 (1960).
260. Shulyak, I., Grushova, E., Semenchenko, A., Rheological Properties of Aqueous Solutions of Polyethylene Glycols with Various Molecular Weights. *Russian Journal of Physical Chemistry A* 85(3), 419-422 (2011).
261. Rice, S.A., Kirkwood, J.G., On an Approximate Theory of Transport in Dense Media. *J. Chem. Phys.* 31(4), 901-908 (1959).
262. Habershon, S., Markland, T.E., Manolopoulos, D.E., Competing Quantum Effects in the Dynamics of a Flexible Water Model. *J. Chem. Phys.* 131(2), 024501 (2009).
263. Laage, D., Hynes, J.T., A Molecular Jump Mechanism of Water Reorientation. *Science* 311(5762), 832-835 (2006).
264. Vij, J.K., Simpson, D.R.J., Panarina, O.E., Far Infrared Spectroscopy of Water at Different Temperatures: Ghz to Thz Dielectric Spectroscopy of Water. *Journal of Molecular Liquids* 112(3), 125-135 (2004).
265. Brubach, J.-B., Mermet, A., Filabozzi, A., Gerschel, A., Roy, P., Signatures of the Hydrogen Bonding in the Infrared Bands of Water. *J. Chem. Phys.* 122(18), 184509 (2005).
266. Choi, G.Y., Ulman, A., Shnidman, Y., Zurawsky, W., Fleischer, C., Isotope Effect in Adhesion. *J. Phys. Chem. B* 104(24), 5768-5771 (2000).
267. Chen, A., Wilburn, P., Hao, X., Tully, T., Walking Deficits and Centrophobism in an A-Synuclein Fly Model of Parkinson's Disease. *Genes, Brain Behav.* 13(8), 812-820 (2014).
268. Winner, B., *et al.*, In Vivo Demonstration That A-Synuclein Oligomers Are Toxic. *Proc. Natl. Acad. Sci. U. S. A.* 108(10), 4194-4199 (2011).
269. Galvin, J.E., *et al.*, Pathobiology of the Lewy Body. *Adv. Neurol.* 80, 313-324 (1999).
270. Dev, K.K., Hofele, K., Barbieri, S., Buchman, V.L., van der Putten, H., Part II: A-Synuclein and Its Molecular Pathophysiological Role in Neurodegenerative Disease. *Neuropharmacology* 45(1), 14-44 (2003).
271. Lassen, L.B., Reimer, L., Ferreira, N., Betzer, C., Jensen, P.H., Protein Partners of A-Synuclein in Health and Disease. *Brain. Pathol.* 26(3), 389-397 (2016).
272. Maroteaux, L., Campanelli, J.T., Scheller, R.H., Synuclein: A Neuron-Specific Protein Localized to the Nucleus and Presynaptic Nerve Terminal. *J. Neurosci.* 8(8), 2804-2815 (1988).
273. Iwai, A., *et al.*, The Precursor Protein of Non-A β Component of Alzheimer's Disease Amyloid Is a Presynaptic Protein of the Central Nervous System. *Neuron* 14(2), 467-475 (1995).
274. Eliezer, D., Kutluay, E., Bussell Jr, R., Browne, G., Conformational Properties of A-Synuclein in Its Free and Lipid-Associated States. *J. Mol. Biol.* 307(4), 1061-1073 (2001).
275. Lee, H.-J., Choi, C., Lee, S.-J., Membrane-Bound A-Synuclein Has a High Aggregation Propensity and the Ability to Seed the Aggregation of the Cytosolic Form. *J. Biol. Chem.* 277(1), 671-678 (2002).

276. Perrin, R.J., Woods, W.S., Clayton, D.F., George, J.M., Interaction of Human A-Synuclein and Parkinson's Disease Variants with Phospholipids Structural Analysis Using Site-Directed Mutagenesis. *J. Biol. Chem.* 275(44), 34393-34398 (2000).
277. Kiskis, J., Horvath, I., Wittung-Stafshede, P., Rocha, S., Unraveling Amyloid Formation Paths of Parkinson's Disease Protein A-Synuclein Triggered by Anionic Vesicles. *Q. Rev. Biophys.* 50, (2017).
278. Fusco, G., *et al.*, Direct Observation of the Three Regions in A-Synuclein That Determine Its Membrane-Bound Behaviour. *Nat. Commun.* 5, 3827 (2014).
279. Uluca, B., *et al.*, Dnp-Enhanced Mas Nmr: A Tool to Snapshot Conformational Ensembles of A-Synuclein in Different States. *Biophys. J.* 114(7), 1614-1623 (2018).
280. Jao, C.C., Hegde, B.G., Chen, J., Haworth, I.S., Langen, R., Structure of Membrane-Bound A-Synuclein from Site-Directed Spin Labeling and Computational Refinement. *Proc. Natl. Acad. Sci. U. S. A.*, pnas. 0807826105 (2008).
281. Bodner, C.R., Dobson, C.M., Bax, A., Multiple Tight Phospholipid-Binding Modes of A-Synuclein Revealed by Solution Nmr Spectroscopy. *J. Mol. Biol.* 390(4), 775-790 (2009).
282. Hellstrand, E., *et al.*, Adsorption of A-Synuclein to Supported Lipid Bilayers: Positioning and Role of Electrostatics. *ACS Chem. Neurosci.* 4(10), 1339-1351 (2013).
283. Pfefferkorn, C.M., *et al.*, Depth of A-Synuclein in a Bilayer Determined by Fluorescence, Neutron Reflectometry, and Computation. *Biophys. J.* 102(3), 613-621 (2012).
284. Galvagnion, C., *et al.*, Chemical Properties of Lipids Strongly Affect the Kinetics of the Membrane-Induced Aggregation of A-Synuclein. *Proc. Natl. Acad. Sci. U. S. A.* 113(26), 7065-7070 (2016).
285. Galvagnion, C., *et al.*, Lipid Vesicles Trigger A-Synuclein Aggregation by Stimulating Primary Nucleation. *Nat. Chem. Biol.* 11, 229 (2015).
286. Bussell Jr, R., Eliezer, D., A Structural and Functional Role for 11-Mer Repeats in A-Synuclein and Other Exchangeable Lipid Binding Proteins. *J. Mol. Biol.* 329(4), 763-778 (2003).
287. Ulmer, T.S., Bax, A., Cole, N.B., Nussbaum, R.L., Structure and Dynamics of Micelle-Bound Human A-Synuclein. *J. Biol. Chem.* 280(10), 9595-9603 (2005).
288. Drin, G., Antonny, B., Amphipathic Helices and Membrane Curvature. *FEBS Lett* 584(9), 1840-1847 (2010).
289. Jao, C.C., Der-Sarkissian, A., Chen, J., Langen, R., Structure of Membrane-Bound A-Synuclein Studied by Site-Directed Spin Labeling. *Proc. Natl. Acad. Sci. U. S. A.* 101(22), 8331-8336 (2004).
290. Liu, J., Conboy, J.C., Direct Measurement of the Transbilayer Movement of Phospholipids by Sum-Frequency Vibrational Spectroscopy. *J. Am. Chem. Soc.* 126(27), 8376-8377 (2004).
291. Liu, J., Conboy, J.C., 1, 2-Diacyl-Phosphatidylcholine Flip-Flop Measured Directly by Sum-Frequency Vibrational Spectroscopy. *Biophys. J.* 89(4), 2522-2532 (2005).
292. Verreault, D., Hua, W., Allen, H.C., From Conventional to Phase-Sensitive Vibrational Sum Frequency Generation Spectroscopy: Probing Water Organization at Aqueous Interfaces. *J. Phys. Chem. Lett.* 3(20), 3012-3028 (2012).
293. Johnson, C.M., Baldelli, S., Vibrational Sum Frequency Spectroscopy Studies of the Influence of Solutes and Phospholipids at Vapor/Water Interfaces Relevant to Biological and Environmental Systems. *Chem. Rev. (Washington, DC, U. S.)* 114(17), 8416-8446 (2014).
294. Morsbach, S., *et al.*, Engineering Proteins at Interfaces: From Complementary Characterization to Material Surfaces with Designed Functions. *Angew. Chem., Int. Ed.*, (2018).
295. Troiano, J.M., *et al.*, Quantifying the Electrostatics of Polycation-Lipid Bilayer Interactions. *J. Am. Chem. Soc.* 139(16), 5808-5816 (2017).

296. McGeachy, A., *et al.*, Interfacial Electrostatics of Poly (Vinylamine Hydrochloride), Poly (Diallyldimethylammonium Chloride), Poly-L-Lysine, and Poly-L-Arginine Interacting with Lipid Bilayers. *Phys. Chem. Chem. Phys.* 20(16), 10846-10856 (2018).
297. Pan, J., *et al.*, Molecular Structures of Fluid Phase Phosphatidylglycerol Bilayers as Determined by Small Angle Neutron and X-Ray Scattering. *Biochim. Biophys. Acta, Biomembr.* 1818(9), 2135-2148 (2012).
298. Lide, D.R., *Crc Handbook of Chemistry and Physics*. (CRC press, Boca raton, U.S.A., 2004).
299. de Beer, A.G., Roke, S., Obtaining Molecular Orientation from Second Harmonic and Sum Frequency Scattering Experiments in Water: Angular Distribution and Polarization Dependence. *J. Chem. Phys.* 132(23), 234702 (2010).
300. de Beer, A.G.F., Roke, S., What Interactions Can Distort the Orientational Distribution of Interfacial Water Molecules as Probed by Second Harmonic and Sum Frequency Generation? *J. Chem. Phys.* 145(4), 044705 (2016).
301. Simpson, G.J., Rowlen, K.L., An Shg Magic Angle: Dependence of Second Harmonic Generation Orientation Measurements on the Width of the Orientation Distribution. *J. Am. Chem. Soc.* 121(11), 2635-2636 (1999).
302. Gardiner, C., *et al.*, Measurement of Refractive Index by Nanoparticle Tracking Analysis Reveals Heterogeneity in Extracellular Vesicles. *J. Extracell. Vesicles* 3(1), 25361 (2014).
303. Gubskaya, A., Kusalik, P., The Multipole Polarizabilities and Hyperpolarizabilities of the Water Molecule in Liquid State: An Ab Initio Study. *Molecular Physics* 99(13), 1107-1120 (2001).
304. Dadap, J.I., Shan, J., Eisenthal, K.B., Heinz, T.F., Second-Harmonic Rayleigh Scattering from a Sphere of Centrosymmetric Material. *Phys. Rev. Lett.* 83(20), 4045 (1999).
305. Morar, A.S., Olteanu, A., Young, G.B., Pielak, G.J., Solvent-Induced Collapse of A-Synuclein and Acid-Denatured Cytochrome C. *Protein Sci.* 10(11), 2195-2199 (2001).
306. Dedmon, M.M., Lindorff-Larsen, K., Christodoulou, J., Vendruscolo, M., Dobson, C.M., Mapping Long-Range Interactions in A-Synuclein Using Spin-Label Nmr and Ensemble Molecular Dynamics Simulations. *J. Am. Chem. Soc.* 127(2), 476-477 (2005).
307. Hammoud, Z., *et al.*, Cyclodextrin-Membrane Interaction in Drug Delivery and Membrane Structure Maintenance. *International Journal of Pharmaceutics* 564, 59-76 (2019).
308. Miranda, J.C.d., Martins, T.E.A., Veiga, F., Ferraz, H.G., Cyclodextrins and Ternary Complexes: Technology to Improve Solubility of Poorly Soluble Drugs. *Brazilian Journal of Pharmaceutical Sciences* 47, 665-681 (2011).
309. Griebenow, K., *et al.*, Improved Enzyme Activity and Enantioselectivity in Organic Solvents by Methyl-B-Cyclodextrin. *J. Am. Chem. Soc.* 121(36), 8157-8163 (1999).
310. Ribeiro, A., Figueiras, A., Santos, D., Veiga, F., Preparation and Solid-State Characterization of Inclusion Complexes Formed between Miconazole and Methyl-B-Cyclodextrin. *AAPS PharmSciTech* 9(4), 1102-1109 (2008).
311. Frank, S.G., Inclusion Compounds. *Journal of Pharmaceutical Sciences* 64(10), 1585-1604 (1975).
312. Baek, J.-S., *et al.*, Enhanced Transdermal Drug Delivery of Zaltoprofen Using a Novel Formulation. *International Journal of Pharmaceutics* 453(2), 358-362 (2013).
313. McCormack, B., Gregoriadis, G., Drugs-in-Cyclodextrins-in Liposomes: A Novel Concept in Drug Delivery. *International Journal of Pharmaceutics* 112(3), 249-258 (1994).
314. Markones, M., *et al.*, Engineering Asymmetric Lipid Vesicles: Accurate and Convenient Control of the Outer Leaflet Lipid Composition. *Langmuir* 34(5), 1999-2005 (2018).
315. Leventis, R., Silvius, J.R., Use of Cyclodextrins to Monitor Transbilayer Movement and Differential Lipid Affinities of Cholesterol. *Biophys. J.* 81(4), 2257-2267 (2001).

316. Beseničar, M.P., Bavdek, A., Kladnik, A., Maček, P., Anderluh, G., Kinetics of Cholesterol Extraction from Lipid Membranes by Methyl-B-Cyclodextrin—a Surface Plasmon Resonance Approach. *Biochim. Biophys. Acta, Biomembr.* 1778(1), 175-184 (2008).
317. Nishijo, J., Mizuno, H., Interactions of Cyclodextrins with Dppc Liposomes. Differential Scanning Calorimetry Studies. *Chemical and pharmaceutical bulletin* 46(1), 120-124 (1998).
318. Anderson, T.G., Tan, A., Ganz, P., Seelig, J., Calorimetric Measurement of Phospholipid Interaction with Methyl-B-Cyclodextrin. *Biochemistry* 43(8), 2251-2261 (2004).
319. Sett, R., Paul, B.K., Guchhait, N., Unsaturation of the Phospholipid Side-Chain Influences Its Interaction with Cyclodextrins: A Spectroscopic Exploration Using a Phenazinium Dye. *Colloids and Surfaces B: Biointerfaces*, (2019).
320. Huang, Z., London, E., Effect of Cyclodextrin and Membrane Lipid Structure Upon Cyclodextrin–Lipid Interaction. *Langmuir* 29(47), 14631-14638 (2013).
321. Denz, M., *et al.*, Interaction of Fluorescent Phospholipids with Cyclodextrins. *Chemistry and Physics of Lipids* 194, 37-48 (2016).
322. Puskás, I., Csempesz, F., Influence of Cyclodextrins on the Physical Stability of Dppc-Liposomes. *Colloids and Surfaces B: Biointerfaces* 58(2), 218-224 (2007).
323. Coleman, A.W., Nicolis, I., Keller, N., Dalbiez, J.P., Aggregation of Cyclodextrins: An Explanation of the Abnormal Solubility Of β -Cyclodextrin. *Journal of inclusion phenomena and molecular recognition in chemistry* 13(2), 139-143 (1992).
324. Kluzek, M., Schmutz, M., Marques, C.M., Thalmann, F., Kinetic Evolution of Dopc Lipid Bilayers Exposed to A-Cyclodextrins. *Soft matter* 14(28), 5800-5810 (2018).
325. Tsamaloukas, A., Szadkowska, H., Slotte, P.J., Heerklotz, H., Interactions of Cholesterol with Lipid Membranes and Cyclodextrin Characterized by Calorimetry. *Biophys. J.* 89(2), 1109-1119 (2005).
326. López, C.A., de Vries, A.H., Marrink, S.J., Molecular Mechanism of Cyclodextrin Mediated Cholesterol Extraction. *PLOS Computational Biology* 7(3), e1002020 (2011).
327. Mascetti, J., Castano, S., Cavagnat, D., Desbat, B., Organization of B-Cyclodextrin under Pure Cholesterol, Dmpc, or Dmpg and Mixed Cholesterol/Phospholipid Monolayers. *Langmuir* 24(17), 9616-9622 (2008).
328. López-Nicolás, J.M., Bru, R., Sánchez-Ferrer, A., García-Carmona, F., Use of 'Soluble Lipids' for Biochemical Processes: Linoleic Acid-Cyclodextrin Inclusion Complexes in Aqueous Solutions. *Biochemical Journal* 308(1), 151 (1995).
329. López-Nicolás, J.M., Rodríguez-Bonilla, P., Méndez-Cazorla, L., García-Carmona, F., Physicochemical Study of the Complexation of Pterostilbene by Natural and Modified Cyclodextrins. *Journal of Agricultural and Food Chemistry* 57(12), 5294-5300 (2009).
330. López-Nicolás, J.M., García-Carmona, F., Effect of Hydroxypropyl-B-Cyclodextrin on the Aggregation of (E)-Resveratrol in Different Protonation States of the Guest Molecule. *Food Chemistry* 118(3), 648-655 (2010).
331. Bru, R., López-Nicolás, J., García-Carmona, F., Aggregation of Polyunsaturated Fatty Acids in the Presence of Cyclodextrins. *Colloids and Surfaces A: Physicochemical and Engineering Aspects* 97(3), 263-269 (1995).
332. Son, M., London, E., The Dependence of Lipid Asymmetry Upon Polar Headgroup Structure. *Journal of lipid research* 54(12), 3385-3393 (2013).
333. Son, M., London, E., The Dependence of Lipid Asymmetry Upon Phosphatidylcholine Acyl Chain Structure. *Journal of lipid research* 54(1), 223-231 (2013).
334. Bretscher, M.S., Asymmetrical Lipid Bilayer Structure for Biological Membranes. *Nature* 236(61), 11-12 (1972).

335. Verkleij, A., *et al.*, The Asymmetric Distribution of Phospholipids in the Human Red Cell Membrane. A Combined Study Using Phospholipases and Freeze-Etch Electron Microscopy. *Biochim. Biophys. Acta, Biomembr.* 323(2), 178-193 (1973).
336. Loftsson, T., Saokham, P., Couto, A.R.S., Self-Association of Cyclodextrins and Cyclodextrin Complexes in Aqueous Solutions. *International journal of pharmaceutics* 560, 228-234 (2019).
337. Loftsson, T., Másson, M., Brewster, M.E., Self-Association of Cyclodextrins and Cyclodextrin Complexes. *Journal of pharmaceutical sciences* 93(5), 1091-1099 (2004).
338. Duchêne, D., Wouessidjewe, D., Pharmaceutical Uses of Cyclodextrins and Derivatives. *Drug development and industrial pharmacy* 16(17), 2487-2499 (1990).
339. Hope, M., Bally, M., Webb, G., Cullis, P., Production of Large Unilamellar Vesicles by a Rapid Extrusion Procedure. Characterization of Size Distribution, Trapped Volume and Ability to Maintain a Membrane Potential. *Biochim. Biophys. Acta, Biomembr.* 812(1), 55-65 (1985).
340. MacDonald, R.C., *et al.*, Small-Volume Extrusion Apparatus for Preparation of Large, Unilamellar Vesicles. *Biochim. Biophys. Acta, Biomembr.* 1061(2), 297-303 (1991).
341. Chen, X., Hua, W., Huang, Z., Allen, H.C., Interfacial Water Structure Associated with Phospholipid Membranes Studied by Phase-Sensitive Vibrational Sum Frequency Generation Spectroscopy. *J. Am. Chem. Soc.* 132(32), 11336-11342 (2010).
342. Casal, H.L., Mantsch, H.H., Paltauf, F., Hauser, H., Infrared and ³¹P-Nmr Studies of the Effect of Li⁺ and Ca²⁺ on Phosphatidylserines. *Biochimica et Biophysica Acta (BBA) - Lipids and Lipid Metabolism* 919(3), 275-286 (1987).
343. Casillas-Iltuarte, N.N., Chen, X., Castada, H., Allen, H.C., Na⁺ and Ca²⁺ Effect on the Hydration and Orientation of the Phosphate Group of Dppc at Air– Water and Air– Hydrated Silica Interfaces. *J. Phys. Chem. B* 114(29), 9485-9495 (2010).
344. Li, W., Lu, B., Sheng, A., Yang, F., Wang, Z., Spectroscopic and Theoretical Study on Inclusion Complexation of Beta-Cyclodextrin with Permethrin. *J. Mol. Sci.* 981(1), 194-203 (2010).
345. Mohan, P.R.K., Sreelakshmi, G., Muraleedharan, C.V., Joseph, R., Water Soluble Complexes of Curcumin with Cyclodextrins: Characterization by Ft-Raman Spectroscopy. *Vibrational Spectroscopy* 62, 77-84 (2012).
346. Egyed, O., Spectroscopic Studies on B-Cyclodextrin. *Vibrational Spectroscopy* 1(2), 225-227 (1990).
347. Eicher, B., *et al.*, Intrinsic Curvature-Mediated Transbilayer Coupling in Asymmetric Lipid Vesicles. *Biophys. J.* 114(1), 146-157 (2018).
348. Marquardt, D., *et al.*, 1h Nmr Shows Slow Phospholipid Flip-Flop in Gel and Fluid Bilayers. *Langmuir*, (2017).
349. Gamble, D., Barnett, C., Scattering in the near Infrared. *Industrial & Engineering Chemistry Analytical Edition* 9(7), 310-314 (1937).
350. Didier, M.E.P., Tarun, O.B., Jourdain, P., Magistretti, P., Roke, S., Membrane Water for Probing Neuronal Membrane Potentials and Ionic Fluxes at the Single Cell Level. *Nat. Commun.* 9(1), 5287 (2018).
351. Starikov, E.B., Bräsicke, K., Knapp, E.W., Saenger, W., Negative Solubility Coefficient of Methylated Cyclodextrins in Water: A Theoretical Study. *Chem. Phys. Lett.* 336(5), 504-510 (2001).
352. Aree, T., Saenger, W., Leibnitz, P., Hoier, H., Crystal Structure of Heptakis(2,6-Di-O-Methyl)-B-Cyclodextrin Dihydrate: A Water Molecule in an Apolar Cavity. *Carbohydrate Research* 315(3), 199-205 (1999).
353. Mele, A., Mendichi, R., Selva, A., Non-Covalent Associations of Cyclomaltooligosaccharides (Cyclodextrins) with Trans-B-Carotene in Water: Evidence for the Formation of Large Aggregates by Light Scattering and Nmr Spectroscopy. *Carbohydrate Research* 310(4), 261-267 (1998).

354. Wu, A., Shen, X., He, Y., Micrometer-Sized Rodlike Structure Formed by the Secondary Assembly of Cyclodextrin Nanotube. *Journal of colloid and interface science* 302(1), 87-94 (2006).
355. Puskás, I., Schrott, M., Malanga, M., Szente, L., Characterization and Control of the Aggregation Behavior of Cyclodextrins. *Journal of Inclusion Phenomena and Macrocyclic Chemistry* 75(3), 269-276 (2013).
356. Mathapa, B.G., Paunov, V.N., Self-Assembly of Cyclodextrin–Oil Inclusion Complexes at the Oil–Water Interface: A Route to Surfactant-Free Emulsions. *Journal of Materials Chemistry A* 1(36), 10836-10846 (2013).

Curriculum vitae

Jan Dedic

Chemin de Bonne-Espérance 28

1006 Lausanne

jan.dedic@outlook.com

Born in Český Krumlov, Czech Republic

Citizenship: Czech republic

Education

07.2015 – 01.2020 EPFL, Lausanne

Ph.D. in Photonics

Thesis title: “*Soft matter probed by nonlinear scattering: self-assembly, interfaces, hydration, and long-range order*” (supervisor: Prof. Dr. Sylvie Roke).

09.2013 – 06.2015 Czech Technical University, Prague

M.Sc. (highest honors) in Photonics and Nanostructures

Thesis title: “*Study of the preparation of dielectric shell on gold nanorods*” (supervisor: Dr. Filip Novotný).

09.2010 – 09.2013 Czech Technical University, Prague

B.Sc. (honors) in Physical Engineering

Thesis title: “*Preparation of the free-standing monolayers of metallic nanoparticles*” (supervisor: Dr. Filip Novotný).

Skills

Technical

- Work in wet labs, chemical safety, preparation, analysis and handling of colloids. Preparation of oil-water nanoemulsions and liposomes by sonication, homogenization or extrusion. Synthesis of metallic colloids with subsequent surface modifications.
- Microscopy (optical, electron, AFM), spectroscopy (uv-vis-ir, Raman, nonlinear), dynamic light scattering, electrophoretic mobility measurements, viscometry.
- Work in optical labs, laser safety, optical setups (design, operation, maintenance).
- Extensive experience with femtosecond lasers, optical parametric amplifiers, and nonlinear optical effects.

IT

- Coding in Mathematica, Python, Matlab.
- MS Office Suite, Adobe Illustrator, Photoshop, Igor Pro, Zemax Optic Studio.

Languages

- English (C2, self-assessed)
- French (B2, certified, fluent)
- Czech (native)

Selected conferences and presentations

1. Oral presentation at “Swiss Soft Days, 25th edition”, Nestlé Research Center, Vers-chez-les-Blancs, Switzerland (August 2019).
2. Oral presentation to the Bristol Dynamics group, Bristol, UK (April 2019)
3. Oral presentation at “Frontiers in Optics/Laser science”, Washington Hilton, Washington D.C., USA. (September 2018).
4. Flash and poster presentation at “Physical Approaches to Membrane Asymmetry”, Physikzentrum, Bad Honnef, Germany (March 2018).

Extracurricular activities

Secretary and committee member of the EPFL Photonics Chapter (2018-2020)

Responsible for organization of networking events for academia and industry (communication, team management, procurement, budgeting).

Personal interests

Rock climbing, ski touring, modern art, classical music, acoustic guitar.